**Title**
Investigating how kinesin and dynein walk on complex microtubule surfaces



**Author**
Ferro, Luke

**Publication Date**
2020

Peer reviewed|Thesis/dissertation

# Investigating how kinesin and dynein walk on complex microtubule surfaces

By

Luke S Ferro

A dissertation submitted in partial satisfaction of the

requirements for the degree of

Doctor of Philosophy

in

Molecular and Cellular Biology

in the

Graduate Division

of the

University of California, Berkeley

Committee in charge:

Professor Ahmet Yildiz, Chair
Professor Eva Nogales
Professor Hernan Garcia
Professor Dan Fletcher

Summer 2020

Abstract

Investigating how kinesin and dynein walk on complex microtubule surfaces

by

Luke Scarpino Ferro

Doctor of Philosophy in Molecular and Cellular Biology

University of California, Berkeley

Professor Ahmet Yildiz, Chair

Eukaryotic cells are intricately organized on many length and time scales, from molecules to organelles. Much of this organization is achieved by motor proteins, which directionally transport intracellular components along cytoskeletal tracks (myosins on actin filaments, kinesins and dyneins on microtubules). Intracellular transport takes place in a highly crowded and dynamic cytoplasm, and microtubules are decorated with decorated with obstacles such as microtubule-associated proteins (MAPs), stationary organelles, protein aggregates, microtubule defects, opposing motor traffic and other cytoskeletal filaments. My graduate work focused on how kinesin and dynein respond to the presence of obstacles and MAPs on the microtubule. I chose to approach this question with an *in vitro* reconstitution approach coupled with single-molecule fluorescence microscopy.

To understand how obstacles and MAPs on the microtubule (MT) affect cargo transport driven by these motors, I first studied their motility on pure microtubules and then added in various types of obstacles, proteins, and microtubule geometries. Kinesin-1, yeast dynein and the active human dynein complex were challenged to walk on the microtubule in the presence of quantum dots or anti-tubulin antibodies attached to the microtubule surface. I used single-molecule tracking to dissect the motions of these motors to nanometer accuracy on the microtubule. I also used microfabrication to create “microtubule bridges” where the microtubule was raised off the coverslip surface, allowing for the motors to access all sides of the microtubule. I found that dynein motors are capable of bypassing a diversity of obstacles. In comparison, kinesin motors were incapable of walking on obstacle-coated microtubules. This observation, however, was not in line with *in vivo* observations that both kinesin and dynein can navigate cargos in the complex cellular environment. I discovered that kinesin motors are able to avoid obstacles when working as part of a multi-kinesin team. These results show that multiplicity of motors not only increases the collective force generation and the length of processive runs on an MT but also enables motors to maneuver around obstacles in their path.

Next, I investigated how motors and MAPs interact on the microtubule surface. MAPs have a microtubule-binding domain (MTBD) and a disordered projection domain which extends from the microtubule surface. I monitored kinesin and dynein motility on the microtubule in the absence and presence of the MAPs tau, MAP7 and DCX. With the exception of MAP7 and kinesin, each combination of motor and MAP resulted in inhibition of the motor. In collaboration with Lisa Eshun-Wilson and Mert Gölcük, we dissected the cause of this inhibition using fluorescence imaging, cryo-electron microscopy, and all-atom molecular dynamics. The ability of kinesin to walk on MAP7-coated microtubules was due to the favorable interactions between kinesin and MAP7's projection domain. Due to the differential effects of MAP7 on kinesin and dynein, we were able to control the directionality of kinesin-dynein assemblies by the addition of MAP7 to the microtubule. Protein engineering revealed that the inhibition of motors was due to the MAP's MTBD. Surprisingly, we found that motors could be inhibited by a MAP that did not overlap with the motor's binding site or activated by a MAP that did overlap with the motor's binding site. Using molecular dynamics, we showed that a large portion of the inhibition of dynein by tau could be linked to positively-charged residues on tau. The MTBDs of MAPs are enriched in lysine and arginine, allowing them to bind to the electronegative microtubule surface. We propose that the inhibition of motors by MAPs is driven by the positively-charged nature of MAP MTBDs, which alters the electrostatic environment of the microtubule and disrupts motor binding. Together, I present a general model for understanding how motors and MAPs interact on the microtubule.

**Acknowledgments**

To my parents, thank you for supporting me through the ups and downs of high school and college. You unquestionably empowered me to get where I am today. I was privileged to have such wonderful role models growing up. As an adult, I try to model my life and marriage after yours. Thank you for always being there for me.

To Erich Kushner, your patience and mentorship made a huge impact on my life at a time when I was looking for a direction. My life took a turn for the better after meeting you. I will always remember how important it is to mentor and empower the people younger than you.

Ahmet Yildiz, I am very grateful that you took a chance on me as a fourth rotation student. I don't think I was remotely qualified to join your lab and I appreciate your patience over the years as I have learned biochemistry and biophysics. It has been an incredible experience to train as a scientist in your lab. You provided me with a clear direction and kept my projects on the right track. I will also always remember to check the pH of my buffer and record my laser power before each experiment.

Sinan Can, you are a truly amazing friend and mentor. I don't know how I would have succeeded in a lab full of physicists without your support, guidance, and friendship. I will always remember dancing to bad music, ice bucket basketball and aligning microscopes for hours. The best part of graduate school was having the opportunity to work with you.

To Amanda Jack, it has been such a pleasure to work alongside you these last few years. I have been inspired by all you have accomplished, and I look forward to seeing what you will do in the future. I think that I got much more out of working with you than the other way around. Thank you for powering my last few years of graduate school with memes, '80s music and Boba tea.

Most importantly, I thank my wife Katelyn Costa who moved across the country with me to Berkeley and is now moving once again as I start a postdoc. The last seven years with you have unquestionably been the best of my life and I deeply appreciate everything you have done to support me. As much as I love science, I will always remember to put down my pipettes to spend time with you and Milo. Our wedding day remains the best day of my life and I have felt like a different person ever since. My only wish from life is that I love you as much as you deserve.

This dissertation is dedicated to my father, Ari Ferro.

**Contents**

## Chapter I: Introduction

### Cytoskeletal motors

The interior of cells is organized by active transport along cytoskeletal filaments such as microtubules (MTs) and actin. Motor proteins bind to these filaments and utilize ATP-powered conformational changes to translocate along these tracks [1,2]. Myosin family proteins walk along actin [3], while kinesin and dynein motors (Figure 1) move on microtubules[2]. Binding to the cytoskeleton triggers nucleotide hydrolysis and exchange which is coupled to mechanical movements between different protein domains of the motor [4-6]. Directionality of motor stepping is linked to the way motors bind their respective track and undergo ATP-induced conformational changes [7]. Cytoskeletal motors also apply forces to filaments, providing the driving force for cellular processes such as cell division and ciliary beating[8,9].

MTs are polymers of alpha and beta tubulin heterodimers and have an intrinsic polarity: the plus ends extend to the cell periphery and the minus ends are anchored in the cell center. They are composed of multiple protofilaments and dynamically switch between growing and shrinking depending on cellular conditions [10]. The dynamic instability of MTs allows for the cytoskeleton to be remodeled during processes such as cell migration and is modulated by the binding of MT-associated proteins [11]. Kinesin and dynein bind to the intra-dimer interface and interact with the unstructured C-terminal tails of tubulin [12]. The C-terminal tail of tubulin is the site of multiple post-translational modifications, such as polyglutamylation and detyrosination [13].

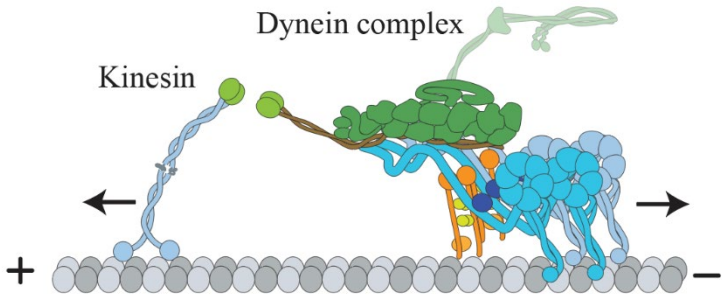


Figure 1. Schematic of kinesin and dynein structure on the microtubule.

The kinesin family of motors consists of many members, each with distinct functions or assigned cargoes [14,15]. Kinesin-1 (hereafter kinesin) is composed of a coiled-coil stalk that connects to N-terminal motor domains. Most kinesin motors walk to the plus-ends of MTs [16]. In contrast, all dyneins studied to date move towards the MT minus-end [17,18]. While there are about 40 kinesins responsible for plus-end directed motility, there is only a single isoform of dynein (cytoplasmic dynein) responsible for all dynein-driven processes in the cytoplasm [2]. The dynein motor domain is a heterohexameric ring of AAA+ subunits that connects to its MT binding domain through a coiled-coil stalk [19]. The motor domains dimerize through the N-terminal tail domain, which interacts with smaller polypeptides and cofactors of dynein [2]. Through these interactions, cytoplasmic dynein assembles into a complex consisting of three components: the dynein

complex, dynactin complex, and a cargo adaptor [20]. Cargo adaptors connect two dynein dimers to dynactin via a long coiled-coil domain [21,22].

The mechanism by which motors move along MTs has been studied extensively *in vitro*. For both motor families, stepping is powered by ATP-dependent conformational changes within the linker region [1,2]. Despite having complementary functions in the cell, kinesin and dynein display a remarkable divergence in the mechanism of their motility along MTs. For example, kinesin walks through coordinated stepping of its two motor domains along a single protofilament on a MT [23,24]. In comparison, the stepping of dynein monomers is largely uncoordinated, and dynein can take sideways and backward steps [25,26]. When not transporting cargo, both kinesin and dynein remain in their autoinhibited conformations. Dynein alone exists in an autoinhibited form and is only activated by forming a complex with dynactin and a cargo adaptor [20,27]. Kinesin is autoinhibited by folding of the tail domain onto the motor domain [28,29].

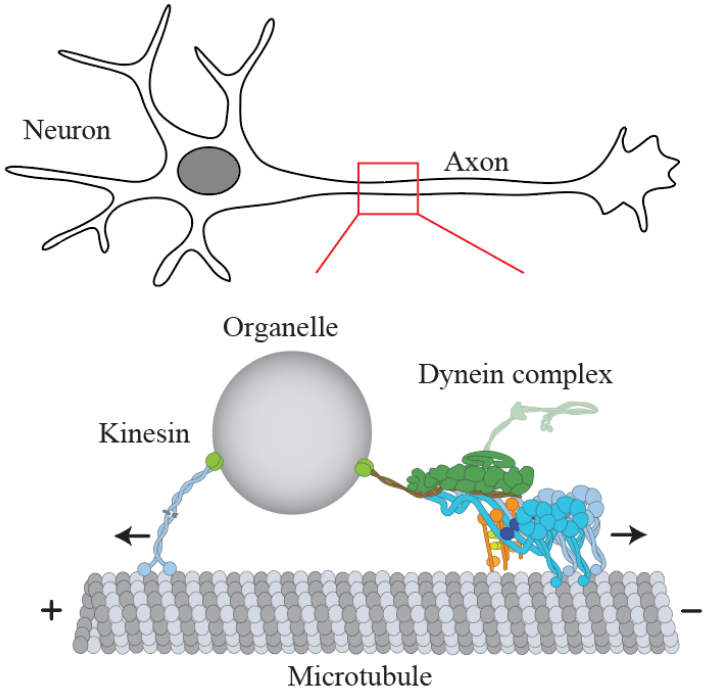


Figure 2. Schematic of kinesin and dynein transporting a cargo on a microtubule.

**Regulation of cargo directionality**

In neuronal axons, intracellular cargoes are shuttled back and forth between the cell body and the synapse (Figure 2). Defects in this process lead to neurodegeneration and developmental disorders[30]. Live-cell imaging studies revealed that most cargos simultaneously recruit kinesin and dynein motors [31,32]. The mechanism by which the cell creates a bias for one type of motor activity over another on a cargo is still an open question. Previous studies suggested that motors engage in a mechanical "tug-of-war" to dictate the direction of transport [31]. The tug-of-war model predicts that both motor types are actively pulling in the opposite direction and the cargo moves in the direction of the stronger motor. Consistent with this model, the cargo movement is often saltatory, such that unidirectional movement is interspersed with frequent pauses and brief reversals [33]. Live cell studies of endosomes also showed that cargos that move unidirectionally still display the activity of opposite polarity motors [34]. However, *in vitro* studies of motor tug-of-war show that active kinesin and dynein motors actively oppose each other, resulting in

substantially lower velocities for the kinesin/dynein complex [35,36]. This is in contrast to the high velocities of intracellular cargos as they move unidirectionally in between pauses and reversals [37]. The tug-of-war model also fails to explain why inhibition of transport in one direction also stops the transport in the opposite direction within minutes [32].

Co-dependence of motors on one another suggested that cells avoid futile tug-of-war between opposite polarity motors by tuning the recruitment and activation states of motors. One possibility is that cargoes control the relative number of kinesin and dynein bound to their surface and thereby influence the direction of travel [38]. Another is that the post-translational modification of MT tracks creates a bias for the activity of one motor type over another [13]. Given the evidence supporting both of these models, it is likely that the cell utilizes multiple methods to control the directionality of MT traffic.

**Obstacles to transport**

*In vivo,* kinesin and dynein transport cargoes on complex and crowded MT surfaces. Cellular MTs are coated in potential obstacles to transport such as MT defects, intersecting cytoskeletal elements, macromolecular crowding, stationary organelles and a diversity of non-motor MT binding proteins [37,39,40]. It is not well understood how motors transport cargos efficiently throughout the cell despite all of these challenges. Importantly, both kinesin and dynein must be able to avoid obstacles in their path, as the cell must maintain intracellular traffic in both directions. One method to bypass obstacles is to take sideways steps around them [41]. As kinesin has a limited ability to take sidesteps, it is inhibited by obstacles such as catalytically inactive motors, MAPs or cell extract [41-43]. Kinesin motors detach from the MT upon encountering an obstacle, and only infrequently can reattach to a neighboring protofilament and continue forward [41,44]. A different kinesin family member, kinesin-2, utilizes an increased side-stepping ability to avoid obstacles [45]. Little work has been done to understand how dynein avoids obstacles in its path. Human dynein alone, not the active complex, diffuses on the MT and reverses direction when encountering tau [42]. It is not well understood how the active dynein complex avoids obstacles [46].

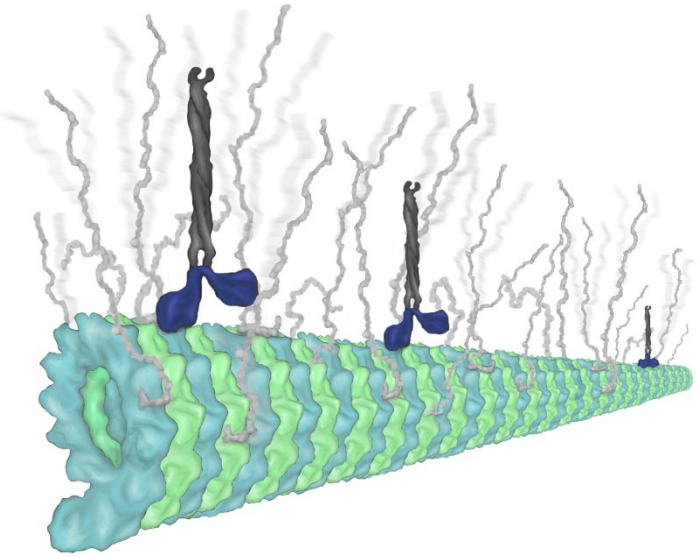

Figure 3. Schematic of kinesin walking along a microtubule coated with a MAP.

**Microtubule-associated proteins (MAPs)**

MTs are densely coated with a family of structural MAPs that play diverse roles in MT biology [11,13]. Members such as MAP2, tau, MAP7, DCX have been shown to regulate MT dynamics, organelle transport, cell polarity and axon morphogenesis [47,48]. MAPs possess two common features: a MT-binding domain (MTBD) which anchors them to the MT and a disordered projection domain. Tau and MAP4 bind on top of the MT protofilament, similar to motors, while EB1 and DCX bind between protofilaments and stabilize lateral tubulin contacts [49,50]. Secondary structure prediction and NMR experiments propose that the MT-binding domain of MAP7 forms an alpha-helical structure upon binding the MT [51]. However, MAP7's structure on the MT remains unknown.

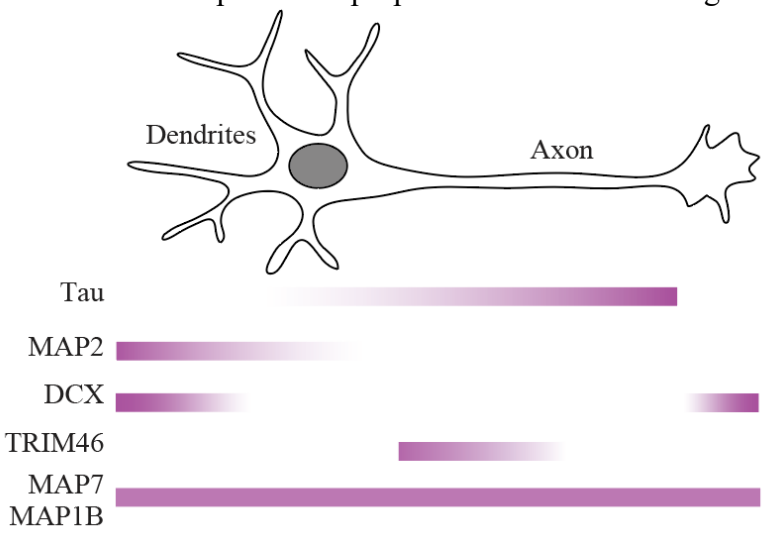


Figure 4. Schematic of MAP localization patterns in the neuron.

While MAPs are known to regulate the stability of the MT network, several studies have emerged suggesting that MAPs may also function to regulate motor traffic (Figure 3). The MAPs Tau, MAP7, XMAP4, She-1, doublecortin have all been shown to alter the activities of either kinesin or dynein [42,52-54]. This suggests that MAPs may be used by the cell to control the polarity of MT traffic. Tau is of particular interest in this respect, as it is known to play important roles in Alzheimer's disease [55]. In neurons, Tau is localized specifically to axons, with its concentration increasing in a proximodistal fashion [56]. Recent work has shown that the harmful effects of Aβ peptide in Alzheimer's disease can be ameliorated by reducing levels of endogenous Tau [30]. In addition, it has been shown in *Drosophila* that expression of Tau replicates many of the key features of human neurodegenerative diseases [57]. However, the exact mechanism behind Tau's neurotoxicity is not well understood.

*In vitro* and *in vivo* studies have investigated the role of Tau in regulating MT traffic. By over-expressing Tau in CHO cells, it was found that kinesin-driven traffic was impaired more so than dynein-driven traffic [56]. However, whether this was due to a direct or indirect effect on motor proteins remained unclear. Several *in vitro* studies also observed an inhibitory role of Tau on kinesin motility [39,58]. The effect of Tau on dynein motility is more ambiguous. Previous work has shown that purified human dynein motors reverse their directionality when they encounter Tau clusters on a MT [42]. However, this work was performed with dynein alone, rather than the

active dynein complex. Therefore, whether Tau has any role in differential regulation of kinesin over dynein motility is still an open question in the field [59].

Motors and MAPs compete for space on the MT surface as they carry out their functions. Recent work has looked at the interactions between kinesin-1 and MAP7, tau, MAP2, DCX, DCLK1 and MAP9 *in vitro* [39,58]. Interestingly, all MAPs were inhibitory to kinesin-1 except MAP7, which contains a kinesin-1 interaction domain. A similar effect was observed with kinesin-3 and MAPs [39]. Despite differences in domain organization, charge distribution, disorder and length, these MAPs all share a feature which is inhibitory to motors. The observation that MAPs can activate or inhibit motors has given rise to the concept of a "MAP code," similar to the histone code, in which MAPs govern the activity of motors of the MT [39]. MAPs have very different localization patterns in neurons, which may lead to differential regulation of motors throughout the neuron (Figure 4) [39]. However, the mechanism by which MAPs affect motor activity remains unclear. The binding sites of MAPs may overlap with motor binding site on MTs, or MAP condensates may form a selectivity barrier to control access of specific motors to the MT. These models have not yet been carefully tested in vitro.

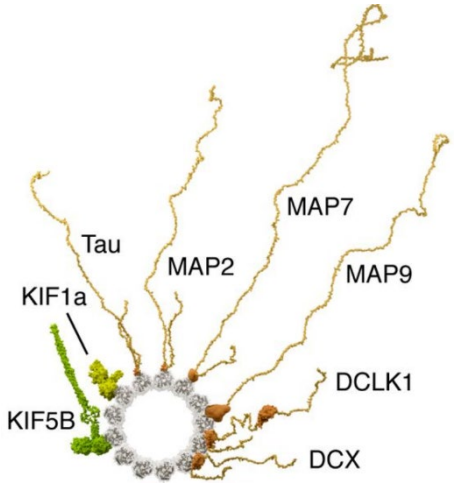


Figure 5. Schematic of the projection domains of MAPs. Adapted from Monroy et al. 2020.

**MAP condensates**

Biomolecular condensates are membrane-less compartments used to facilitate biochemical reactions in the cell [60,61]. Examples of condensates include the nucleolus, centrosome, heterochromatin, stress granules, P granules, and others. These compartments form when networks of weak interactions drive the de-mixing of proteins from the surrounding environment. Nucleic acids (RNA, DNA) are highly involved in the formation of biomolecular condensates because they can scaffold multivalent interactions [62-64]. The formation and dissolution of these bodies can be controlled by post-translational modifications, temperature, pH, or the availability of binding partners. Phase separation emerged as a way to form membraneless compartments, to function as a selectivity barrier to control the entry of certain agents into these compartments and also to control the soluble concentration of proteins inside the nucleus and cytoplasm [61].

On the MT surface, tau has been observed to form "1D" liquid condensates [65]. Rather than forming a sphere, these condensates conform to the shape of the MT. Tau binds the MT and diffuses until it finds another MAP [59,66]. Then, they cluster together into dynamic, liquid-like bodies that spread along the MT surface, in a manner driven by interactions between the

projection domains [59] (Figure 5). These condensates have been observed to undergo fusion and fission, supporting their liquid-like nature [66]. Future work is needed to determine if condensate formation is unique to tau or if it is a general property of MAP family proteins.

Condensates have been observed to allow for the partitioning of "client" proteins [60]. Client proteins interact with the proteins forming the condensate and this interaction drives the client into the condensate. For example, the MAP TPX2 forms condensates on the MT and drives MT branching by recruiting soluble tubulin to the MT surface [67]. In some cases, non-interacting proteins have been observed to be excluded from the condensates. This manifests as having a partitioning coefficient of less than one. Tau and TPX2 condensates recruit tubulin and enhance MT nucleation [67,68]. Tau condensates prevent the binding of kinesin and the MT-severing enzyme spastin to the MT [59,66]. The physiological role of these condensates remains to be elucidated.

**Single molecule techniques**

To address these questions, I have reconstituted the motility of kinesin-1 and cytoplasmic dynein motors on surface immobilized MTs *in vitro*. The motions of motors on the MTs were monitored by attaching fluorescent dyes to the motors [25]. Organic dyes are more suitable for these purposes than fluorescent proteins because they can be modified to improve photon yield and photostability [69]. The dye was excited by the wavelength of the excitation laser and it emits a red-shifted wavelength detected by the camera. In most of my experiments, I used total internal reflection fluorescence (TIRF) microscopy. In TIRF, reflection of the excitation light at the glass/water interface generates an evanescent wave that excites a narrow region of the flow chamber [70]. This allows for the excitation only of proteins or dyes that are near the interface, and reduction of autofluorescence from freely floating molecules and from Raman scattering of water.

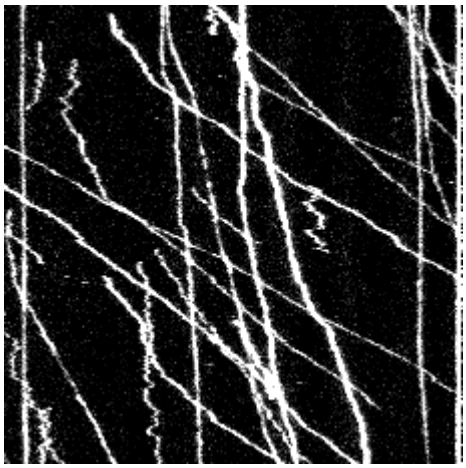

Figure 6. Kymograph of dynein complex motility on a microtubule.

I next decorated the MT surface with various obstacles or MAPs and tested how their presence on an MT affects the motility. Motors and MAPs are expressed in insect cells and purified using affinity tags. Tubulin and dynactin are purified from pig brains [71]. MTs are prepared by polymerizing tubulin with GTP and stabilized with taxol. Biotin-labelled MTs are incubated on a coverslip that is coated with PEG-biotin and streptavidin. The PEG surface helps reduce background signal from non-specific attachment to the surface. Movies of kinesin and dynein motility are visualized using kymographs, which are representations of distance on the x-axis and time on the y-axis (Figure 6). Diagonal lines in a kymograph represent motor

movement, which is then quantified in ImageJ to calculate the velocity, run frequency, and average run length of these motors.

## Chapter II: Kinesin and dynein use distinct mechanisms to bypass obstacles

*The work presented in this section was published in the following paper: "Kinesin and dynein use distinct mechanisms to bypass obstacles" written by Luke Ferro, Sinan Can, Meghan Turner, Mohamed Elshenawy and Ahmet Yildiz.* ***eLife*** *(2019)*

### Abstract

Kinesin-1 and cytoplasmic dynein are microtubule (MT) motors that transport intracellular cargos. It remains unclear how these motors move along MTs densely coated with obstacles of various sizes in the cytoplasm. Here, we tested the ability of single and multiple motors to bypass synthetic obstacles on MTs *in vitro*. Contrary to previous reports, we found that mammalian dynein is highly capable of bypassing obstacles. Human kinesin-1 motors fail to avoid obstacles, consistent with their inability to take sideways steps on to neighboring MT protofilaments. Kinesins overcome this limitation when working in teams, bypassing obstacles as effectively as multiple dyneins. Cargos driven by multiple kinesins or dyneins are also capable of rotating around the MT to bypass large obstacles. These results suggest that multiplicity of motors is required not only for transporting cargos over long distances and generating higher forces, but also for maneuvering of the cargos on obstacle-coated MT surfaces.

### Introduction

Kinesin and dynein move towards the plus- and minus-ends of MTs, respectively, and play major roles in intracellular cargo transport, cell locomotion, and division [1,72]. Although these motors have complementary functions on MTs, they have distinct structural and mechanistic features. Kinesin-1 contains a globular motor domain that binds the MT and hydrolyzes ATP. Two identical motor domains are connected by a short neck-linker to a common tail (Figure 1A)[1]. *In vitro* studies have shown that kinesin moves by coordinated stepping of its motor domains, in a manner akin to human walking [23,24]. It follows a single protofilament track on the MT and almost exclusively steps forward without frequent sideways or backward motion [73,74]. Unlike kinesin, dynein's motor domains are large heterohexameric rings of AAA+ ATPase subunits that connect to the MT through a coiled-coil stalk (Figure 1A)[18]. Stepping of the dynein motor domains is not tightly coordinated [25]. Instead, either monomer can take a step while the other serves as an MT tether [25,72]. Dynein has a large diffusional component in its stepping behavior, resulting in frequent sideways and backward steps [25]. Differences in the stepping behaviors between these motors may influence their cellular functions [31].

Intracellular transport takes place in a highly crowded and dynamic cytoplasm. The MT network is densely decorated with obstacles such as MT-associated proteins (MAPs), stationary organelles, protein aggregates, MT defects, opposing motor traffic and other cytoskeletal filaments [37,40,42]. It is not well understood how motors transport cargos efficiently throughout the cell despite these challenges. Previous *in vitro* studies suggested that motors need to take sideways steps to avoid obstacles on their path [41]. In agreement with this idea, kinesin motility is strongly inhibited by obstacles such as catalytically inactive motors, MAPs or cell extract [41-43]. While these motors can occasionally bypass obstacles by detaching and reattaching to neighboring protofilaments, they stall or detach from the MT in most cases [41,44]. Kinesin-2, a different kinesin family member with faster MT detachment/reattachment kinetics [75] and increased side-stepping ability [45], bypasses obstacles more successfully than kinesin-1. Dynein was expected to be less sensitive to obstacles than kinesin because of its elongated structure and frequent sideways stepping [25]. Yet, *in vitro* studies on isolated mammalian dynein observed that the motor reverses direction when encountering a MAP obstacle rather than bypassing it [42,76]. However, these studies were conducted before it was understood that mammalian dynein alone is autoinhibited and its activation requires assembly with dynactin and a cargo adaptor [20,77,78]. Therefore, how active dynein motors bypass obstacles on MTs is not well understood [46].

Unlike helicases, unfoldases and DNA/RNA polymerases which usually function as individual motors [79], cytoskeletal motors often operate in teams to transport a cargo [32,38,80]. Multiple motors carry cargos with increased processivity relative to single motors [35], which is essential for long-range transport in cell types such as neurons. Teams of motors also exert higher forces, which may enable the transport of large cargos through the dense cellular environment [81]. It has been proposed that cargos with multiple motors also avoid obstacles more effectively than single motors [31]. A recent study found that multi-kinesin cargos pause at MT defects rather than detach like single motors [40]. Ensembles of two kinesin-1 motors linked together with a DNA scaffold have a higher run length than single kinesins, but their run length was also decreased in the presence of neutravidin obstacles on the MT [75]. Motility of multiple dyneins has not been studied on MTs decorated with obstacles. Therefore, it is not well understood whether cargos driven by multiple motors bypass obstacles more successfully than single motors.

Here, we challenge single- and multi-motor cargos of kinesin and dynein with quantum dot (QD) and tubulin antibody obstacles on MTs. We find that kinesin and dynein employ different mechanisms to bypass these obstacles. Consistent with their ability to take side-steps, single dynein motors efficiently circumnavigate around QD obstacles. Unlike dynein, single kinesins are strongly inhibited by QDs and antibodies on MTs yet overcome this limitation when working together as a team. The multiplicity of motors was also critical to bypass large roadblocks. When cargos driven by a team of kinesin or dynein motors face a wall along their path, they swing around the MT without net forward movement and continue moving forward. Together, our

results provide insight into how motors transport intracellular cargos along obstacle-coated MT surfaces.

## Results

### Single dyneins, but not kinesins, bypass obstacles

Previous studies used rigor motors [41], cell extracts [43] or MAPs [42] to study how motors move in the presence of obstacles. Because some of these obstacles have complex binding kinetics to MTs, vary in size, and interact with motors directly, it is difficult to discern how their presence on the MT obstructs motility. We sought a model obstacle that stably attached to the MT, had a well-defined size and formed no specific interactions with motors. To this end, we decorated biotinylated MTs with streptavidin-conjugated QDs (25 nm in diameter) [25]. These QDs have a bright and photostable fluorescent emission, which enable us to measure their linear density along MTs.

We studied the motility of human kinesin-1, yeast cytoplasmic dynein, and mammalian dynein/dynactin in the presence and absence of QD obstacles. Human kinesin-1 was truncated at its coiled-coil stalk (expressing amino acids 1-560) and fused to GFP and HaloTag at its C-terminus [82]. The N-terminal tail domain of yeast cytoplasmic dynein was replaced with a glutathione S-transferase (GST) tag for dimerization and HaloTag for labeling (GST–Dyn331kD, expressing amino acids 1219-4093 of the dynein heavy chain) [83]. Mammalian dynein/dynactin complex was assembled using full-length human cytoplasmic dynein, pig brain dynactin and N-terminal coiled-coil of mouse BicD2 (BicD2N). To facilitate assembly of the DDB complex, we used a human dynein mutant that does not form the autoinhibited conformation [27]. Motors were labeled with excess QDs of a different color on their tail region and their motility on surface-immobilized MTs was monitored using multicolor imaging (Figure 1A). The run length of kinesin-QD (2.1 ± 0.2 μm, mean ± SD) was similar to kinesin motors labeled with an organic dye ($p = 0.21$, two-tailed t-test, Figure 7D,E), suggesting that QDs were driven by single motors.

The surface density of QD obstacles was varied, with a maximum decoration of 12 QDs $\mu m^{-1}$ (Figure 1B,C). Consistent with dynein's ability to take side-steps, we found that single yeast dynein and DDB motors walked processively even at the highest QD density tested (Figure 1D,E, Figure 7) [25]. We did not see evidence of motor reversals when DDB encountered a QD obstacle, suggesting that previously observed reversals of mammalian dynein might be due to diffusive motion of this motor in the absence of dynactin and a cargo adaptor [20,77,78]. While mobile fraction, velocity and run length of yeast dynein were reduced 30-70% by increasing density of QDs, DDB motility was less sensitive to obstacles. In comparison to dynein motors, kinesin motility was severely affected by the QDs (Figure 1D,E). The majority of kinesins became stuck on the MT by the addition of QDs (Figure 1D,E). At low QD density (1-2 $\mu m^{-1}$), the mobile fraction was reduced 90%, while the run length and velocity were reduced by 60%

compared to no obstacle condition ($p = 0.0003$, Figure 1E). Kinesin motility could not be analyzed at higher QD densities because we did not detect processive runs longer than 250 nm under these conditions. Collectively, these results show that kinesin remains bound to an MT but is unable to move forward when it encounters an obstacle.

**Kinesin pauses longer than dynein when encountering QD obstacles.**

We next investigated how obstacles affected the pausing behavior of motors. Even at the lowest QD density, most kinesin motors were immotile throughout the recording, suggesting that kinesin has a high likelihood of permanently pausing when encountering a QD. Trajectories of the remaining processive motors were interspersed with frequent pauses (Figure 8). We analyzed the trajectories of these motors before they permanently paused or dissociated from the MT and calculated the residence times of motors per distance traveled (Figure 2A). Residence times were composed of two distinct states. A fast state corresponded to processive motility of the motor along MTs and a slow state represented transient pauses in motility (Figure 2B). We calculated the density and length of pauses from the frequency and decay time of the slow state (Figure 2B). Strikingly, kinesin pause density increased two-fold and pause time increased four-fold at 2 QDs $\mu m^{-1}$. In contrast, pause density and duration of yeast and DDB were only modestly increased by the QD density (Figure 2C). Transient pauses may correspond to detachment of kinesin when encountering an obstacle and reattachment to a nearby protofilament [41]. However, this mechanism is not robust enough to efficiently bypass obstacles and kinesin motility stalls permanently usually after a few transient pauses in motility. Dynein also pauses frequently in the presence and absence of QD obstacles (Figure 9). However, unlike kinesin, it rarely pauses permanently even at the highest density of QDs (Figure 1D,E).

**Kinesin quickly detaches from MTs decorated with antibody obstacles**

Previous studies have reported that kinesin motors detach when encountering catalytically "dead" motors or MAPs on the MT rather than getting stuck [41,43]. It is possible that bulky obstacles, such as QDs may hinder motor movement more than proteins. To test this idea, we labeled kinesin motors with Cy3 dye instead of a QD. In assembling the dynein complex, mouse BicDR1 with a C-terminal SNAP tag was labelled with LD555 and incubated with dynein/dynactin [21]. In addition, we decorated the MTs with anti-tubulin antibody obstacles (Figure 3A). Because antibodies are small in size (~150 kDa), they likely block fewer protofilaments than QD obstacles (Figure 10). Similar to QD-obstacles, we see that single kinesin motors are more strongly inhibited by antibody obstacles than DDB ($p = 0.013$ for velocity and 0.01 for run length, two-tailed t-test, Figure 3B, C). Kinesin run length and velocity were reduced by ~70% at 20 µg/mL antibody ($p = 0.01$ and 0.0001, respectively, two-tailed t-test, Figure 3C). In contrast to QD-obstacles, there was not a significant difference between the mobile fraction of kinesin and dynein at 20 µg/mL antibody ($p = 0.15$, two-tailed t-test). Consistent with a previous study that used rigor kinesin as an obstacle [41], we did not observe extended pauses of kinesin motors. Thus, antibody obstacles inhibit kinesin by causing them to

detach rather than pausing for extended periods. Collectively, our results show that single kinesins detach from MT when encountering small, protein obstacles. However, kinesin motors that carry a rigid QD cargo are more likely to pause when encountering a bulkier obstacle on an MT.

**Obstacle avoidance of single motors on freely suspended MTs**

On surface-immobilized MTs, motors cannot access protofilaments facing the coverslip. As a result, surface immobilization may serve as an additional obstacle as the motors attempt to bypass the QDs. MTs in the cell, however, are freely suspended in 3D. This may allow motors to fully explore the MT surface and more successfully bypass the obstacles. To test this possibility, we constructed "MT bridges" by immobilizing MT ends to polydimethylsiloxane (PDMS) ridges on either end of a 10-µm deep valley (Figure 4A,B, Figure 11). Similar to surface-immobilized MTs, DDB and yeast dynein were able to walk at the highest QD concentration tested on MT bridges (Figure 4C). Interestingly, yeast dynein's run length was 2.5-fold higher on MT bridges compared to surface-immobilized MTs at 12 QD $\mu m^{-1}$ ($p < 0.001$, two-tailed t-test, Figure 1E, Figure 4C), suggesting that this motor bypasses obstacles more successfully by exploring the entire MT surface. However, we did not observe a significant improvement in kinesin motility on MT bridges in comparison to surface-immobilized MTs (Figure 1E, Figure 4C). The mobile fraction was reduced 75% at 1 QD $\mu m^{-1}$ compared to the no obstacle condition and motility could not be detected at 7 QDs $\mu m^{-1}$. Similar to surface-immobilized MTs, frequent pauses were observed in kinesin motility in the presence of QD obstacles on MT bridges (Figure 12). These results suggest that kinesin is intrinsically limited by its ability to side-step to adjacent protofilaments when it encounters obstacles on an MT.

**Multi-kinesin cargos bypass obstacles on MTs**

In cells, cargos are often carried by multiple motors, which increases collective force generation and enables transport of the cargo over longer distances [32,35,38,80] as well as slightly higher velocities [84]. We asked whether multiple motors can transport cargo under conditions in which single motors are unable to walk along MTs. To test this, 500 nm cargo beads were coated with multiple kinesins or DDB motors (Figure 5A). In the absence of QD obstacles, the beads were highly processive and did not detach until they reached the end of the MT. When the beads were incubated with a low concentration (50 nM) of kinesin motors, we detected processive motility of beads, albeit with frequent pausing, on MTs decorated with 7 QDs $\mu m^{-1}$ (Figure 5B). This was a density at which single kinesins were completely inhibited (Figure 1E). However, motility of these beads was severely inhibited at 12 QDs $\mu m^{-1}$. Surprisingly, when beads were incubated with a higher concentration (1.5 µM) of kinesin, their mobile fraction was unaffected by the decoration of MTs with 12 QDs $\mu m^{-1}$ (Figure 5B,C, Figure 13). Similarly, multiple DDBs transported beads to the minus-ends of MTs regardless of the surface density of QDs with no decrease in mobile fraction (Figure 5B,C).

The analysis of the individual trajectories of dynein-driven beads showed the velocity decreases by 28% in the presence 12 QD $\mu m^{-1}$ ($p = 0.02$, two-tailed t-test, Figure 5C), comparable to 19% decrease of the velocity of single dyneins under the same conditions ($p = 0.05$, two-tailed t-test, Figure 1E). The velocity of kinesin-driven beads has also decreased by 25% decrease when exposed to 12 QDs $\mu m^{-1}$ ($p = 0.02$, two-tailed t-test, Figure 5C). We also tested if multi-kinesin cargoes were able to walk on antibody-coated MTs better than single kinesin motors. For beads coated with 1.5 μM of kinesin, run length and mobile fraction are unaffected by 20 μg/mL antibody (Figure 5D, E). Remarkably, all beads walked until they reached the end of the MT (Figure 5D). Mobile fraction was also not reduced ($p = 0.73$, Figure 5E). Similar to QD-obstacles, multi-motor kinesin had reduced velocity at 20 μg/mL antibody ($p = 0.04$, Figure 5E). Therefore, while single kinesins are strongly affected by obstacles on MTs, a team of kinesins can carry cargo beads over long distances as well as dyneins along MTs densely decorated with obstacles.

**Multi-motor cargos rotate around the MT to avoid large obstacles**

Avoiding obstacles larger than a QD, such as a stationary organelle or intersecting cytoskeletal filament, may require cargo to rotate to the other side of the MT before continuing forward movement [85]. *In vivo* studies have observed both anterograde and retrograde cargos to bypass stationary organelles [37]. It has been proposed that rotation of cargo around the MT requires the presence of both kinesin and dynein motors on the cargo or the distortion of the lipid cargo [31,33,85]. To test whether a single type of motor can rotate a rigid cargo around the MT, we tracked beads driven by multiple kinesins or dyneins on MT bridges. If the beads were positioned below the MT when they reached the end of the bridge, they were challenged to bypass the PDMS wall (Figure 6A). Remarkably, we observed that most of these beads rotated to the top of the MT with no forward motion before they continued along the MTs (77 ± 13% kinesin beads and 85 ± 5% dynein beads, mean ±SD, Figure 6B,C). This movement was different from the previously observed helical movement of kinesin- or dynein-driven cargos around the MT [74,86], in which rotation is accompanied by forward translational movement. 29% and 24% of kinesin- and dynein-driven beads, respectively, paused before moving forward (Figure 6B,C), similar to intracellular cargos that encounter stationary organelles [37]. In contrast to strong inhibition of single kinesins by obstacles, beads driven by multiple kinesins paused for a shorter period than dynein-driven beads when they encountered the wall (3.8 ± 0.2 s vs 7.8 ± 1.0 s, mean ± SEM, Figure 6D). Only 23% of kinesin beads and 15% of dynein beads either got stuck or detached from MTs at the PDMS wall. We concluded that cargos driven by multiple motors can bypass large obstacles by rotating around the circumference of the MT

**Discussion**

Despite the complexity of the cytoplasm, kinesin and dynein drive intracellular transport with remarkable efficiency towards MT ends. In this study, we investigated the ability of kinesin and

dynein to bypass permanent obstacles using *in vitro* reconstitution and single-molecule imaging. These results show that kinesin and dynein utilize different mechanisms to bypass these obstacles. Despite their large size, single dyneins were highly capable of maneuvering around obstacles on the MT. In contrast, single kinesins were strongly inhibited by obstacles, as previously reported [41-44]. These results are likely a consequence of differences in the sidestepping ability of the two motors [25,73,74]. Remarkably, multiple kinesins were able to bypass these obstacles as efficiently as dyneins. In the case of multi-motor cargos, we anticipate that kinesin motors are just as likely to get stuck at an obstacle as a single motor. However, the other motors driving the cargo may exert a force on the stuck motor, causing its rapid detachment and the continued forward motion of the cargo [87]. In this process, new motors in the leading direction are being recruited into the interface with the lattice, while the motors in the trailing direction detach from an MT, which causes rolling of the cargo around the obstacle. Alternatively, a team motors carrying the cargo pause until they move sideways either because motors step to neighboring protofilaments or stochastic shifts in the center of mass of the bead allow for unbound motors to attach to adjacent protofilaments. Addressing the mechanism of obstacle avoidance of multiple motors will require future studies at higher spatial resolution.

Multi-motor teamwork also proved beneficial for both types of motors when challenged by a large obstacle. Cargo beads driven by multiple kinesin or dynein motors were able to maneuver around a PDMS obstruction that blocked access to half of the MT surface (Figure 10). This behavior helps explain how cargos bypass large cellular roadblocks such as stationary organelles or intersecting cytoskeletal filaments. Recent measurements observed rotational motion in the trajectories of endosomal cargos carrying gold nanorods [33]. In addition, correlative live-cell and super-resolution microscopy showed that rotational movement could be used by cargos to avoid steric obstacles [85]. These studies proposed that rotational movement and off-axis stepping might result from having a mix of motors, such as kinesin-2 or dynein, on the cargo along with kinesin-1. While transient back-and-forth movement of cargo may allow it to change the protofilament track, our results clearly show that tug-of-war between opposite polarity motors is not required to bypass large obstacles. Instead, cargo beads driven by multiple motors can switch to the other side of the MT surface by rotation, when only one type of motor is active at a time. We also showed that fluidity of the cargo is not essential for this process [85]. These results show that multiplicity of motors not only increases the collective force generation and the length of processive runs on an MT but also enables motors to maneuver around obstacles in their path. Future studies are required to address how the motor copy number affects the ability of cargo to bypass dynamic obstacles, such as MAPs.

**Materials and Methods**

| Reagent type (species) or resource | Designation | Source or reference | Identifiers | Additional information |
|---|---|---|---|---|
| Other | Amino quantum dot (655) | ThermoFisher | Q21521MP | |
| Other | Streptavidin quantum dot (585) | ThermoFisher | Q10111MP | |
| Chemical | APTES | Sigma | 440140 | |
| Antibody | Anti-tubulin antibody (mouse monoclonal) | Sigma, Tub 2.1 | T5201 | Dilution range 0 – 20 µg/mL |
| Peptide, recombinant protein | Human Kinesin-1 | Belyy et al. 2016 | N/A | |
| Peptide, recombinant protein | Yeast dynein heavy chain | Reck-Peterson et al. 2006 | N/A | |
| Peptide, recombinant protein | BicD2 (amino acids 1-400) | Schlager et al. 2014 | Addgene 111862 | |
| Peptide, recombinant protein | Human cytoplasmic dynein complex | Zhang et al. 2017 | N/A | |
| Chemical | Acetone | Sigma | 270725 | |
| Chemical | Ethanol | Sigma | 459828 | |
| Other | IgG Sepharose Beads | GE Healthcare | 17096902 | |
| Chemical | Glutaraldehyde | Fisher Scientific | G1511 | |
| Other | PDMS | Sylgard 184 Silicone Elastomer | N/A | |
| Other | Glucose oxidase | Sigma | G2133 | |
| Other | Catalase | Sigma | C3155 | |
| Chemical | Taxol | Sigma | T7191 | |

| | | | | |
|---|---|---|---|---|
| Peptide, recombinant protein | Pig Brain Dynactin | Schlager et al. 2014 | N/A | |
| Peptide, recombinant protein | Pig Brain Tubulin | Castoldi et al. 2003 | N/A | |
| Chemical | ATP | Sigma | A3377 | |
| Other | Ni-NTA beads | Thermo Scientific | 88221 | |
| Chemical | Fugene HD transfection reagent | Promega | E2311 | |
| Chemical | HaloTag Ligand succinimidyl ester | Promega | P6751 | |
| Chemical | SU-8 2010 photoresist | Microchem | N/A | |
| Other | Super Active Latex Beads | Thermo Fisher | C37481 | |
| Chemical | Sulfo-NHS | Thermo Fisher | 24510 | |
| Chemical | EDC | Thermo Fisher | 22980 | |
| Software | U-track | Jaqaman et al. 2008 | N/A | |
| Antibody | Anti-GFP (anti-rabbit polyclonal) | Covance | N/A | Used at 0.4 mg/mL |
| Peptide, recombinant protein | Mouse BicDR1 (full length) | Urnavicius et al. 2018 | Adapted from Addgene 111585 | |

**Protein expression and purification**

A human kinesin-1 coding sequence expressing amino acids 1-560 was fused to GFP, HaloTag and a 6xHis tag on the C-terminus (hK560::GFP::HaloTag::6xHis)[82]. The N-terminus of yeast cytoplasmic dynein was replaced with a HaloTag and a GST dimerization tag (HaloTag-GST-$Dyn1_{331kDa}$, consisted of amino acids 1219-4093 of the dynein heavy chain)[83]. A full length human cytoplasmic dynein construct consisted of the dynein heavy chain tagged with an N-terminal SnapTag, cloned into a pOmniBac vector, and fused to a plasmid that containing dynein intermediate chain, light intermediate chain and three different light chains (Tctex, Roadblock and LC8), as described [77]. We used a dynein mutant that does not form the autoinhibited phi-conformation [27] to facilitate assembly of the DDB complex. The BicD2N construct consisted of GFP fused to the first 400 amino acids of mouse BicD2 [77]. The mouse BicDR1consisted of SNAP tag fused to the C-terminus of the full-length protein [21].

**Kinesin purification**

Rosetta cells transformed with kinesin plasmid were grown in a 5 mL culture overnight. This culture was added to 1 L of LB media and grown for 3 hours until the OD600 reached 0.7. Cells were induced with fresh 100 μM IPTG, put on ice until the temperature reached 20 degrees and incubated overnight at 20 degrees at 180 RPM. After harvesting cells at 4785 RCF for 15 minutes in a JLA 8.1 rotor, 500 mL cell pellets were incubated with 40 mL lysis buffer (50 mM sodium phosphate monobasic pH 8.0, 250 mM sodium chloride, 2 mM magnesium chloride, 20 mM imidazole, 1 mM ATP, 10 mM beta-mercaptoethanol (BME), 1 mM phenylmethylsulfonyl fluoride (PMSF). Cells were lysed with a sonicator and spun in a Ti70 rotor at 117734 RCF for 30 min. The supernatant was incubated with 6 mL of washed Ni-NTA bead slurry (HisPur, Thermo Scientific) for 1 hour at 4 degrees. Beads were collected in a BioRad column and washed in wash buffer (50 mM sodium phosphate monobasic pH 6, 250 mM sodium chloride, 1 mM magnesium chloride, 20 mM imidazole, 100 μM ATP, 10 mM BME). Protein was eluted in elution buffer (50 mM sodium phosphate monobasic pH 7.2, 250 mM sodium chloride, 1 mM magnesium chloride, 500 mM imidazole, 100 μM ATP, 10 mM BME) and snap-frozen in liquid nitrogen after addition of 20% glycerol.

**Yeast dynein purification**

Yeast cells were cultured on YPAD plates for 2-3 days. A 10 mL culture was grown overnight in YP media with 1 mL of 25% dextrose + 0.04% adenine supplements at 30 degrees. 2 mL of the culture was then added to 100 mL of 1.25x YP media supplemented with 10 mL of 20% raffinose. After 9 hours of growth, the entire culture was added to 1.8 L of YP media supplemented with 200 mL of 20% (w/v) galactose. Cells were cultured at 30 degrees with shaking (200 rpm) overnight until the OD600 reached 1.5. After harvesting cells at 4785 RCF for 15 minutes in a JLA 8.1 rotor, cells were frozen dropwise and lysed while frozen in a coffee grinder. 50 mL of lysis buffer (30 mM HEPES pH 7.4, 50 mM potassium acetate, 2 mM magnesium acetate, 1 mM EGTA, 10% glycerol, 1 mM dithiothreitol, 100 μM ATP, 1 mM PMSF) was added to a 1 L yeast pellet. Cells were spun at 360562 RCF for 45 min in a Ti70 rotor. The supernatant was incubated with washed IgG beads (IgG Sepharose 6 Fast Flow, GE Healthcare) for 1 hour with gentle rolling. Beads were collected using a BioRad disposable column, washed with wash buffer (lysis buffer with 125 mM KCl) and TEV buffer (10 mM Tris pH 8, 150 mM KCl, 10% glycerol, 1 mM tris(2-carboxyethyl)phosphine, 100 μM ATP, 1 mM PMSF). Beads were transferred to an Eppendorf tube and eluted with TEV protease for 1 hour. Beads were then spun down and the supernatant was snap-frozen in 20% glycerol.

**Purification of mammalian dynein-dynactin**

Human dynein, mouse BicD2N, mouse BicDR1 and pig brain dynactin were purified as previously described [27]. Further information can also be found on Invitrogen's Bac-to-Bac Baculovirus Expression System Guide (Invitrogen). Briefly, plasmids containing genes of interest were transformed into DH10Bac competent cells and plated on LB agar plates with

kanamycin, gentamycin, tetracycline, Blue-gal, and isopropyl beta-D-1-thiogalactopyranoside. An overnight culture of a colony grown in 2X YT media with kanamycin, gentamycin and tetracycline and the bacmid was purified from these cells. Cells were lysed and neutralized using Qiagen miniprep buffers P1, P2, and P3. DNA was then precipitated with isopropanol and spun down for 10 min at 13,000 RCF at 4 °C. The DNA pellet was washed three times with 70% ethanol, air-dried and resuspended in Qiagen's EB buffer.

Bacmid was used within a few days for transfecting Sf9 cells. All insect cell culture was courtesy of Berkeley's Cell Culture Facility. The cells have not been authenticated or tested for mycoplasma contamination. 2 mL of Sf9 cells at 500,000 cells/mL was aliquoted into a 6-well dish and allowed to attach for 10 minutes. 1 microgram of bacmid DNA was diluted in ESF 921 media (Expression systems, no antibiotic or serum), mixed with 6 µL of Fugene HD transfection reagent (Promega) and incubated for 15 minutes at room temperature. Media on the cells was removed and replaced with 0.8 mL of ESF 921 media. The Fugene/DNA mix was added dropwise on the cells. The dish was sealed with Parafilm and incubated for 72 h. 24 h into this incubation, 1 mL of extra ESF 921 media was added to the cells. After removing the media and spinning, 1 mL of the supernatant (P1 virus) was added to 50 mL of Sf9 cells at a density of 1 million cells/mL. Following a 72 h incubation, the media was spun down and the supernatant (P2 virus) was harvested. 10 mL of the P2 virus was used to infect 1 L of Sf9 cells at 1 million cells/mL and expression proceeded for 72 hours. Cells expressing the protein of interest were harvested at 4000 RCF for 10 min and resuspended in 50 mL lysis buffer (50 mM HEPES pH 7.4, 100 mM NaCl, 10% glycerol, 1 mM DTT, 100 µM ATP, 2 mM PMSF and 1 tablet of protease inhibitor cocktail). Lysis was performed using 15 loose and 15 tight plunges of a Wheaton glass dounce. The lysate was clarified using a 45 minute, 360562 RCF spin in a Ti70 rotor and incubated with 2 mL IgG beads (IgG Sepharose 6 Fast Flow, GE Healthcare) for 2 h. Beads were washed with lysis buffer and TEV buffer (50 mM Tris pH 7.4, 150 mM potassium acetate, 2 mM magnesium acetate, 1 mM EGTA, 10% glycerol, 1 mM dithiothreitol, 100 µM ATP). Beads were then collected and incubated with TEV protease overnight to elute the protein. Finally, the protein was concentrated and snap-frozen in liquid nitrogen after the addition of 20% glycerol.

**Glass silanization**

Glass slides were functionalized with aminopropyltriethoxysilane (APTES) and glutaraldehyde to allow for covalent attachment of MTs, as described previously [88]. APTES (Sigma, 440140) aliquots were prepared in 5 mL cryotubes (Corning, 430656) using glass pipettes, capped under nitrogen atmosphere, snap-frozen upright in liquid nitrogen and stored in -80 °C. Glass slides were sonicated in a 2% Mucasol (Sigma, Z637181) prepared in hot water and then rinsed thoroughly in water. Slides were then baked on a hot plate (Benchmark, BSH1002) to remove excess water for 5 min. To create functional silanol groups, slides were treated with oxygen plasma (PETS Reactive Ion Etcher) at 200 mTorr oxygen, 55 W for 1 min. Slides were rinsed

briefly in acetone (Sigma, 270725) and immersed in a 2% (v/v) APTES in acetone for 1 min. APTES aliquots were added to acetone before warming to room temperature. After silane treatment, the slides were rinsed in acetone and baked on a 110 °C hot plate for 30 min. To remove silane unbound to the glass, slides were sonicated sequentially in ethanol (Sigma, 459828) and water for 5 min. Following this treatment, slides were again baked at 110 °C for 30 min. An 8% glutaraldehyde solution (Fisher Chemical, G1511) was prepared in water and 1 mL drops of the solution were made on Parafilm. Slides were incubated functional-side down on the glutaraldehyde solution drops for 30 min in a sealed container. Finally, the slides were washed and sonicated in water for 10 s to remove loosely absorbed glutaraldehyde and stored in a sealed container at room temperature up to 1 week.

**Labeling**

Motors were labeled with QDs modified with a HaloTag or SnapTag ligand. Amino-PEG-QDs (Thermo, Q21521MP) were labelled with HaloTag ligand by reaction with N-hydroxysulfosuccinimide reactive Halo-Tag ligand (Promega, P6751) or Snap-Tag ligand for 30 min at room temperature. QDs were then exchanged into 25 mM borate pH 8.5 using Amicon 100K centrifugal filters and stored in that buffer. 2 μM of these QDs were mixed with 100-500 nM motors fused with a SNAPTag or HaloTag for 10 min on ice. For labeling with dye, HaloTag-Cy3 was added to kinesin while it was bound to beads during the purification. Excess dye was washed away before eluting the protein. A similar procedure was used to label SNAP-BicDR1.

**Motility assays**

Tubulin was purified from pig brain and labeled with biotin or fluorophores as described [71,88]. The final percentage of biotin on the MT was less than 5%. To perform motility assays, biotinylated MTs were diluted in BRB80 (80 mM PIPES pH 6.8, 1 mM EGTA, 1 mM magnesium chloride) supplemented with 10 μM taxol and flowed into a chamber made with two pieces of double-sided tape between an APTES-silanized slide and an unmodified coverslip. Chamber was then passivated with BRB80 supplemented with 1 mg/mL casein (Sigma, C5890), 1 mM DTT and 10 μM taxol. The chamber was incubated with different dilutions of streptavidin-coated QDs (Invitrogen, Q10111MP) or monoclonal anti-β-tubulin antibody produced in mouse (T5201, Sigma). At low QD concentrations, the linear density of QD-obstacles on the MT was measured by counting the number of fluorescent spots from TIRF images. At higher QD concentrations, the linear density was estimated from the ratio of total fluorescence signal on an MT to the fluorescence intensity of a single QD.

BRB80 (above), DLB (30 mM HEPES pH 7.2, 2 mM magnesium chloride, 1 mM EDTA, 10% glycerol) and MB (30 mM HEPES pH 7.0, 5 mM $MgSO_4$, 1 mM EGTA) buffers were used for assaying the motility of kinesin, yeast dynein, and DDB, respectively. Motor-QD mixtures were flowed into the chamber, bound to the MT and washed to remove unbound motor and QD. For

experiments with antibody obstacles, dye- labelled kinesin-1 or BicDR1 were used. Finally, motor-specific buffer supplemented with 1 mg/mL casein, 1 mM tris(2-carboxyethyl) phosphine (TCEP), 100 μM ATP, glucose oxidase, catalase, and 0.8% dextrose were flown into the chamber. Run-length and velocity were determined by selecting the beginning and end of each trace in ImageJ. Cumulative frequencies of run lengths were fit to a single exponential function. Reported run lengths are the half-life values. The mobile fraction was calculated by dividing the number of moving motors over the total number of motors observed in the kymograph.

**Microscopy**

Microscopy was performed using a custom-built fluorescence microscope equipped with a Nikon Ti-E Eclipse microscope body, a 40X 1.15 NA long-working-distance water immersion objective (Nikon, N40XLWD-NIR), and a perfect focusing system[25]. The sample position was controlled by using an automated microscope stage (Microstage 20E, MadCityLabs). The sample was excited in the epifluorescence mode using 488, 561 and 633 nm laser beams (Coherent). Fluorescence image was split into two channels using OptoSplit2 (Cairn instruments) and detected by an electron-multiplied CCD Camera (Andor Ixon, 512x512 pixels).

**Single-molecule tracking and pause analysis**

Single-particle tracking was performed using Utrack [89]. Tracks were split into 1D motion along the long axis of the MT and perpendicular direction as described [25]. All tracks were manually reviewed to exclude tracks with jumps greater than 100 nm. Localization error was calculated using high pass filtering of the trajectories by calculating $x_i' = \frac{x_{i+1} - x_i}{\sqrt{2}}$, where $x$ is the position of the probe along the MT axis and *i* is the frame number. This operation omits unidirectional motility and pauses at lower frequencies, leaving only the Gaussian noise associated with the trace. $\sigma_{x'}$ is defined as the localization error. Under our imaging conditions, the localization error of QDs was typically between 20-40 nm (Figure 8). Pause analysis was performed as described[90]. Briefly, the track was divided into distance bins and the residence time within each bin was calculated. All non-zero residence times were fit to a single exponential decay. The residuals were then fit to a single exponential decay. The decay time and amplitude of this second fit were defined as the average pause time and pause density, respectively.

**Simulations**

Optimum running window averaging and bin size were calculated from simulated traces generated in MatLab. Experimentally determined noise, velocity and pause distributions were used to generate traces (Figure 8). A particle takes 8 nm unidirectional steps with exponentially distributed dwell times of 0.015 and 0.59 s, mimicking the characteristics times of processive motility and pausing of kinesin motors, respectively. The trace was then resampled to the imaging rate of 10 Hz. Random Gaussian noise was added to each position to introduce localization error. Simulations were used to determine whether the localization error in traces interferes with pause detection.

**Microfabrication**

PDMS bridges were generated using soft lithography [91,92]. Briefly, SU-8 2010 negative photoresist (Microchem) was spun on to a silicon wafer to 10 µm thickness. After a soft bake, the photoresist was exposed to UV light through a patterned, film photomask (Fine Line Imaging) on an OAI 200 Lithographic Mask Aligner. The pattern was developed after a hard bake using SU-8 developer (Microchem). To render the surface less adhesive, the master was treated with trichloro(1H,1H,2H,2H-perfluorooctyl)silane vapor. Sylgard 184 (Dow Corning) base and curing agent were mixed in a 10:1 ratio by mass and degassed. After pouring over the master, the PDMS was cured for 1 h at 80 °C (Figure 1_figure supplement 2). Features were confirmed with helium ion microscopy and scanning electron microscopy. The PDMS was then removed from the mask and baked for an additional 1 week at 80 °C. To extract low molecular weight species that diffuse to the surface and alter surface chemistry [93], PDMS was incubated, in sequence, with triethylamine, ethyl acetate, and acetone and allowed to dry overnight in an oven.

**MT bridges**

Silanization of PDMS was similar to glass with a few modifications. Ethanol was used as the solvent rather than acetone, as it is less likely to swell the PDMS [94]. The patterned surface was plasma oxidized at 50 W and 200 mTorr for 1 min. The slab was then immediately immersed in a 5% (v/v) solution of APTES in HPLC-grade ethanol (Sigma, 459828) for 20 min. After rinsing in 95% ethanol/water, the PDMS was baked 40 min on a hot plate. To remove unbound silane, PDMS was rinsed in pure ethanol and then water, and baked for an additional 40 min. Finally, PDMS was incubated for 1 h in an 8% glutaraldehyde solution. Excess glutaraldehyde was removed by rinsing in water and the functionalized PDMS was stored at room temperature for 1 week. To create a flow chamber, uncured PDMS was spin-coated on a coverslip to a thickness of 100 µm. After baking, a channel was cut in the PDMS-coated coverslip and the surface was plasma oxidized. The PDMS block with the bridge pattern was placed functional-side down on the coverslip, creating a flow cell (Figure 1_figure supplement 2). Motility assays were performed as described for single-molecule assays and the sample was imaged using a 1.4 NA oil-immersion condenser (Nikon) under brightfield illumination.

**Anti-GFP coating beads**

Latex beads were coated with anti-GFP antibody as described [82]. To prevent clumping of the beads when incubated with high concentrations of motors, we used "CML" beads (ThermoFisher, C37481), which have a high density of carboxyl groups that facilitates charge repulsion. 200 µL of 0.5 µm diameter CML beads (4% solids) were washed three times in activation buffer (10 mM MES, 100 mM sodium chloride, pH 6.0) by centrifugation for 6 min at 7,000 *g*. Final resuspension was in 200 µL activation buffer. Beads were then sonicated for 1 min in a bath sonicator (Vevor). Separately, fresh 4 mg/mL solutions of EDC (1-ethyl-3-(3-dimethyl aminopropyl)carbodiimide hydrochloride, ThermoFisher) and Sulfo-NHS (N-

hydroxysulfosuccinimide) were prepared in water. 5 μL each of fresh EDC and Sulfo-NHS solutions were added to the beads. Beads were sonicated for 1 min and nutated for 30 min at room temperature. After three washes in PBS, beads were resuspended in 200 μL PBS and mixed with 200 μL 0.4 mg/mL anti-GFP antibody overnight with nutation. Custom-made anti-GFP antibodies (Covance) were purified by GFP affinity chromatography. The beads were passivated by incubating with 10 mg/mL bovine serum albumin (BSA) overnight. Finally, beads were washed 5 times in PBS and stored at 4 °C with 1 mg/mL BSA supplement.

**Bead motility assay**

For bead motility assays, anti-GFP beads were diluted two-fold in water and sonicated for 1 min to disperse the beads. GFP-tagged kinesin motors were incubated with beads for 10 min. The excess motor was then washed from the beads by diluting the mixture into 100 μL BRB80 supplemented with 1 mg/ml casein (BRB-C) and centrifugation at 8,000 *g* for 3 min. The supernatant was removed and the pellet was resuspended in 15 μL BRB-C supplemented with 1 mM TCEP, 100 μM ATP, glucose oxidase, catalase, and 0.4% dextrose. Beads were then flown into a flow chamber after surface-immobilization of biotinylated MTs. DDB experiments were performed similarly with a few exceptions. The GFP handle was on the cargo adaptor (BicD2N-GFP). We used a dynein mutant that does not form the autoinhibited phi-conformation[27] to facilitate assembly of the DDB complex. 1 μL each of 1 μM human dynein complex, pig brain dynactin, and BicD2N-GFP were mixed at a 1:1:1 molar ratio and incubated for 15 min before mixing with the beads. The mixture was pelleted at 8,000 *g*, resuspended in 15 μL MB supplemented with 1 mg/mL casein, 1 mM TCEP, 100 μM ATP, glucose oxidase, catalase and dextrose and added to the flow chamber.

**Statistical Analysis**

Each measurement was performed with at least three independent replicates, and the exact number of repetitions is reported for each experiment. Each statistical analysis method is explicitly stated in the main text and/or figure legend. “n” refers to the number of motors analyzed across all experimental replicates. “Independent experiments” mean data collected on different days using the same protein preparation. However, all major findings were repeated with multiple different protein preparations. Standard deviations (SD) represent differences between independent experiments. When reported, standard error (SEM) refers to the error of the fit.

**Figures**

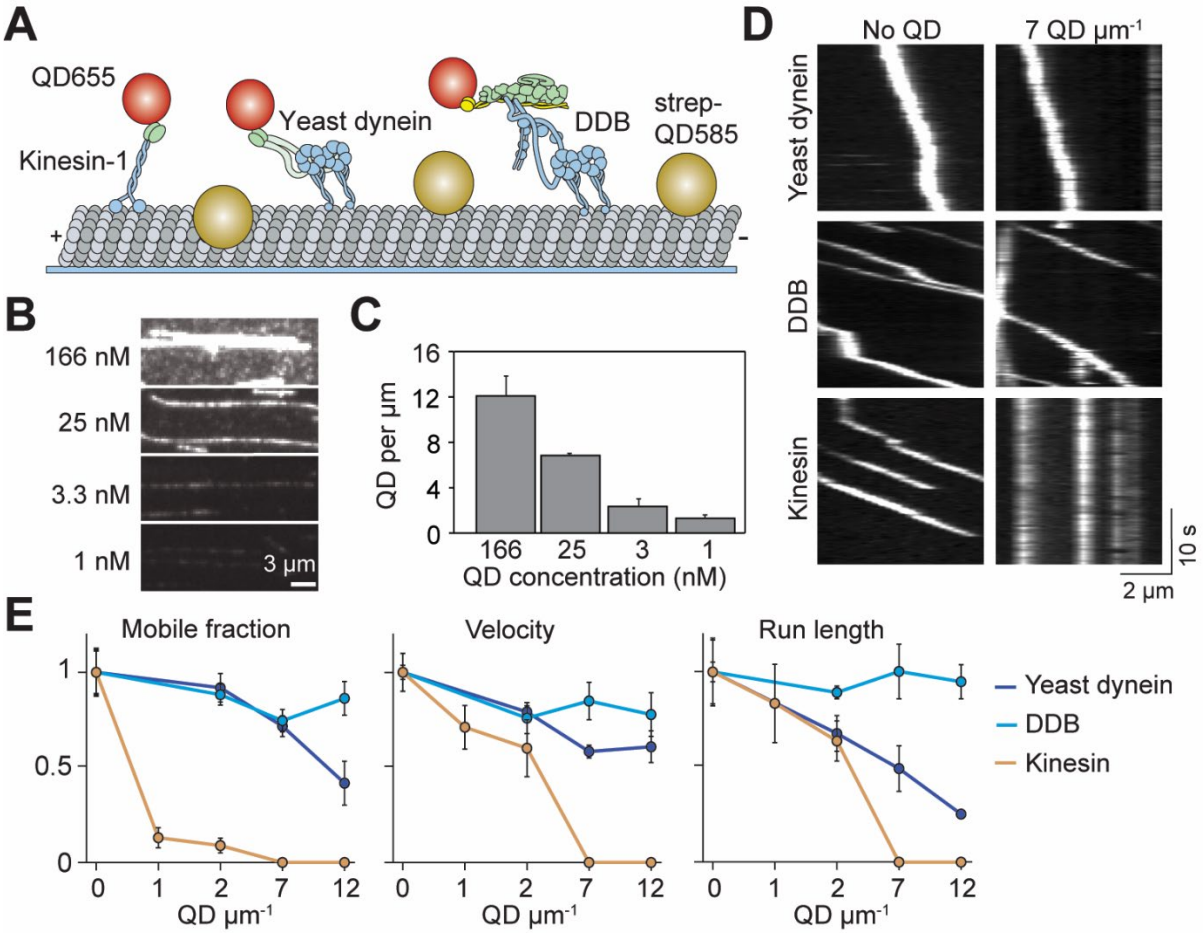


**Figure 1 Single dynein, but not kinesin, motors bypass QD obstacles. (A)** Schematic of single-molecule motility assays on surface-immobilized MTs decorated with streptavidin-coated QD585 obstacles. Human kinesin-1, yeast dynein, and DDB are labeled with QD655 at their tail domain. **(B)** Example fluorescent images of QD585 obstacles on MTs at different QD concentrations. **(C)** The linear density of QDs on MTs at different QD concentrations (mean ± SD, from left to right $n$ = 97, 98, 104 and 90 MTs from two technical replicates). **(D)** Kymographs show the motility of QD655-labeled motors on MTs with or without QD obstacles. QD585 signal is not shown. **(E)** Mobile fraction, velocity and run length for all three motors were normalized to the no QD condition (mean ±SD, three independent experiments). Run-length values represent decay constants derived from a single exponential decay fit. From left to right, $n$ = 271, 423, 405 for kinesin, 315, 407, 197, 168 for yeast dynein, and 636, 502, 356, 509 for DDB.

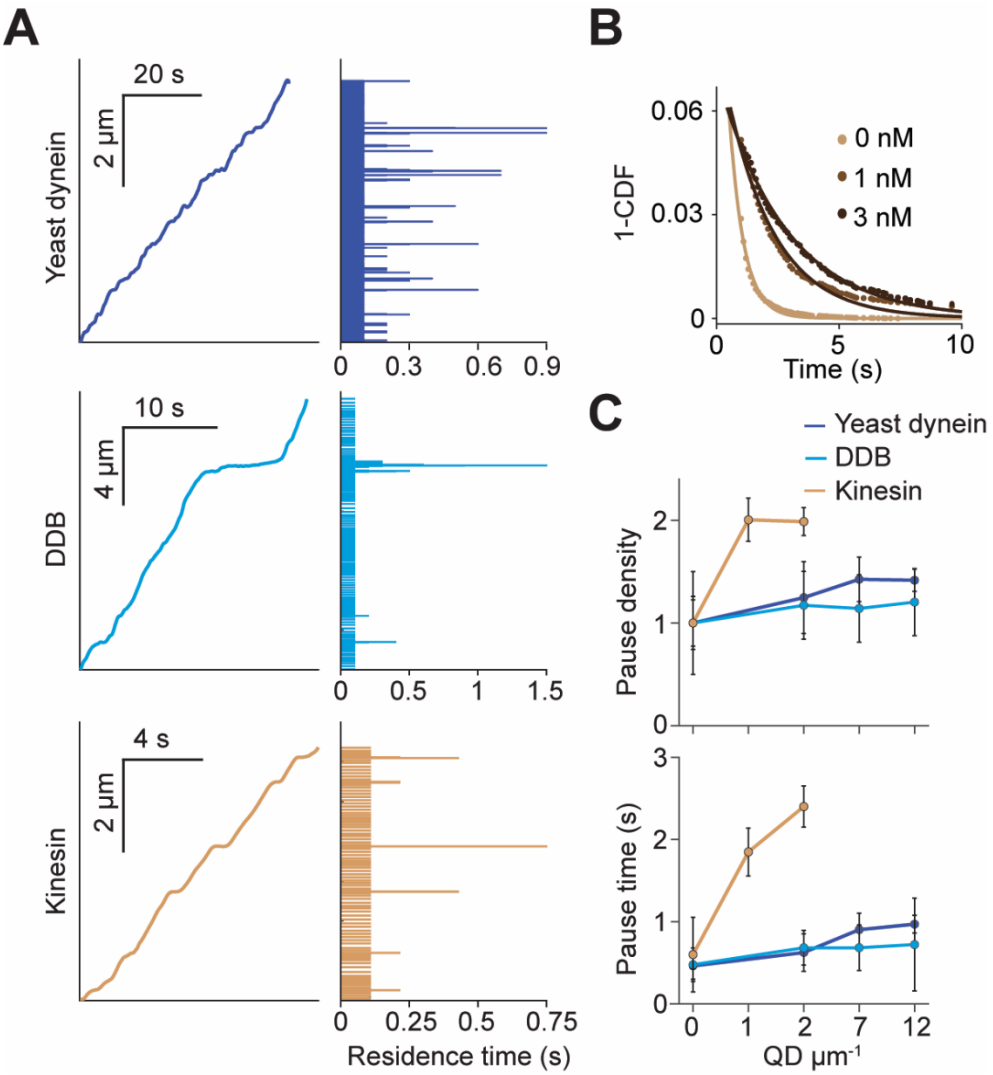


**Figure 2 Kinesin pauses more frequently than dynein when encountering QD obstacles. (A)** (Left) Representative traces of yeast dynein, DDB, and kinesin in the absence of QD obstacles on surface-immobilized MTs. (Right) Residence times of the motors in each section of the traces. **(B)** The inverse cumulative distribution (1-CDF) of kinesin residence times at different obstacle concentrations were fit to a single exponential decay. The residuals of that fit (shown here) are fit to a single exponential decay (solid line) to calculate the density and duration of kinesin pausing. **(C)** Density and duration of the pauses of the three motors. Pause densities (pauses/µm) are normalized to the 0 QDs $\mu m^{-1}$ condition. Kinesin pausing behavior at 7 and 12 QDs $\mu m^{-1}$ could not be determined because the motor was nearly immobile under these conditions. From left to right, $n$ = 535, 520, 158, 29 for yeast dynein, 511, 449, 391, 276 for DDB, and 570, 127, 112 for kinesin. Error bars represent SEM calculated from single exponential fit to residence times.

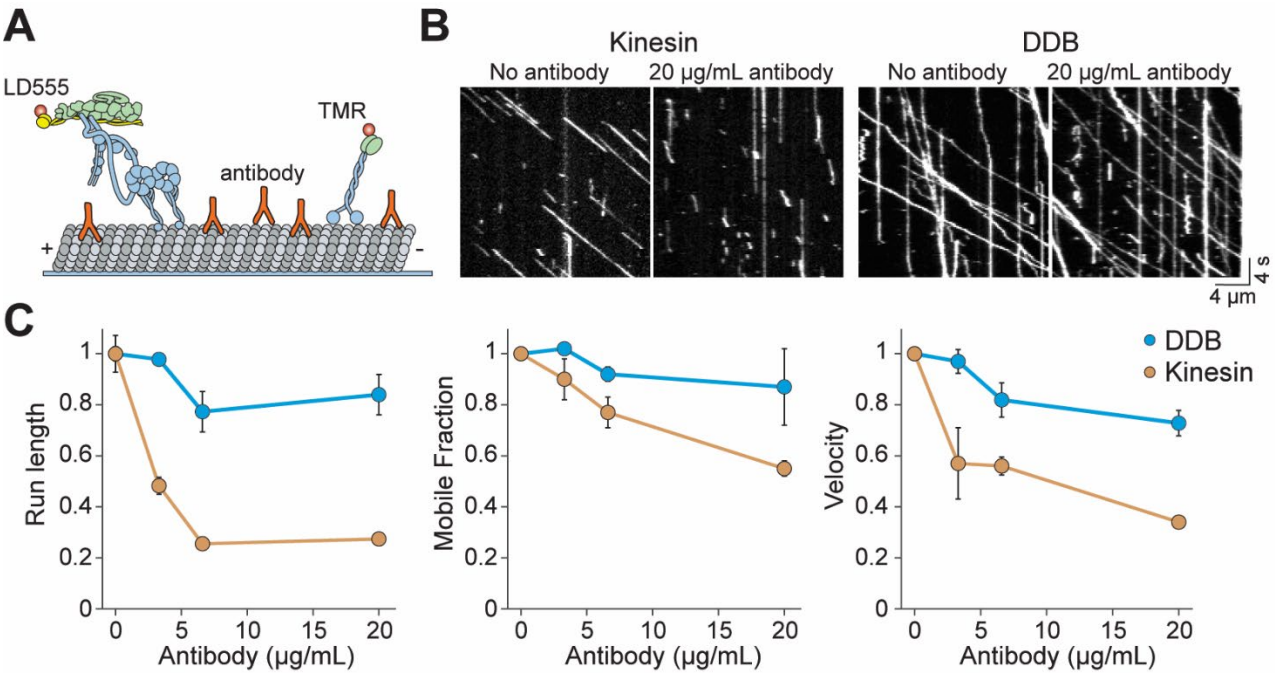


**Figure 3 Kinesin detaches from MTs when encountering antibody obstacles. (A)** Kinesin and dynein were labeled with organic dyes and their motility was tested in the presence and absence of anti-tubulin antibody on MTs. **(B)** Kymographs of TMR-kinesin and LD555-DDB walking on MTs in the absence and presence of 20 µg/mL antibody obstacle. **(C)** Quantification of how antibody obstacles affect motor motility. All data are normalized to the no antibody condition (mean ± SD, two independent experiments). From left to right, *n* =185, 232, 199, 197 motors for kinesin and 104, 224, 262, 308 motors for DDB.

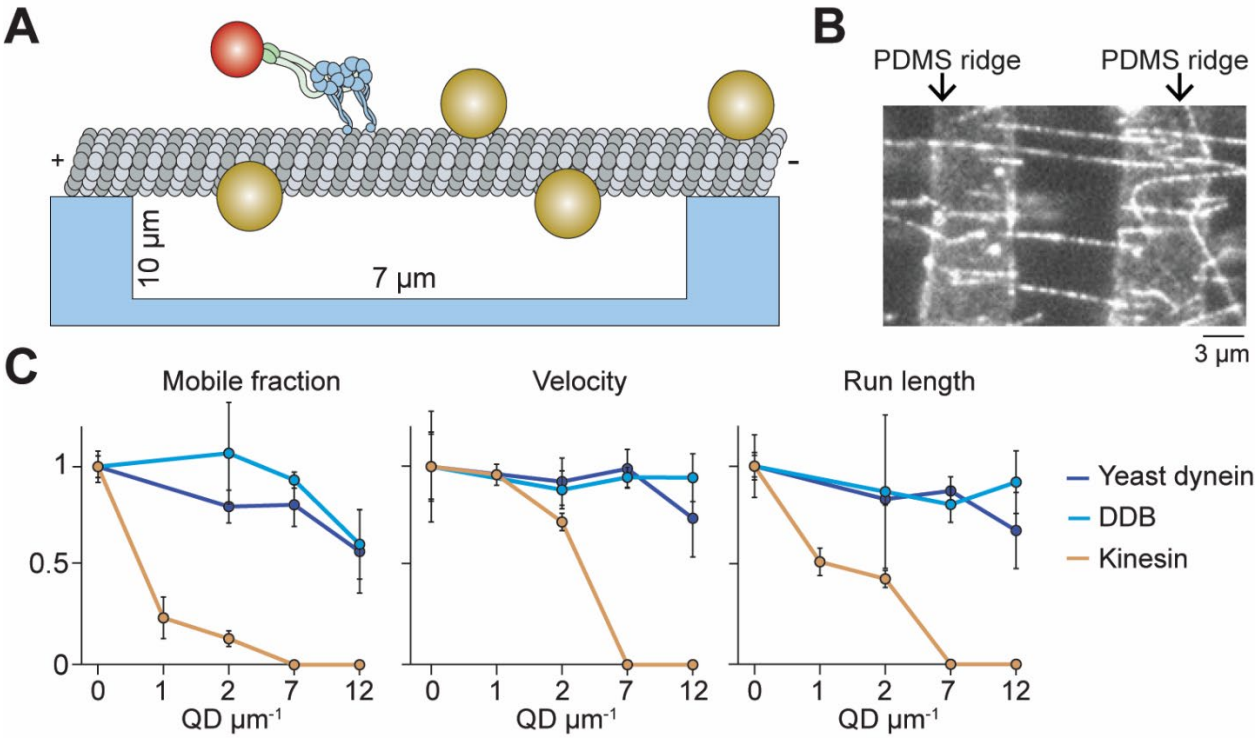


**Figure 4 Suspending MTs from the surface does not aid kinesin in avoiding obstacles. (A)** Schematic of a single-molecule motility assay on MT bridges coated with QD obstacles (not to scale). **(B)** An example image of Cy5-labeled MT bridges in the microfabricated chamber. PDMS ridges (arrows) are visible due to the autofluorescence. **(C)** Mobile fraction, velocity and run length of motors along MT bridges were normalized to no QD condition (mean ±SD, three independent experiments). From left to right, *n* = 199, 187, 106 for kinesin, 129, 107, 163, 135 for yeast dynein, and 192, 206, 330, 276 for DDB.

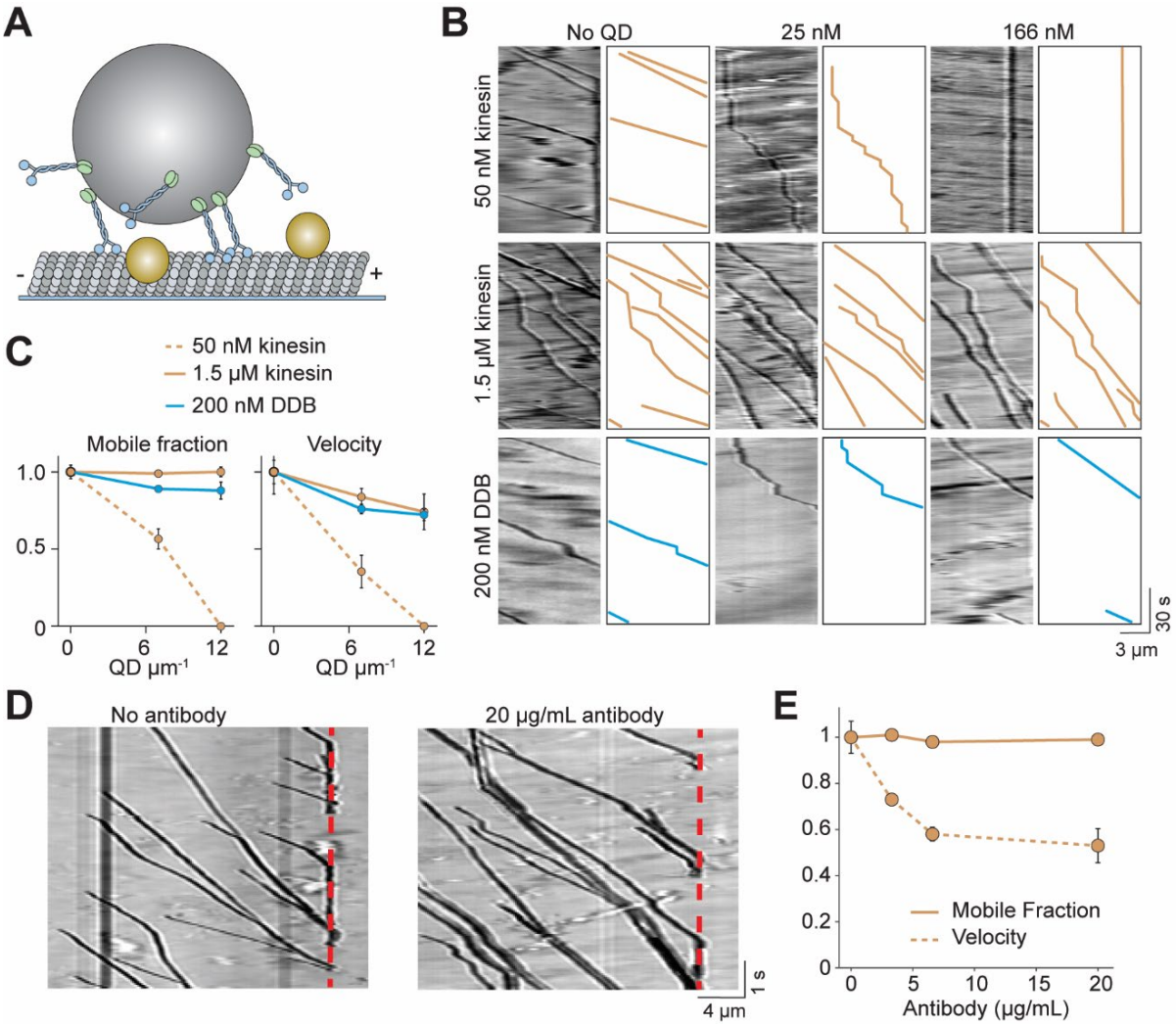


**Figure 5 Cargos driven by multiple kinesins successfully bypass obstacles. (A)** Schematic of bead motility driven by multiple motors along surface-immobilized MTs decorated with QD obstacles (not to scale). **(B)** Kymographs reveal the motility of beads coated with kinesin or DDB in the presence and absence of QD obstacles. Diffusion of unattached beads creates a background in the kymograph. To the right of each kymograph is an illustration of the bead motility on the MT. **(C)** Mobile fraction and velocity of beads were normalized to the no QD condition (mean ± SD). From left to right, *n* = 154, 189 bead traces for 50 nM kinesin, 323, 338, 336 for 1.5 µM kinesin, and 279, 184, 67 for DDB from three independent experiments. **(D)** Representative traces for 1.5 µM kinesin on beads in the absence and presence of antibody obstacle. The dashed red line indicates the plus-end of the MT. **(E)** Quantification of mobile fraction and velocity of kinesin-driven beads. From left to right, n=145, 198, 141, 201 beads.

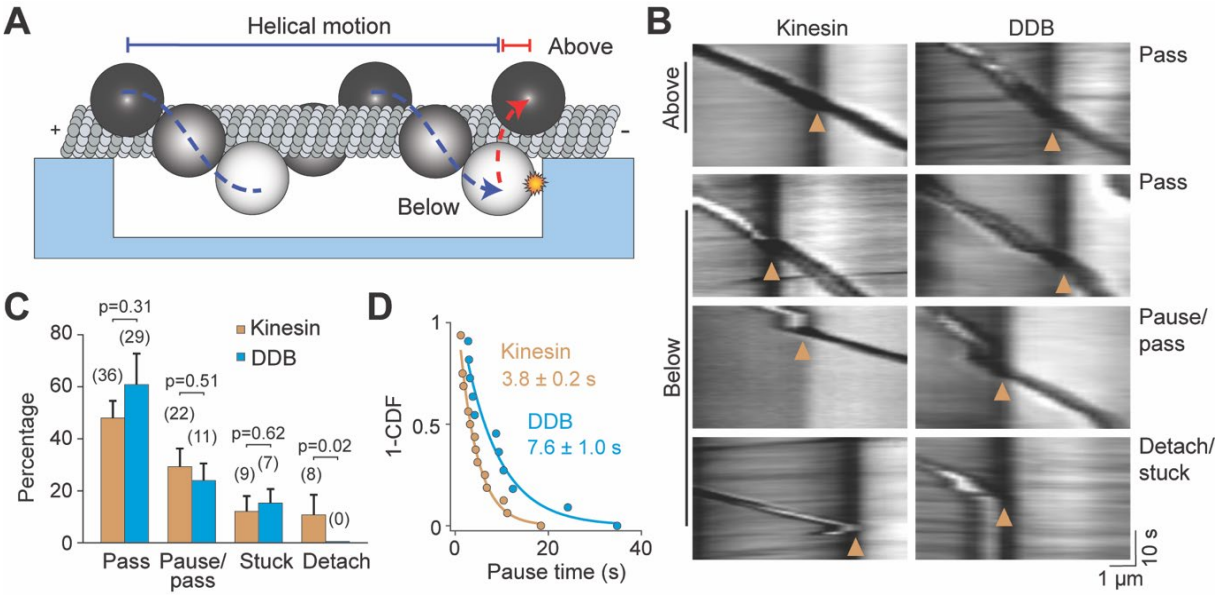


**Figure 6 Cargos driven by multiple motors bypass large obstacles by rotating around the MT. (A)** Schematic of multi-motor bead motility on MT bridges. The position of the bead in the *z*-axis is determined from changes in bead intensity under brightfield illumination. If a bead is positioned below the MT when it reaches the PDMS wall, it must move to the top of the MT (red dotted curve) before continuing forward. **(B)** Kymographs reveal how beads driven by kinesins and DDBs move when they encounter the PDMS wall (Below). (Pass) The bead rotates around the MT as evidenced by light to dark transition in the bead intensity at the wall before continuing forward. (Pause/pass) The bead paused for more than 1 s at the wall before rotating around the MT and moving forward. (Detach/stuck) The bead failed to pass the wall and either detached (left) or got stuck on an MT (right). **(C)** The percentage of the pass, pause/pass and detach/stuck events for the beads positioned below the MT when they encounter the PDMS wall (mean ± SD, two independent experiments). The number of beads is shown in parentheses. p-values are calculated using two-tailed t-test for pass, pause/pass and stuck, and z-score calculation for detach. **(D)** The inverse cumulative distribution of pause times for kinesin and DDB beads. A fit to a single exponential decay (solid curves) revealed that pause duration of DDB-driven beads is longer than kinesin-driven beads (F-test, $p = 0.0001$, $n = 16$ pauses for kinesin and 11 for DDB).

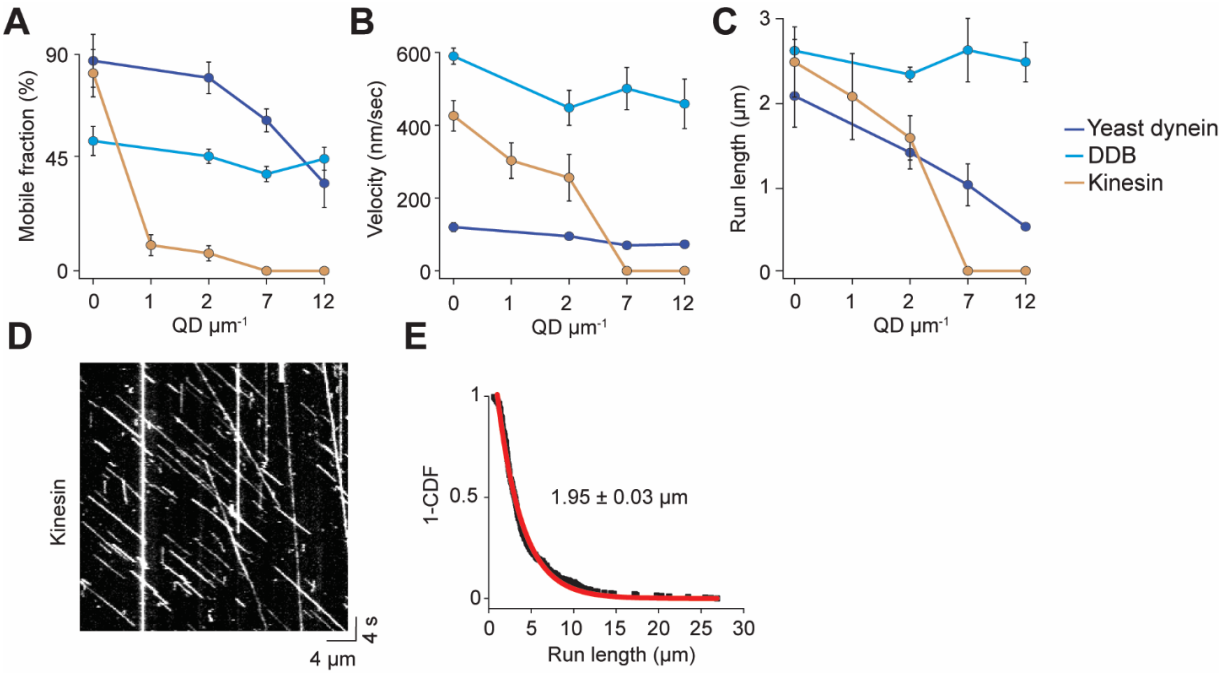


**Figure 7. Analysis of single-molecule trajectories on surface-immobilized MTs without normalization**. **(A)** Mobile fraction, **(B)** velocity and **(C)** run length of single motors on surface-immobilized MTs in the presence of QD obstacles (mean ± SD). From left to right, $n$ = 271, 423, 405 for kinesin, 315, 407, 197, 168 for yeast dynein, and 636, 502, 356, 509 for DDB, three independent experiments. **(D)** A representative kymograph of TMR-kinesin motility in the absence of obstacles on surface-immobilized MTs. The assay was performed in 1 mM ATP. **(E)** The inverse cumulative distribution of distances traveled by single TMR-kinesins was fit to a single-exponential decay to calculate the motor run length (mean ± SEM, $n$ = 422 traces from two independent experiments)

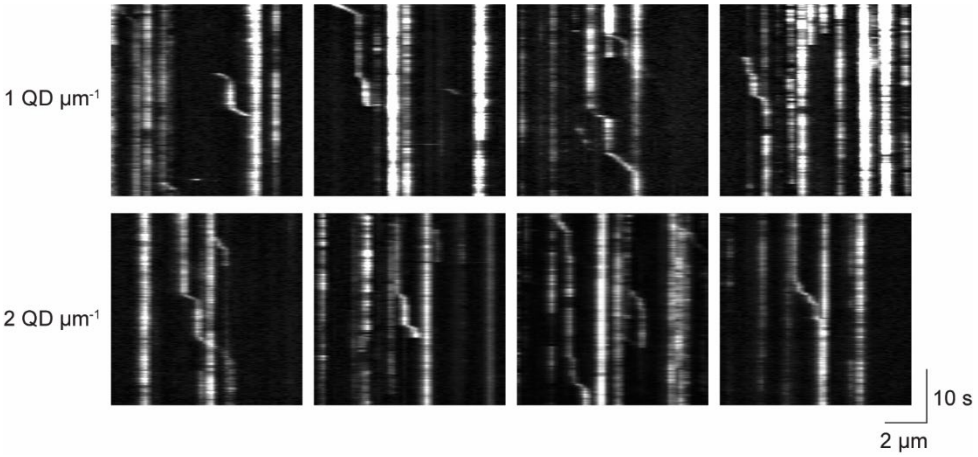


**Figure 8. Kinesin pauses in the presence of QD obstacles.** Representative kymographs reveal frequent pauses in kinesin motility in the presence of 1 QD $\mu m^{-1}$ (top row) or 2 QD $\mu m^{-1}$ (bottom row). Most pauses were permanent throughout recording. Processive traces interspersed with transient pauses were used in pause analysis in Figure 2.

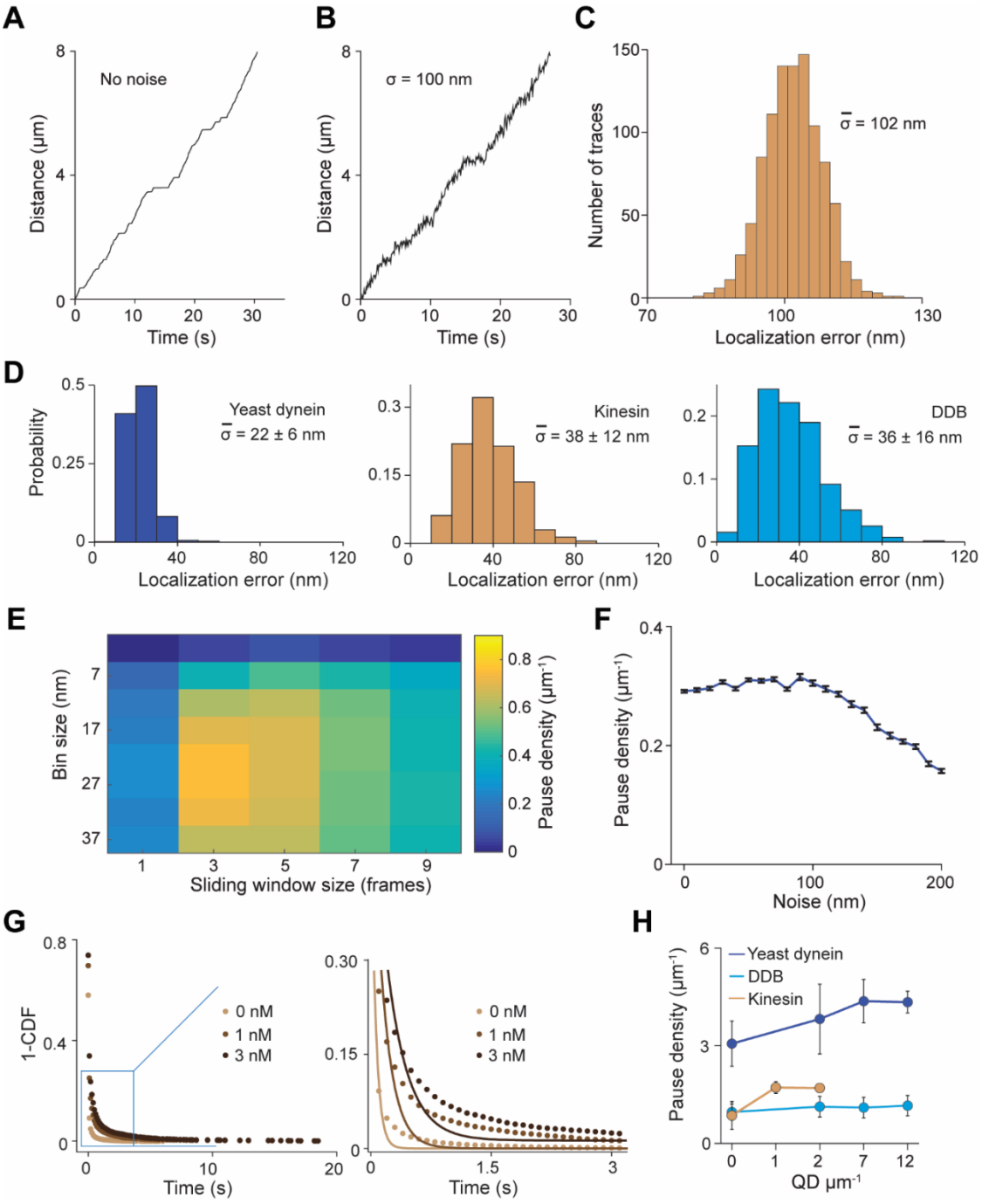


**Figure 9. Simulations for the pause analysis.** **(A)** An example trajectory simulated with a pause density of 0.8 $\mu m^{-1}$ in the absence of tracking noise (see Methods for the parameters used to generate these trajectories). **(B)** An example trajectory simulated with 100 nm root mean squared (RMS) noise. **(C)** Localization error calculated for 1,000 simulated traces closely agrees with 100 nm noise added to the traces. **(D)** Localization error calculated for 500 experimental traces of the three motors. **(E)** Optimization of the bin size and sliding window size for the pause analysis. Noisy traces were simulated using 0.8 $\mu m^{-1}$ pause density, down-sampled with given

window size (the number of data points) and residence time was calculated for a given bin size (distance traveled by motor). The analysis revealed that pause density was slightly underestimated even under optimum conditions. The combination of bin size and window size that resulted in the highest pause density was used to analyze experimental traces. **(F)** Traces were simulated with a pause density of 0.3 $\mu m^{-1}$. Calculated pause density from simulations was insensitive to the 0-100 nm added tracking noise. The density of detected pauses decreases at higher noise. **(G)** The inverse cumulative distribution of pause density and duration were determined from residence time histograms through a two-step process. (Left) All non-zero residence times were fit to a single exponential distribution. (Right) Zoomed view of the blue rectangle on the left. The residuals of this fit (plotted in Figure 2B) were fit to a single exponential decay to determine pause time and density. **(H)** The pause density analysis of single motors on surface-immobilized MTs without normalization. From left to right, $n$ = 535, 520, 158, 29 for yeast dynein, 511, 449, 391, 276 for DDB, and 570, 127, 112 for kinesin. Error bars represent SE calculated from single exponential fit to residence time histograms.

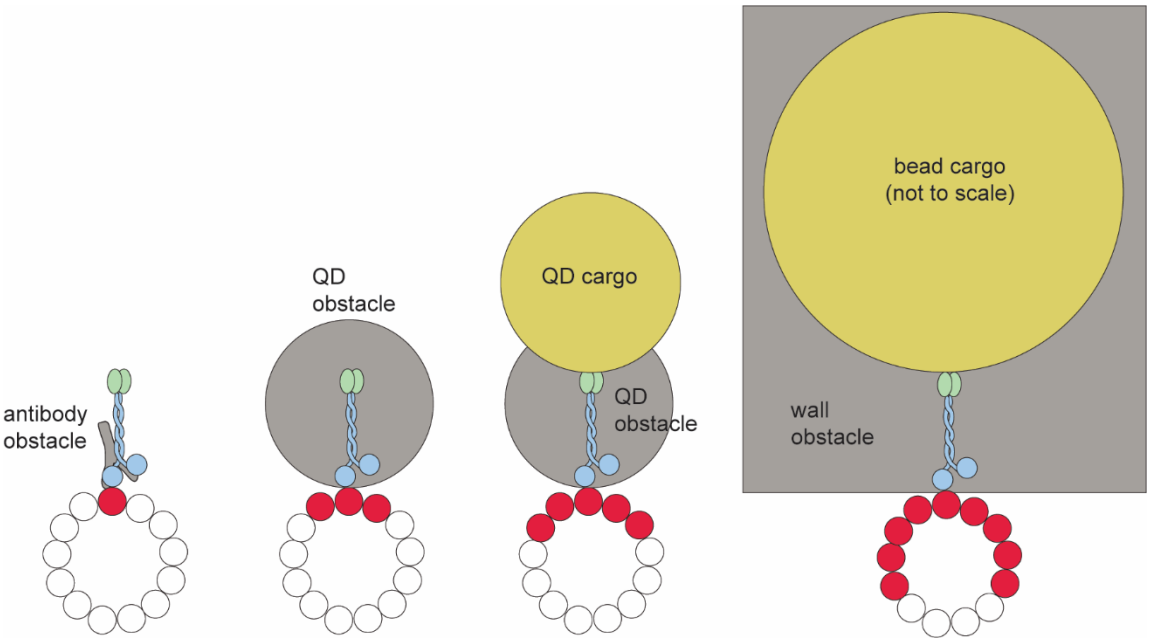


**Figure 10. Larger obstacles block access to more protofilaments on an MT.**
The schematics represent the cross-sectional view of a motor bypassing an obstacle by taking sideways steps on an MT. Increasing the size of the obstacle or the cargo attached to the motor is expected to reduce the number of protofilaments that support motility (white). The protofilaments that are blocked by the obstacle/cargo are shown in red.

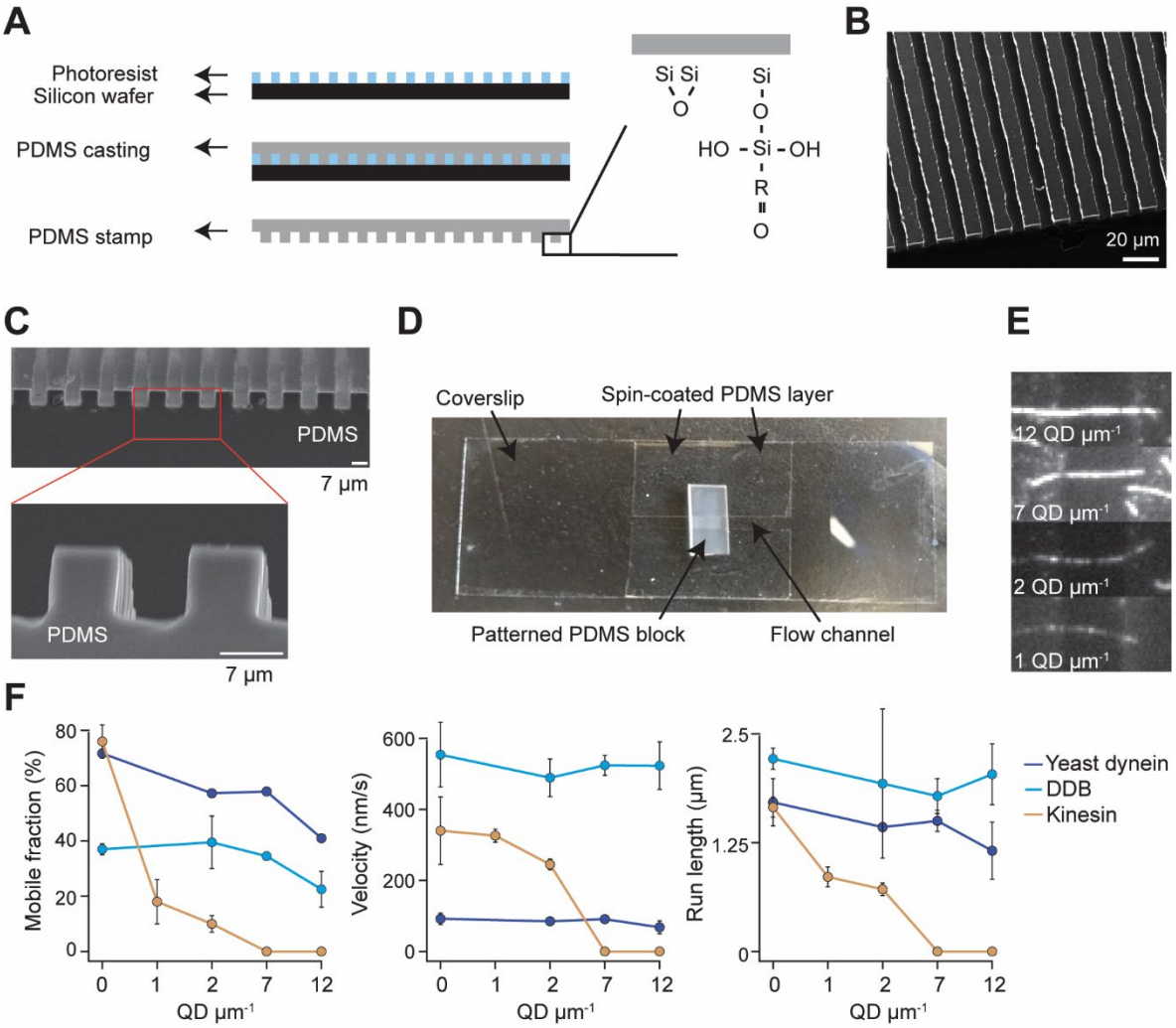


**Figure 11. Chamber design and raw data of single-molecule motility along MT bridges. (A)** Workflow for bridge microfabrication. The photoresist is spun and patterned on a silicon wafer. PDMS is then cast on top of the photoresist and silanized to produce a reactive surface. **(B)** Helium ion microscopy shows a top view of patterned PDMS. **(C)** Scanning electron microscopy shows the side view of patterned PDMS (top) and the zoomed view of this image reveals that the walls have sharp edges (bottom). **(D)** Image of the flow chamber used for experiments. **(E)** Example fluorescent images of QD585 obstacles on MT bridges at different QD concentrations. **(F)** Mobile fraction, velocity and run length of single motors on MT bridges without normalization (mean ± SD, two independent experiments). From left to right, $n$ = 199, 187, 106 for kinesin, 129, 107, 163, 135 for yeast dynein, and 192, 206, 330, 276 for DDB.

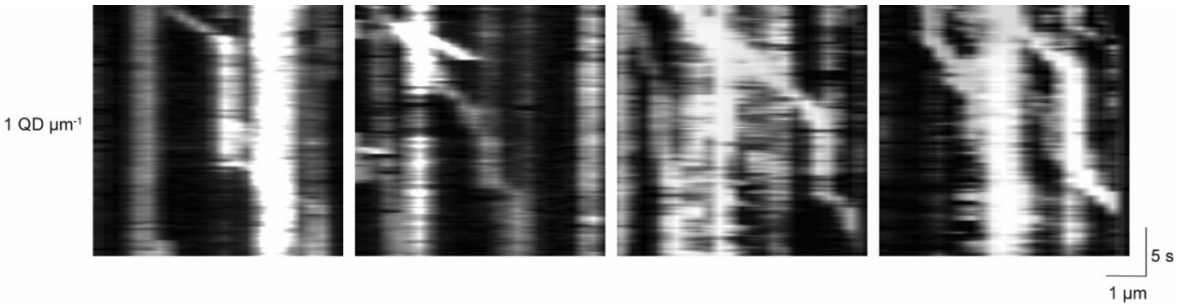


**Figure 12. Kinesin pauses in the presence of QD obstacles on suspended MTs.**
Representative kymographs reveal frequent pauses in kinesin motility in the presence of 1 QD $\mu m^{-1}$ on suspended MT bridges. Most pauses were permanent throughout recording.

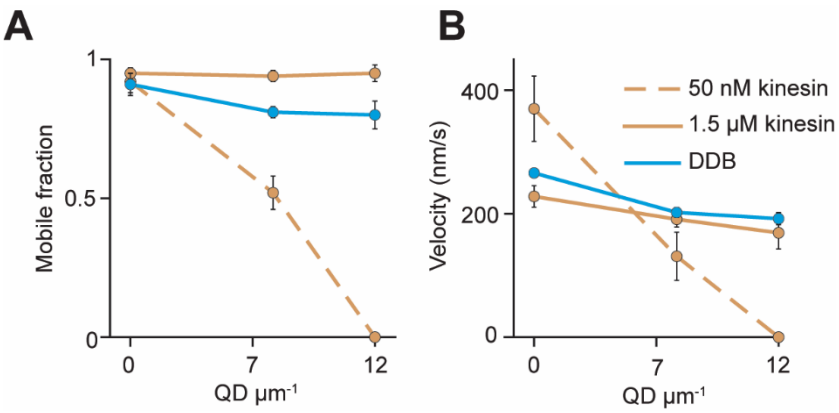


**Figure 13. The analysis of beads driven by multiple motors on surface-immobilized MTs without normalization. (A)** Mobile fraction and **(B)** velocity of beads driven by multiple motors on surface-immobilized MTs in the presence of QD obstacles (mean ± SD, three independent experiments). The mobile fraction of the beads was higher than 95% in the absence of QD obstacles. From left to right, $n$ = 154, 189 traces for 50 nM kinesin, 323, 338, 336 traces for 1.5 μM kinesin, and 279, 184, 67 traces for 200 nM DDB.

## Chapter III: Positive charge on the microtubule-binding domains of tau and MAP7 inhibits motor proteins

*The work presented in this section is unpublished data by authors: Luke S Ferro*, Lisa Eshun-Wilson*, Mert Gölcük, Jonathan Fernandes, Teun Huijben, Eva Gerber, Qianglin Fang, Amanda Jack, Katelyn Costa, Mert Gür, Eva Nogales, Ahmet Yildiz*

**equal contribution*

### Abstract

Microtubule (MT)-associated proteins (MAPs) regulate intracellular transport by affecting motor-based transport. The mechanism of this regulation has been attributed to an overlap between motor and MAP binding sites. We tested this model by investigating how MAP7, tau, and DCX affect MT motors using single-molecule and cryo-electron imaging *in vitro*. We found that all three MAPs inhibit both kinesin-1 and cytoplasmic dynein, except MAP7 that regulates kinesin-1 motility in a biphasic fashion. MAP7 projection domain activates kinesin-1 motility by interacting with its stalk, whereas the MAP7 MT-binding domain (MTBD) inhibits kinesin by overlapping with its MT binding site. Remarkably, tau and DCX inhibit dynein without an overlap. Instead, positive charges on tau's MTBD prevent MT binding of dynein by competing for negatively-charged residues on the MT surface. Our results exclude the steric overlap model and suggest that motors are required to make favorable interactions with a MAP to walk on MAP-coated MTs.

### Introduction

Kinesin-1 (hereafter kinesin) and cytoplasmic dynein (dynein hereafter) are dimeric, force-generating motors that transport organelles, vesicles, and nucleoprotein complexes to the plus- and minus-end of microtubules (MTs), respectively [1,2]. These motors have fundamental roles in neurobiology and development, and mutations that impair dynein or kinesin driven transport lead to developmental and neurological diseases. Although these motors perform complementary cellular functions, they have different structural and mechanistic features (Figure 14A). Kinesin heavy chain is related to G-proteins, contains a single ATP-binding site, and directly binds to the MT [1], whereas dynein heavy chain contains a large AAA+ ring that connects to its MTBD through a 15 nm long coiled-coil. To prevent futile cycles of ATP hydrolysis, these motors are autoinhibited when not transporting a cargo. Kinesin is autoinhibited by the folding of its tail domain onto the motor domain [28,29]. In contrast, dynein is inhibited by self-dimerization of its motor domains and is activated when one or two dyneins assemble with dynactin and a cargo adaptor protein [20,27 21,22].

Many intracellular cargos simultaneously recruit kinesin and dynein, but the molecular cues that govern motor activity and determine where these cargos are delivered remain unclear. Previous models proposed that the direction of the cargo movement is determined by mechanical competition or by reciprocal inhibition of the motors on a cargo [31]. However, recent studies have suggested that motors can be regulated by the MT surface [58,95]. In cells, motors are challenged to transport cargoes in the presence of structural MT defects, intersecting cytoskeletal elements, macromolecular crowding, stationary organelles, and diversity of non-motor MAPs [37,39,40]. *In vitro* studies showed that dynein can bypass large obstacles efficiently due to its ability to take sidesteps [96]. Kinesin walks without frequent sidesteps, and it stops or detaches when encountering an obstacle, [23,24,73]. While kinesin can bypass obstacles when working in a team with other kinesin motors [96,97], it remains to be determined whether sidestepping and teaming up of motors are effective strategies to bypass the high density of MAPs that naturally coat the MT surface.

Structural MAPs, such as tau, MAP2, MAP4, DCX, MAP7, and MAP9, are a family of proteins that regulate MT dynamics, organelle transport, cell polarity, and axon morphogenesis by binding to the MTs [11,13]. MAPs are anchored to the MT by positively-charged MTBDs. Tau and MAP4 bind on the outer-most crest of MT protofilaments, while EB1 and DCX bind between protofilaments [49,54,98]. MT binding sites of MAPs affect how they regulate MT structure and dynamics [49,50]. A disordered projection domain extends from the MT surface [99] and spaces out MTs [100]. The projection domains can also drive for the formation of MAP condensates on the MT surface, as seen for tau and TPX2 [59,66,67]. It is not well understood how either the MTBDs or projection domains of MAPs affect motor activity on the MT.

Motors and MAPs are challenged to carry out their functions while competing for space on the MT surface. Despite differences in domain organization, charge distribution, level of disorder, and length, MAPs are generally inhibitory to motors *in vitro* [39,101,102]. Kinesin-1 is inhibited by tau, DCX, MAP2, and MAP9 [39,58,103]. Dynein is inhibited by MAP2, MAP4 and MAP9 [39,52,102], but not by nanomolar concentrations of either tau or MAP7 in vitro [58,59]. However, the concentration of tau in neurons is estimated to be 1-20 μM [104] and it remains unknown if dynein remains active at such high levels of tau.

MAPs can also recruit specific motors to MTs. For example, kinesin-1 and kinesin-3 driven transport depend on the presence of MAP7 and DCX in cells, respectively [48,54]. In these motor/MAP combinations, the motor makes a specific interaction with the MAP [53,54,58]. Activation of motors by specific MAPs has given rise to the concept of a "MAP code," similar to the histone code, in which MT decoration by MAPs governs the recruitment and activity of motors along these tracks [39]. However, the mechanism by which MAPs affect motor activity is still emerging. The current model proposes that MTBDs of MAPs block the access of motors to the MT by overlapping with their binding sites [39]. Alternatively, condensates formed by the IDRs

could function as a selectivity barrier to control access of specific motors to the MT. Consistent with this latter model, tau condensates prevent the binding of kinesin to the MT [59,66]. Understanding interactions between motors and MAPs on the MT surface is critical to deciphering how intracellular transport is regulated in health and disease.

In this study, we seek a mechanistic understanding of how MAPs affect motor activity using single-molecule imaging, cryo-electron microscopy (cryoEM), and all-atom molecular dynamics (MD) simulations. Specifically, we investigated how MAP7, tau, and DCX regulate kinesin and dynein motility *in vitro*. MAP7 activated kinesin in a biphasic manner and inhibited dynein, allowing it to regulate the direction of motion for kinesin/dynein ensembles. In comparison, tau and DCX strongly inhibited both kinesin and dynein motility. We found that the MTBDs of these MAPs are inhibitory to both motors. Surprisingly, this inhibition does not necessarily require a direct overlap between the footprints of the motor and the MAP on the MT surface. In the absence of such overlap, positively-charged residues on tau MTBD prevent dynein to stably dock onto the negatively-charged MT surface. These observations are not compatible with the steric overlap model and suggest a different mechanism for how MAPs regulate access of motors to the MT.

## Results

### MAP7 and tau differentially affect kinesin and dynein motility

Full-length human MAP7 and tau were expressed in insect cells and fluorescently labeled with a ybbR tag [105] (Figures 1B and S1A-B). In the absence of MTs, both tau and MAP7 formed liquid droplets in solution (Figure 14C) [68,104], with half-saturation concentrations ($k_{sat}$) of 39.9 ± 0.3 and 15 ± 2 μM, respectively (Figure 14D). Tau could also enter MAP7 droplets with a partition coefficient of 2.6 ± 0.2 (Figure 21C-D). We next monitored how MAP7 and tau decorate taxol-stabilized MTs immobilized to polyethylene glycol (PEG)-coated coverslips. As previously reported [59,66], tau formed liquid condensates on the MT surface. We observed these condensates at micromolar concentrations of tau under physiological salt (150 mM KAc) (Figure 21E). With increasing tau concentrations, these condensates grew and merged until the MT surface was saturated (Figure 14E). Unlike tau, MAP7 did not form liquid condensates and uniformly decorated the MT surface (Figure 14E)[53]. MAP7 bound the MT more strongly than tau, with a dissociation constant ($K_D$) of 111 ± 12 nM, compared to 4.9 ± 0.5 μM for tau (Figure 14F). While tau and MAP7 coexisted in droplets (Figure 21C), MAP7 inhibited tau binding to the MT surface with a half-maximal inhibition ($IC_{50}$) of 270 ± 18 nM (Figure 21F-I)[58]. Therefore, MT binding strongly alters the interactions between MAP7 and tau.

We next tested how MAPs affect the motility of active human kinesin-1 (K560, amino acids 1-560) and the mammalian dynein-dynactin-BicDR1 complex (DDR) [27,77]. Because motors quickly dissociate from MTs and exhibit very short runs at physiological salt concentrations *in vitro*,

their motility has mostly been studied at low salt. We found that the addition of 0.1% methylcellulose (a crowding agent) enabled K560 and DDR motors to walk in 150 mM KAc, with velocities of 829 ± 27 and 651 ± 100 nm $s^{-1}$, respectively (mean ± s.d., Figures 1H-J and S1J). We used these conditions to study MAP-motor interactions at physiological salt.

We first investigated how tau affects kinesin and dynein motility. MT decoration by tau reduced the run frequency and run length of K560 motors (Figure 14G-H, Movie S1), as previously reported [56,103,106]. Surprisingly, tau also inhibited DDR motility. The half-maximal inhibition value ($IC_{50}$) was 1.2 ± 0.2 μM tau for dynein and compared to 1.1 ± 0.1 μM tau for kinesin (Figure 14H). This finding is in contrast to a previous report that mammalian dynein is not inhibited by 0.5 nM tau in the absence of salt [59]. We confirmed that tau was also inhibitory to both motors in the absence of added salt (Figure 22A-D) and K560 and DDR both detached when they encountered a tau condensate on the MT (Figure 22E-I). We also tested whether multiple motor assemblies more successfully walk on tau-coated MTs [96]. Beads driven by multiple K560s or DDRs were also inhibited by tau (Figure 22J-L), suggesting that teaming up of motors is not an effective solution to navigate a cargo on MAP-coated MTs.

Unlike tau, the addition of 50 nM MAP7 increased K560 run frequency and run-length by 4-fold, as previously reported [39,53] (Figure 14I-J, Movie S2). However, how MAP7 affects kinesin motility at higher concentrations remained unknown. We increased the MAP7 concentration to near its saturation concentration on the MT (~1 μM) and observed that MAP7 has a biphasic effect on K560 run frequency and length (Figure 14I-J). K560 run frequency peaked around 50 nM MAP7 and then slowly declined as MAP7 concentration increased. While previous work concluded that MAP7 does not affect dynein motility [58], we found that run frequency and run-length of dynein sharply declined with increasing MAP7 (Figure 14I-J, Movie S3). $IC_{50}$ of run frequency was 11.9 ± 0.9 nM MAP7 (±s.e.), a concentration 10-fold below the $K_D$ of MAP7. For both K560 and DDR, velocity declined gradually as MAP7 concentration increased (Figure 14H-J), likely due to crowding of the MT surface. Together, we concluded that tau inhibits both kinesin and dynein, whereas MAP7 inhibits dynein and regulates kinesin motility in a biphasic manner.

**Biphasic regulation of kinesin motility by MAP7**

Biphasic regulation arises when an enzyme is subjected to simultaneous activation and inhibition which dominate at different concentrations [107]. The run frequency of K560 under different MAP7 concentrations (Figure 14J) fit well to a two-component Hill equation, with one activation component and one inhibition input (Figure 15A). The activation concentration was nearly 1,000-fold lower than the inhibition concentration, enabling robust kinesin motility under a wide range of MAP7 concentrations (Figure 15A). To understand the source of these opposing inputs, we first tested whether the biphasic effect was also observed with full-length (FL) kinesin (Figure 15B). Unlike K560, FL kinesin is autoinhibited by folding of its C-terminus onto the

motor domains [28,29], and exhibit poor motility (Figure 15D). MAP7 has been shown to activate FL kinesin by interacting with its coiled-coil stalk (Figure 15C) [47,48,53]. Consistent with these reports, we observed a substantial increase in the run frequency of FL kinesin. However, the gains in run frequency and run-length decreased at higher MAP7 concentrations, similar to K560 (Figure 15E). Therefore, MAP7 rescues kinesin from autoinhibited conformation and enhances its motility along MTs at low concentrations, but the effect of MAP7 on FL kinesin is still biphasic.

Next, we tested a kinesin construct (K490, amino acids 1-490) that lacks the MAP7-binding domain and thus is unable to bind MAP7 (Figure 15B) [58]. We hypothesized that K490 could walk on MAP7-coated MTs, but its run frequency would not be enhanced by MAP7. Surprisingly, we observed strong inhibition of K490 motility by MAP7 ($IC_{50}$ = 6.0 ± 1.0 nM, ±s.e., Figure 15F-G), similar to DDR (Figure 14). These results indicate that the activation of kinesin motility is driven by the interaction of kinesin with the projection domain of MAP7. In the absence of this activation, the motor cannot walk due to the inhibitory inputs from MAP7.

**MAP7 switches the directionality of cargos transported by kinesin and dynein**

Given that MAP7 differentially regulates kinesin and dynein motility, we next tested whether MAP7 could control the direction in which kinesin-dynein (KD) assemblies move along MTs [108]. We connected FL kinesin to DDR with a C-terminal GFP on kinesin and a C-terminal anti-GFP nanobody on BicDR1 and labeled the motors with different fluorophores. In the absence of MAP7, DDR walks on the MT but FL kinesin is auto-inhibited (Figure 14J and 2E). As a result, 80 ± 11% of KD assemblies moved towards the MT minus-end and their velocities were similar to that of dynein only (Figure 16B-D). In the presence of 50 nM MAP7, DDR motility is inhibited while FL kinesin is activated (Figure 14J, 2E). In this case, 93 ± 6% of KD assemblies moved towards the plus-end and velocities resembled those of kinesin only (Figure 16B-D, Movie S5). Previous work that linked together dynein and K560 on a DNA scaffold observed substantially impaired velocities, as the two motors engaged in a mechanical tug-of-war [35,36,82]. Here, MAP7 controls the activation state of opposite polarity motors and prevents futile tug-of-war. These results are consistent with a model that MAPs can control the direction of bidirectional transport by activating one class of motor while inhibiting the other.

**MAP7 binds a novel site on the MT**

We next sought to understand why MAPs often inhibit other MAPs and motors to bind the MT. The inhibition of kinesin by tau has been attributed to an overlap between tau and kinesin binding sites [49]. Binding site overlap is also thought to drive MAP7's inhibition of tau binding to the MT [58]. Thus, we first investigated whether the inhibitory interactions we observed on the MT could be explained by a binding site overlap model. As tau and MAP7 both inhibit dynein (Figure 14G-J), the model would predict that both MAPs block dynein's binding site on the MT. Given the striking differences between how MAP7 affects kinesin and dynein motility (Figure

14G-J), the model also predicts a significant difference in how MAP7 overlaps with the binding sites of the two motors.

While tau's structure and binding register along the MT was previously determined [49], MAP7's structure was unknown. Using cryo-EM, we determined the structure of full-length MAP7 bound to the MT at 5.2 Å resolution (Figures 4 and S3). We observe that MAP7 binds at a novel site along the MT outer surface close to key lateral contacts (LCs) between the M-loop (between S7 and H9) in one tubulin monomer and the H2–H3 loop and β-hairpin structure in the H1′–S2 loop of its neighbor (Zhang et al., 2015) (Figure 17B). Consistent with the critical role of inter-PF interactions in the structural organization of MTs [109,110], we observed a drastic shift in PF number of MAP7-bound MTs (Figure 23).

We observe that full-length MAP7 appears to have two binding sites, one at the inter-dimer interface and one at the intra-dimer interface (Figure 17C). The binding site at the intra-dimer interface may be more flexible since the density connecting MAP7 to the MT disappears as the signal-to-noise threshold is increased. The intradimer interface is a major binding site for motors so MAP7 may possess intrinsic flexibility at this site to accommodate motor binding. We also obtained a 4.4 Å co-structure of MAP7's MTBD (aa 60-170) with full-length tau on the MT (Fig. 4D and S3). As hypothesized from previous MAP-MT structures (Figure 17D-F)[49], MAP7 and tau occupied different sites on the MT surface, demonstrating that the inhibition of tau by MAP7 is not driven by steric binding site overlap on the MT surface (Figure 17E).

To determine whether the MAP7's binding site overlaps with motor binding sites, we superimposed previously determined structures of kinesin and dynein bound to the MT onto our MAP7 structure (Figures 4G-H). Both kinesin and dynein bind at the intra-dimer interface between tubulin subunits [111,112]. Surprisingly, there was a clear overlap between the MAP7's density with that of both kinesin and dynein (Figure 17G). Docking of motors on the structure of tau on the MT [49] showed that tau overlaps with the kinesin binding site, but not with the MTBD of dynein (Figure 17G). The "steric overlap model" would thus predict that both motors would be similarly inhibited by MAP7, whereas tau inhibits dynein, but not kinesin. However, these predictions are not in line with our observations (Figure 14I-J). We further challenged the steric overlap model with DCX, as the MT-bound structure of this MAP has recently been characterized at near-atomic resolution[50]. Docking of motors on the structure of the N-terminal doublecortin domain of DCX showed that DCX overlaps with neither kinesin nor DDR (Figure 17G). Yet, the motility assays showed that DCX inhibits both K560 and DDR (Figures 4H-I and S4), providing further evidence against the steric overlap model.

The docking results also raise the question of how kinesin walks on MAP7-coated MTs when MAP7 is blocking its binding site. One possibility is that MAP7 is flexible enough to rearrange itself on the MT and accommodate passing motors, as shown for DCX and kinesin-3 [54], and for

MAP4 and kinesin-1 [98]. To test this possibility, we performed MAP7 pelleting assays with MTs pre-coated with a rigor kinesin monomer ($K350^{E236A}$, amino acids 1-350) in the presence of a nonhydrolyzable ATP analog AMP-PNP. If MAP7's binding site is truly blocked by the kinesin motor domain, MAP7 would not bind $K350^{E236A}$ -coated MTs. In contrast, we see that MAP7 binds the MTs equally well in the presence and absence of $K350^{E236A}$ (Figure 17J-K), suggesting that MAP7 may rearrange on the MT to allow for kinesin to bind and walk along MTs (Figure 17L).

**The MTBDs of MAPs inhibit motors**

Another feature of MAPs that may be inhibitory to motors is their extended projection domain, which may interfere with motors by forming a liquid condensate or by retaining the MAPs on the MT [59,66]. To test if the projection domains interfere with motility, we expressed constructs that included only the MT binding segments of tau and MAP7 (Figure 18A). Unlike FL tau, tau-MTBD (amino acids 242-367) did not bind to MTs in 150 mM salt. In the absence of added salt, tau-MTBD binds to MTs at ~100-fold lower affinity than FL tau and did not form liquid condensates on the MT (Figures 5B-C and S5A). Therefore, the projection domain drives the liquid-liquid phase separation, which is essential for MT binding of tau under physiological conditions. Similar to FL tau, tau-MTBD was inhibitory to both K560 and DDR (Figure 18D-E), suggesting that condensate formation is not necessary for tau to inhibit motors.

Next, we investigated how MAP7-MTBD affects motor motility. Similar to tau-MTBD, both MAP7-N (amino acids 1 -316) and MAP7-MTBD (amino acids 60-170) strongly inhibited both K560 and DDR motility (Figures 5F-G and S5B). We noticed that the degree of inhibition of K560 by MAP7-N ($IC_{50}$ = 17.6 ± 6.0 nM) was comparable to inhibition of K490 by FL MAP7 ($IC_{50}$ = 6 ± 1 nM, Figure 15G). Therefore, MAP7 fully inhibits kinesin motility in the absence of either the MAP7-interacting site of kinesin or the kinesin-binding site of MAP7. Consistent with this conclusion, addition of excess (1 μM) MAP7-N inhibits the motility of kinesin on MTs decorated with 50 nm FL-MAP7, whereas addition of excess MAP7 C-terminal domain (MAP7-C, amino acids 307-749), which lacks the MTBD but still interacts with K560, did not affect motility (Figure 18H-I). As the MTBDs of MAP7 and tau inhibited both motors, we conclude that the projection domains of MAPs are not necessary for motor inhibition.

**Positive charges on MAP MTBDs inhibit motor binding to MTs**

We next investigated how a MAP can inhibit a motor without overlapping with its MT binding site. The MT binding interface of the motors is enriched in positively-charged residues. Previous studies proposed that negatively-charged tails of tubulin (E-hooks) capture motors through electrostatic attraction and retain them on the MT [113]. Electrostatic interactions are also critical for guiding motors to their stable binding sites [12], where they form salt bridges with the negatively-charged residues at the MT surface [114]. Remarkably, MTBD and regions that are proximal to MTBD of both MAP7 and tau are highly enriched in arginine and lysine residues

(Figure 19A), which may compete for negatively-charged residues on MTs and prevent motor binding. We showed that a scrambled sequence of the R2 pseudo-repeat in tau and a synthetic peptide consisting of lysine, arginine, glycine, and serine residues strongly bind to the MT (Figure 25C), demonstrating the relevance of the positively-charged amino acid composition of MAP MTBDs.

To investigate whether tau inhibits motors by competing for the E-hooks, we cleaved the tubulin C-terminal tail by subtilisin treatment (Figure 26A). Both K560 and DDR walked processively on subtilisin-treated MTs, and the addition of 100 nM tau abolished their motility (Figure 26B). Because tau inhibits motors both in the presence or absence of the tubulin C-terminal tails (Figure 14H), tau MTBD prevents binding of dynein to the MT surface, rather than preventing its MT recruitment through the E-hooks. We also tested whether positively charged residues of tau change the electrostatic potential at the MT surface (Figure 19B) and inhibit the guiding of motors to a closely-positioned site. Consistent with this prediction, K560 motility was fully inhibited by 5 nM of poly-L-lysine (PLL, Figure 19C).

## Discussion

*In vitro* reconstitution of kinesin and dynein motility on purified MTs has contributed to our understanding of how these motors transport cargos along MTs in cells. However, how motors walk on MTs decorated with different types of MAPs is not well understood. In this study, we investigated the mechanism by which the activity of kinesin-1 and cytoplasmic dynein is regulated by MAP7, tau, and DCX. In contrast to previous reports, we observed that dynein motility is strongly inhibited by these MAPs regardless of overlap between the MT binding sites of dynein and these MAPs. Kinesin was also inhibited by MTBDs of these MAPs. However, the interaction between kinesin and the projection domain of MAP7 activates kinesin and allows this motor to walk on MAP7-coated MTs despite a steric overlap between their MT binding sites. Using a combination of cryo-EM imaging and MD simulations, we dissected the mechanism by which MT binding of MAPs inhibits motility. Our results challenge the established views of motor regulation by MAPs and we propose a new model for how kinesin- and dynein-driven transport are regulated by MAPs.

### Motors must interact with a MAP to walk on a MAP-coated MT.

Previous studies showed that MAPs are largely inhibitory to kinesin motors *in vitro* [39], with the exceptions of kinesin-1 with MAP7 and kinesin-3 with DCX. In these motor/MAP pairs, the motor binds to the MAP through weak interactions ($K_D$ >10 μM)[53]. In this study, we observed that motors were inhibited by MAPs that they do not interact with. MAP7 regulated kinesin motility in a biphasic manner, meaning that it can both activate and inhibit kinesin motility. At low concentrations, MAP7 serves as an allosteric activator and tethers kinesin to MT [53]. At higher concentrations, MAP7 becomes inhibitory to kinesin motility through the actions of

MAP7's MTBD (Figure 20A). We propose that favorable interactions with the projection domain of MAP7 help overcome the inhibitory interactions with the MTBD of MAP7. These results indicate that MAPs are broadly inhibitory to motors unless the motor can make a specific interaction with that MAP. Consistent with this model, MAP7 becomes fully inhibitory to kinesin without a favorable interaction between kinesin and MAP7 IDR. Similarly, due to the absence of a known favorable interaction, MAP7 inhibits dynein motility by preventing its binding to MTs. This model provides a broad framework for how MAPs specifically regulate motor proteins.

**Biphasic regulation of kinesin.**

Because MAP7 activates kinesin at low concentrations and inhibits motility at higher concentrations, MAP7 results in biphasic regulation of kinesin motility. Based on our observations and previous reports, we propose a possible mechanism for this regulation. Kinesin is recruited to MAP7-coated MTs through the interaction of its stalk with the MAP7 projection domain [58]. This rescues kinesin from the autoinhibited conformation and initiates processive motility along the MT [53]. Due to the weak affinity of kinesin to MAP7, the motor disrupts its interaction with one MAP while forming a favorable interaction with another MAP as it walks through the dense "brush" of MAP projections on the MT surface. These interactions prevent the motor from diffusing away after it dissociates from the MT. As a result, the motor quickly rebinds and continues to walk from the same location on the MT lattice, increasing the apparent run length of a motor. When the MT surface is nearly saturated with MAP7, run frequency and run length of kinesin are reduced because the inhibitory effect of MAP7's MTBD begins to be more dominant than the activation from the projection domain. Kinesin and MAP7 have overlapping binding sites on the MT, kinesin may have to wait for MAP7 to detach before taking a step on the MT. It is also possible that MAP7 rearranges on the MT surface to allow for motor binding, as seen with DCX and MAP4 [54,98]. Together, activation of motility by MAP7's projection domain and inhibition by MAP7's MTBD combine to yield a biphasic effect on kinesin motility. Consistent with this model, MAP7 fully inhibits kinesin in the absence of a favorable interaction between kinesin and MAP7 projection domain.

**Inhibition of motors by MAPs**

Inhibitory role of MAP7 and tau on kinesin and dynein motility primarily arose from their MTBDs. This was unexpected because the two MAPs bind in different locations on the MT surface (Figure 17). MAP7-MTBD overlaps with kinesin and dynein binding sites, and it prevents these motors to bind MTs. However, tau-MTBD inhibits dynein motility without a steric clash with dynein's MTBD or by forming liquid condensates on the MT, suggesting that direct overlap or phase separation are not necessary for motor inhibition (Figure 20B). Phase separation of tau on the MT likely contributes to inhibition by stabilizing the binding of tau on the MT surface. We also observed that both kinesin and dynein were inhibited by DCX, which

has no overlap with the MTBDs of motors [50]. Together, our data suggest that the effect of a MAP on a motor cannot be predicted based on the presence or absence of a binding site overlap.

We provided evidence that MAPs can prevent motors from binding the MT by altering the electrostatic potential of the MT surface (Figure 19). The MT surface is strongly negatively-charged, which favors the binding of positively-charged motor domains of kinesin and dynein [12]. The MTBDs of MAPs are also positively charged and MT binding of these MAPs can compete against the motor for interacting with the negative charges on the MT surface. Stable binding of a motor may be disrupted by pockets of positive charges introduced by the MTBD of these MAPs either at or near the motor binding site. These unfavorable interactions can inhibit the recruitment of motors and accelerate their dissociation as they step along the MT. Consistent with this model, positively-charged polypeptides can bind the MT surface and interfere with motor transport [115,116]. In addition to the MAP/tubulin interface, tubulin C-terminal tails are negatively charged, whereas proximal regions of MAP MTBDs are positively charged, suggesting that these regions likely also play a role in how MAPs and motors interact. Future work will be required to dissect the role of tubulin tails in MAP/motor interactions.

**Differential regulation of motor activity by MAPs**

In cells, the destination of specific cargos may be encoded by modifications of the MT tracks. Although post-translational modifications of tubulin have been proposed to play a major role in this process, *in vitro* studies report relatively minor effects in motor activity by detyrosination and acetylation of tubulin [117]. In comparison, MAPs have a strong effect on motor activity, suggesting that the "MAP code" on MT tracks regulates motor activity. In neurons, MAPs segregate into distinct spatial domains [11,39]. Tau is concentrated in the axon, while MAP2 is found in the cell body and dendrites. DCX and DCLK1 are enriched at the ends of the dendritic and axonal extensions. MAP7 and MAP9, on the other hand, are found throughout the neuron. The spatial patterns of MAP localizations may play a major role in sorting cargos transported by specific motors. This view has been supported by the observations that MAPs that localize to dendrites favor kinesin-3 motility on MTs in vitro and loss of these MAPs impede kinesin-3 driven transport in dendrites [54]. Similarly, the loss of MAP7 prevents kinesin-1 recruitment to MTs in human cells [53]. Consistent with the MAP code model, the addition of MAP7 causes a shift in the direction of isolated phagosomes on MTs in vitro, which has been attributed to an increase in the MT-binding rate of kinesin-1 [108]. Similarly, we observed that the addition of MAP7 almost fully switches the direction of kinesin and dynein assembled on a cargo adaptor from the minus-end to the plus-end, favoring kinesin-driven transport. However, this major shift in direction of motility is due to reciprocal activation and inactivation of kinesin and dynein by MAP7, rather than accelerated rebinding of kinesin-1 to MTs.

While in vitro studies identified MAP7 and MAP9 as favorite MAPs of kinesin-1 and kinesin-3, respectively, positive interactions between dynein and a specific MAP has not been determined,

and its motility is inhibited by all three MAPs we tested. The dynein complex may possess a different mechanism to walk on MAP-coated MTs. For example, dynein is recruited to specific cargos by coiled-coil adaptor proteins. Some of these adaptors, such as JIP1, contain an SH3 domain that is known to interact with proline-rich regions [118]. Tau, MAP7, DCX, and other MAPs have proline-rich regions projecting from the MTBD [50,53,54,119], raising the possibility that regulation of the retrograde transport by MAPs is driven by cargo adaptor proteins, rather than dynein itself. Future studies are required to test whether this model can be generalized for the regulation of other cargo adaptors with specific MAPs.

## Figures

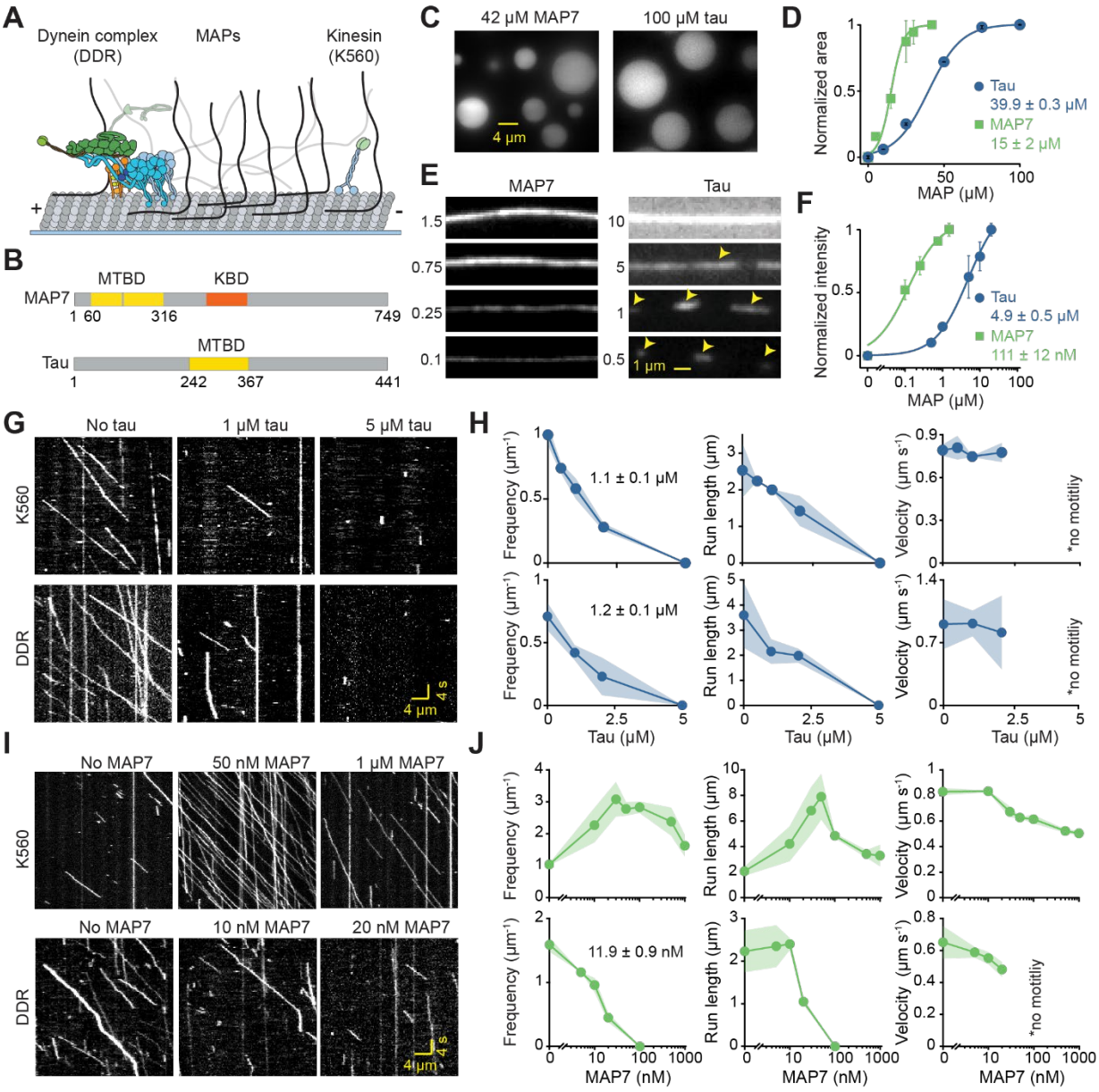


**Figure 14. MAP7 and tau differentially regulate kinesin and dynein motility. (A)** Schematic of kinesin and dynein motility on MTs coated with MAPs. DDR assembled with mammalian dynein, dynactin, and BicDR1. Human kinesin-1 was truncated at its tail (K560). **(B)** Schematic of MAP7 and tau functional domains. **(C)** Fluorescent images show MAP7 and tau form liquid condensates in the absence of MTs. **(D)** Area covered by condensates increases with MAP7 and tau concentration (mean ± s.d., n = 10 images each condition, two technical replicates). The MAP concentration that produces half-maximal surface area coverage (cSat, ±s.e.) was determined from a fit to the Hill equation (solid curves). **(E)** Images of fluorescently -labeled

MAP7 and tau on single MTs. Higher concentrations (μM) were used for tau to account for its lower MT affinity. Yellow arrows point to tau islands at low concentrations. **(F)** Normalized intensity of MAP7 and tau binding to the MT (mean ± s.d.). $K_D$ values (±s.e.) were calculated from a fit to the Hill equation (solid curves). From left to right, N = 54, 63, 58, 49, 73 for tau, and 44, 50, 68, 109 MTs for MAP7 (two technical replicates). **(G)** Representative kymographs of K560 and DDR motility in the absence and presence of tau. **(H)** Run frequency, run length, and velocity of K560 and DDR at different tau concentrations (mean ± s.d.). $IC_{50}$ values were calculated from a fit with a single exponential decay function (± s.e.). From left to right, N = 198, 160, 209, 99 for K560, and 185, 129, 100 for DDR (two technical replicates). **(G)** Representative kymographs of K560 and DDR motility in the absence and presence of MAP7. **(H)** Run frequency, run length, and velocity of K560 and DDR at different MAP7 concentrations (mean ± s.d.). cSat was calculated from a single exponential decay (± s.e.). From left to right, N = 281, 463, 532, 836, 381, 433, 233 for K560, and 386, 235, 213, 146 for DDR (two technical replicates). In E-J, the assays performed in 150 mM KAc and 0.1% methylcellulose.

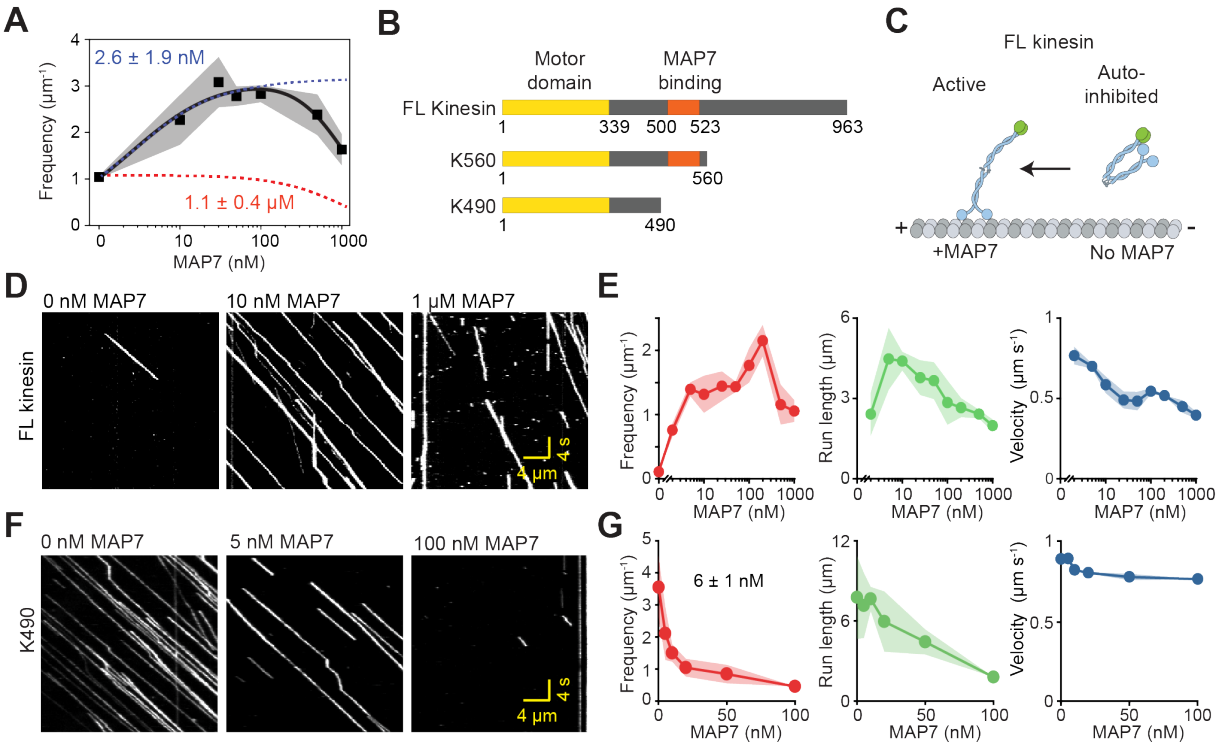


**Figure 15. Interaction with MAP7's projection domain drives kinesin activation. (A)** The biphasic regulation of K560 run frequency with MAP7 can be modeled by a fit to a Hill equation (solid black curve), which has an inhibition component (dashed red curve) and an activation component (dashed blue curve). The fit reveals the half-maximal activation and inhibition concentrations (±s.e.). **(B)** Schematic of FL and tail-truncated kinesin constructs. K490 does not contain the MAP7 binding domain. **(C)** Schematic depicting the activation of kinesin by MAP7. **(D)** Kymographs of FL kinesin motility in the absence and presence of MAP7. **(E)** Run frequency, run length, and velocity of FL kinesin with different MAP7 concentrations. N = 12, 658, 399, 527, 816, 664, 2434, 1303, 897, 802 runs from left to right (two technical replicates). **(F)** Kymographs of K490 motility in the absence and presence of MAP7. **(G)** Run frequency, run length, and velocity of K490 with different MAP7 concentrations. N = 855, 532, 581, 304, 457, 149 traces from left to right (two technical replicates). Assays were performed in 150 mM KAc and 0.1% methylcellulose. Error bars represent s.d.

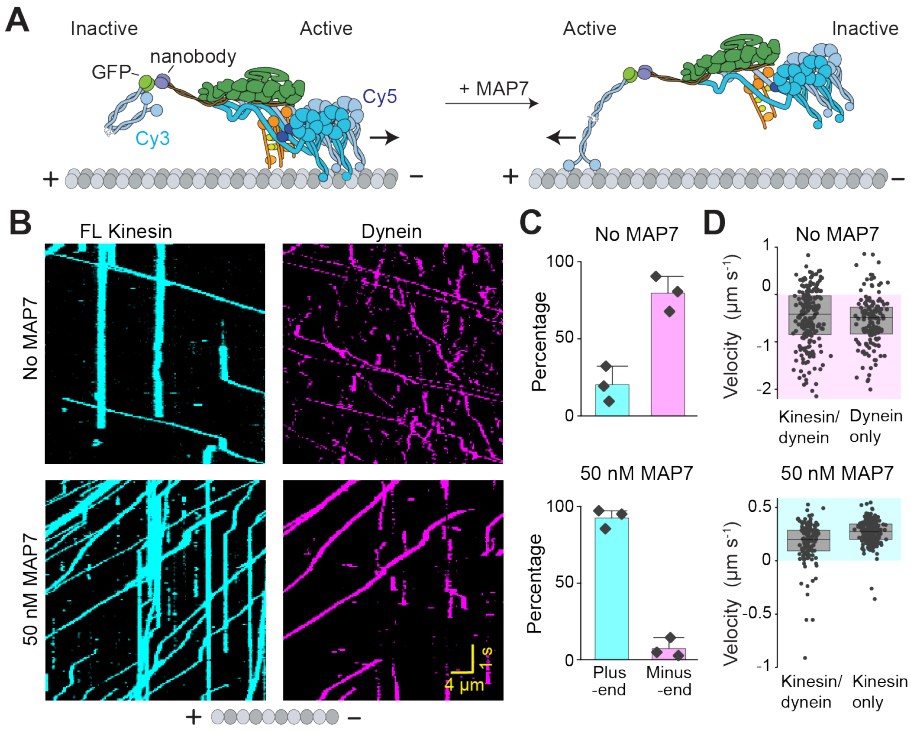


**Figure 16. MAP7 switches the direction of kinesin-dynein assemblies on an MT. (A)** Schematic of a model cargo assembled onto BicDR1. FL kinesin is attached to BicDR1 through a GFP-nanobody linkage. Dynein and FL kinesin are labeled with Cy5 and Cy3, respectively. In the absence of MAP7 (left), FL kinesin is inactive, whereas DDR is active. The addition of MAP7 switches the active motor (right). **(B)** Kymographs of kinesin-dynein assemblies in the absence and presence of 50 nM MAP7. **(C)** The direction of complexes that contain both kinesin and dynein in the absence and presence of 50 nM MAP7. **(D)** (Top) The velocity of complexes that contain both kinesin and dynein versus dynein only in the absence of MAP7. N = 207, 151 from left to right. (Bottom) The velocity of complexes that contain both kinesin and dynein versus dynein only in 50 nM MAP7. N = 145, 435 from left to right. Experiments were repeated 3 times without additional KAc or methylcellulose.

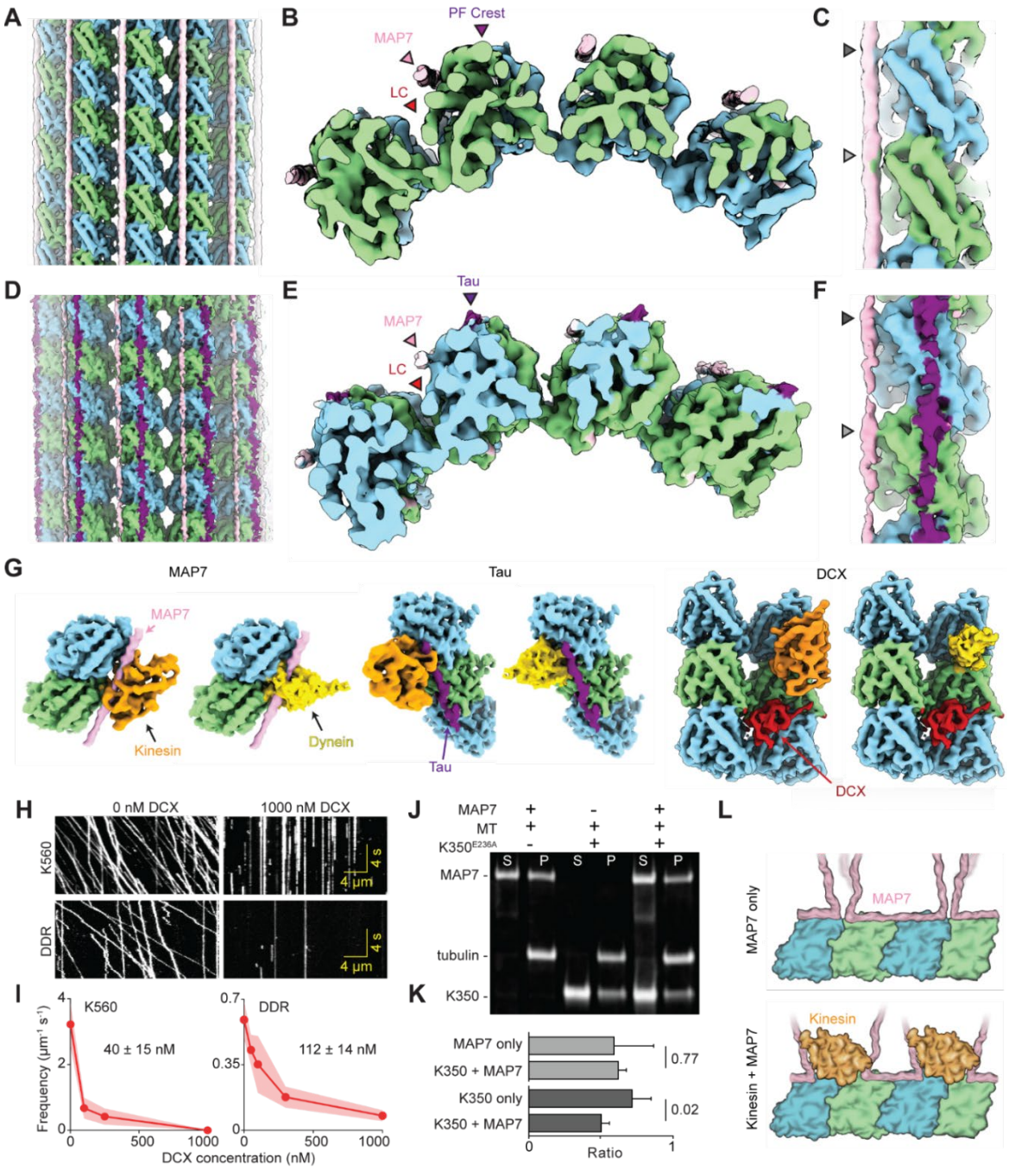


**Figure 17. Visualization of MAP7 bound to an MT and considerations on simultaneous motor binding. (A)** Cryo-EM map of an MT decorated with MAP7; α-tubulin, β-tubulin, and MAP7 are shown in green, blue, and pink, respectively. MAP7 binds on the outer surface of the MT close to the lateral contacts (LCs) between protofilaments (PFs). The map is shown at a threshold of 1.7 in ChimeraX. **(B**) An end-on view of MAP7 in between four PFs. MAP7 is closer to an LC than the central region of a PF, or the PF crest. **(C)** Close-up of the structure highlighting the potential binding sites of MAP7 with α - and β -tubulin (orange arrows). **(D)**

Cryo-EM map of an MT co-decorated with MAP7-MTBD and tau at a threshold of 2. **(E)** End-on view of MAP7-MTBD and full-length tau in between four PFs. **(F)** Close-up of the MAP7-MTBD and tau co-decorated MT. **(G)** The density for MAP7, tau (EMDB ID: 7769), and DCX (EMDB ID: 1788) superimposed with the kinesin motor domain (EMDB ID: 6353) and dynein MTBD (EMDB ID: 10060). **(H)** Kymographs of K560 and DDR motility in the absence and presence of DCX. **(I)** The run frequency of K560 and DDR in different DCX concentrations. From left to right, N = 655, 187, 130, 0 runs for K560 and 224, 237, 245, 104, 55 runs for DDR. $IC_{50}$ (±s.e.) of run frequency was calculated from a fit to a single exponential decay. **(J)** The denatured gel of MT pelleting assay tests MAP7 binding to MTs pre-decorated with $K350^{E236A}$ in 150 mM KAc (S: supernatant, P: pellet). **(K)** Ratios of band intensities of (top) MAP7 to tubulin and (bottom) kinesin to tubulin in the pellet in J. Error bars represent s.d. between 3 technical replicates. p-value was derived from a two-tailed t-test. **(L)** A model for flexible rearrangement of MAP7 to accommodate kinesin on an MT.

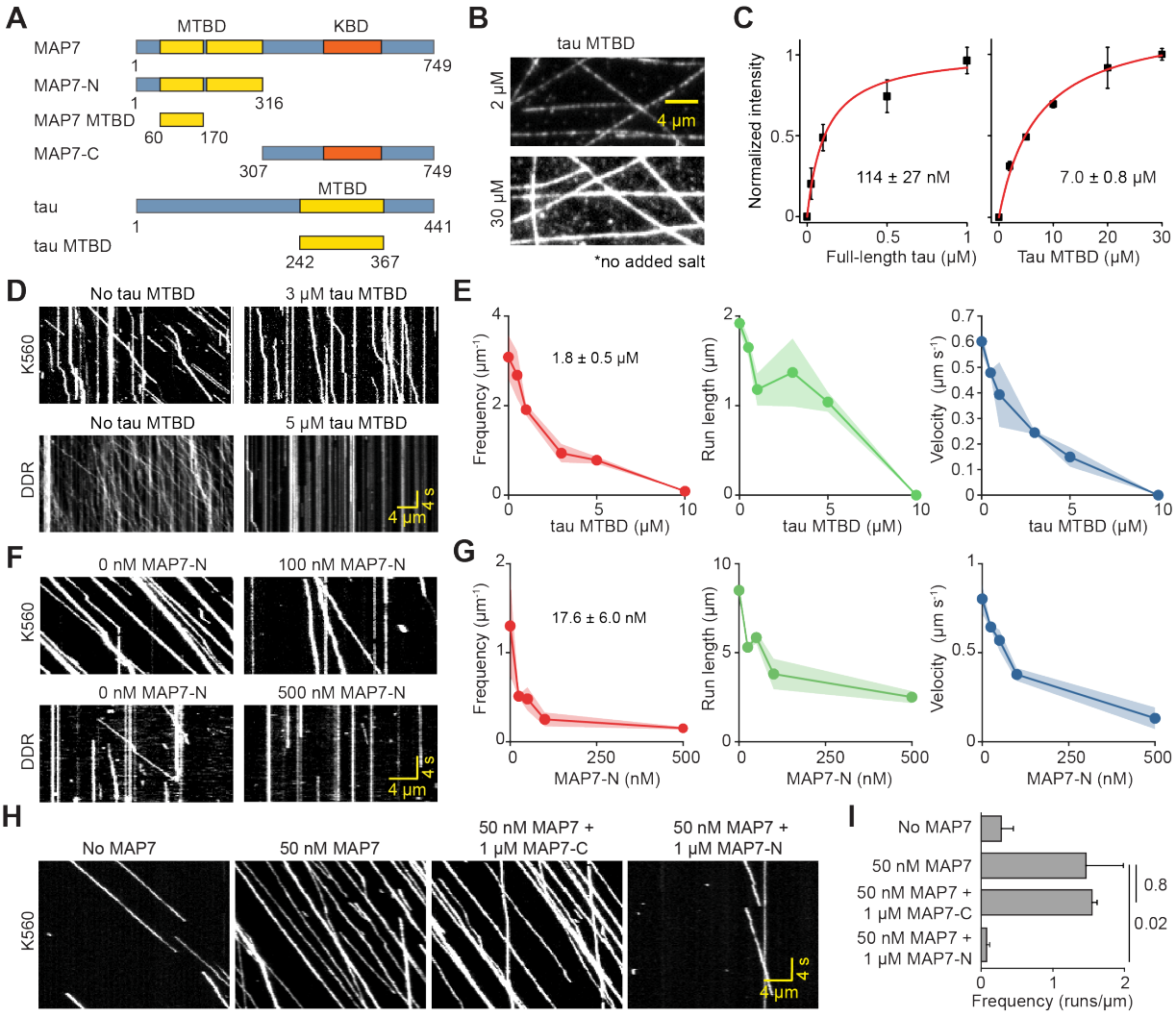


**Figure 18. MTBDs of MAPs are inhibitory to motors. (A)** Schematic of MAP7 and tau truncation constructs. **(B)** Fluorescence images show that tau MTBD does not form liquid condensates on MTs. **(C)** The MT-binding affinity of FL tau and tau MTBD in the absence of added salt and methylcellulose (N = 20 each condition, two technical replicates). Dissociation constants (±s.e.) were calculated from a fit to Hill Equation (red curves). **(D)** Kymographs of K560 and DDR motility in the absence and presence of MTBD tau, without added salt or methylcellulose. **(E)** The run frequency, run length, and velocity of K560 in different tau MTBD concentrations. N = 848, 801, 839, 568, 499, 46 from left to right. $IC_{50}$ (±s.e.) of run frequency was calculated from a fit to a single exponential decay. **(F)** Kymographs of K560 and DDR motility in the absence and presence of MAP7-N. Assays were performed in 150 mM KAc and 0.1% methylcellulose. **(G)** The run frequency, run length, and velocity of K560 in different MAP7-N concentrations. N = 276, 168, 172, 121, 75 from left to right. $IC_{50}$ (±s.e.) of run frequency was calculated from a fit to a single exponential decay. **(H)** Kymographs of K560 motility in the presence of MAP7 construct combinations. **(I)** K560 run frequency for different

MAP7 construct combinations. From top to bottom, N = 114, 355, 365, 27 runs. Error bars represent s.d. p-values are calculated from a two-tailed t-test.

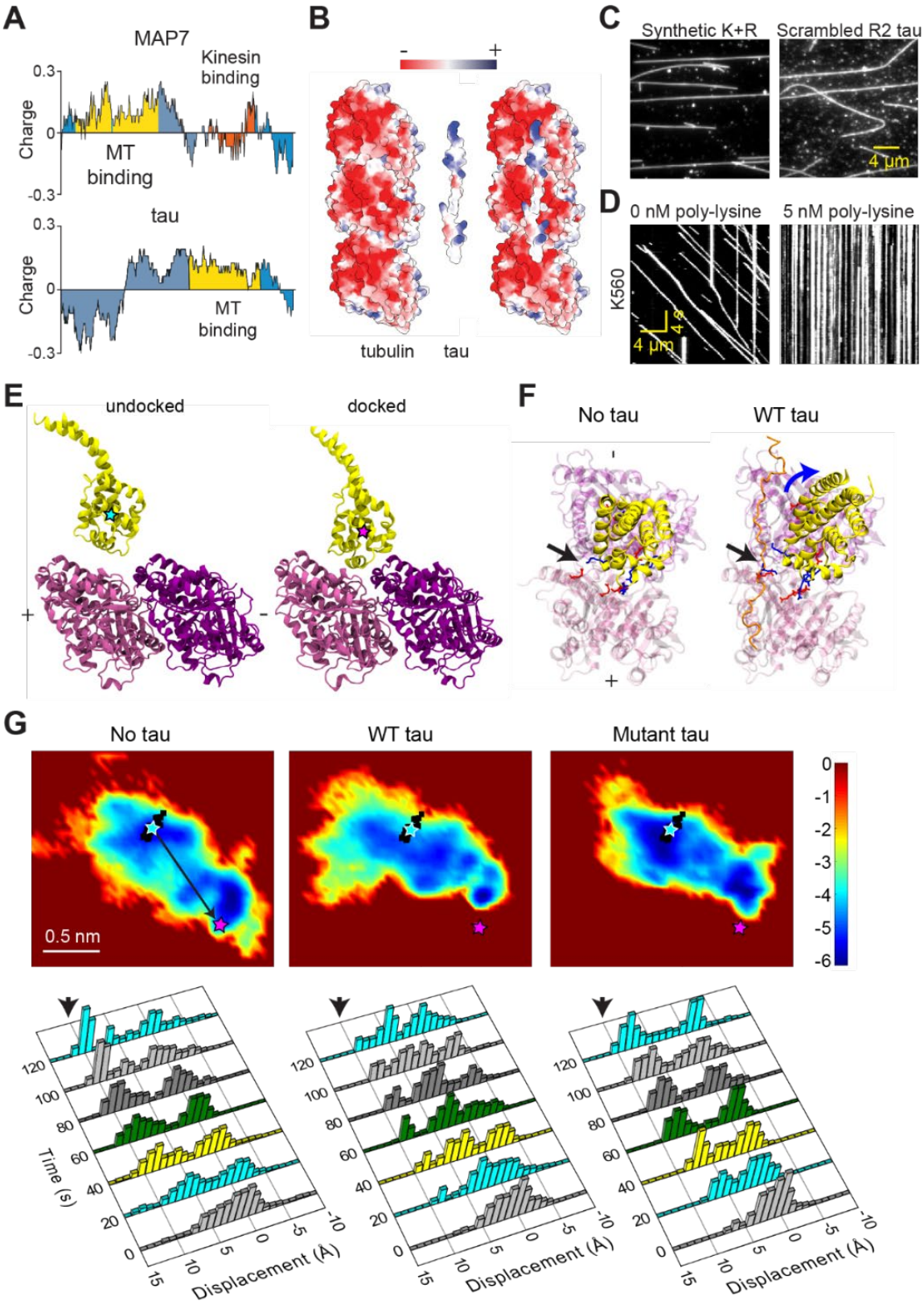
A
MAP7
Kinesin binding
MT binding
Charge
0.3
0
-0.3
tau
MT binding
B
-
+
tubulin
tau
C
Synthetic K+R
Scrambled R2 tau
4 µm
D
0 nM poly-lysine
5 nM poly-lysine
K560
4 µm
4 s
E
undocked
docked
+
-
F
No tau
WT tau
+
G
No tau
WT tau
Mutant tau
0.5 nm
0
-1
-2
-3
-4
-5
-6
Time (s)
120
100
80
60
40
20
0
15
10
5
0
-5
-10
Displacement (Å)

**Figure 19. Positive charges on the MT-binding domain inhibit motors. (A)** Charge distribution on MAP7 and tau using a sliding window size of 30 amino acids. **(B)** Electrostatic potential map of MT, tau, and MT/tau complex. **(C)** Fluorescent images of synthetic peptides bound on the MT. "Synthetic K+R" is a scrambled sequence of 30 arginine (R), 30 lysine (K), 20 glycine (G), 20 serine (S) residues. "Scrambled R2 tau" is a scrambled sequence of the R2 repeat region in the MTBD of tau. **(D)** Kymograph of kinesin motility in the absence and presence of poly-lysine. The experiment was repeated 3 times. **(E)** MD simulations of dynein MTBD to a tubulin heterodimer. Dynein MTBD in the low-affinity state was positioned 1 nm away from the stable binding position. Pink and magenta stars show the midpoint of helices XXX of dynein MTBD at the starting point of the simulations and in the docking position of dynein on the MTBD, respectively. The C-terminal tubulin tails have not been modeled. **(F)** The top view shows the formation of salt bridges between the positive charges on dynein (blue) and negative residues on tubulin. In the presence of tau (right), the salt bridge between dynein XXX and tubulin YYY cannot form due to tau ZZZ (black arrow), and the dynein MTBD rotates away from the tau binding site (blue arrow)). **(G)** (Top) The heat maps show the position of the midpoint of helices XXX of dynein MTBD relative to the starting point of the simulations (black squares) and in the docking position of dynein on the MTBD (pink star). The pink line is drawn from the average position of black squares to the pink star. (Bottom) The histogram shows the displacement of the midpoint along the pink line in F. 0 and 10 Å distances correspond to the starting position of the simulations and the stable docking of dynein to the MT, respectively.

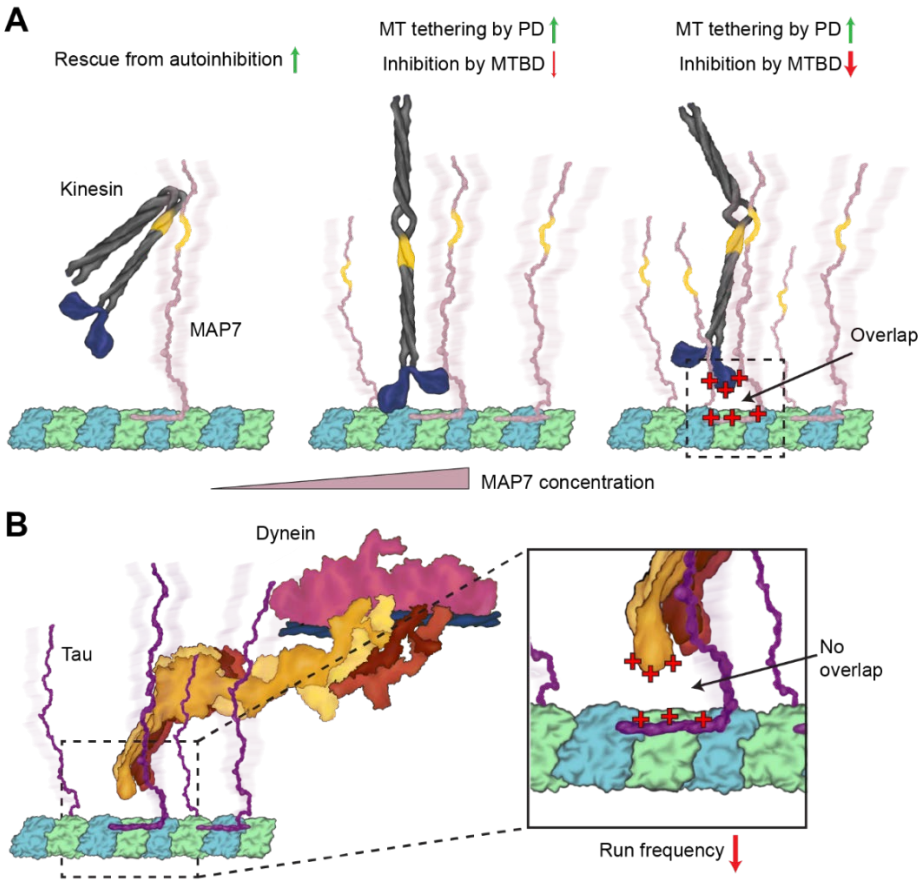


**Figure 20. Model for regulation of MT motors by MAPs. (A)** (Left) Kinesin is auto-inhibited in solution. Binding of kinesin to MAP7's projection domain relieves the motor from auto-inhibited conformation. (Middle) Interaction between kinesin's stalk and MAP7 projection domain (PD) serves as a tether that prevents the dissociation of kinesin from MT. Kinesin walks along MAP7-coated MT even though it competes for the same binding site with MAP7 MTBD. (Right) As the MT surface is nearly saturated with MAP7, MTBD inhibits kinesin motility either through steric overlap or electrostatic repulsion between the positive charges. **(B)** Unlike the kinesin-MAP7 pair, dynein does not specifically interact with tau's projection domain. In this case, positive charges on tau and dynein MTBD repel each other and compete for the negatively charged residues on the MT. As a rest, tau inhibits dynein motility without overlapping between their MT binding sites.

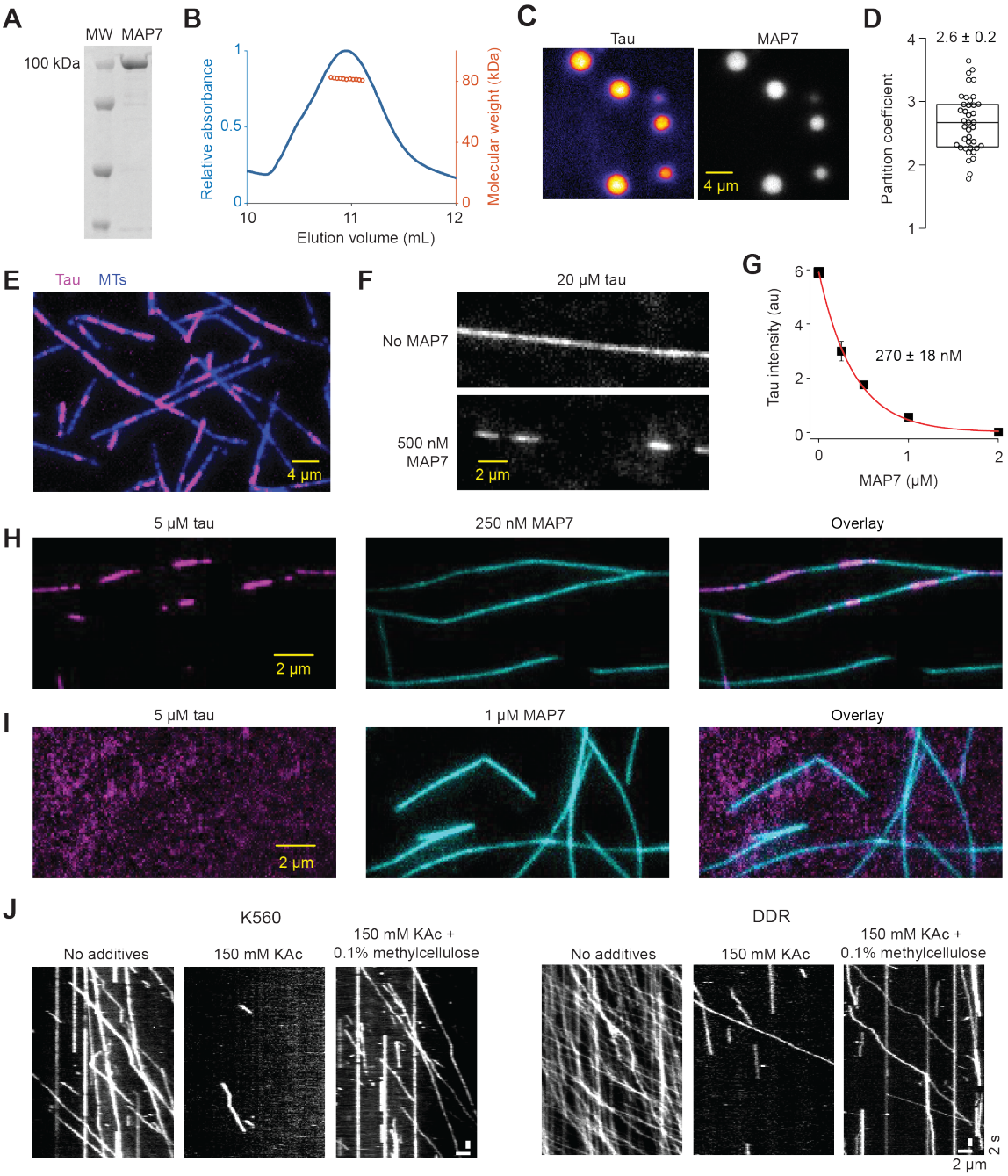


**Figure 21. Interactions between MAP7 and tau in solution and on MTs; related to Figure 14. (A)** Denaturing gel of purified MAP7 (MW: molecular weight). **(B)** Size exclusion chromatography coupled to multi-angle light scattering of MAP7 (SEC-MALS) shows MAP7 elutes as a monomer. **(C)** Partitioning of tau into MAP7 droplets formed in solution. Droplets are formed in the presence of 150 mM KAc without a crowding agent. In the tau channel, fluorescence intensity increases from blue to red. **(D)** The partition coefficient of tau into MAP7 droplets (N = 40, mean ± s.d.). The center line and edges of the box represent mean and quartiles. **(E)** Fluorescent image shows tau condensates on the MT. **(F)** MT decoration of 20 µM

tau in the presence and absence of 500 nM MAP7. **(G)** MAP7 removes tau from MTs. Fluorescence intensity of 20 μM tau on MTs was measured at different MAP7 concentrations (symbols, mean ± s.d.). $IC_{50}$ (mean ± s.d.) was determined from a fit to a single exponential decay (red curve). **(H)** Two-color fluorescent images of 5 μM tau and 250 nM MAP7 show an overlap between MAP7 and tau islands on the MT. **(I)** 1 μM MAP7 displaces 5 μM tau on the MT. **(J)** K560 and DDR motility in the presence and absence of 150 mM KAc and 0.1% methylcellulose.

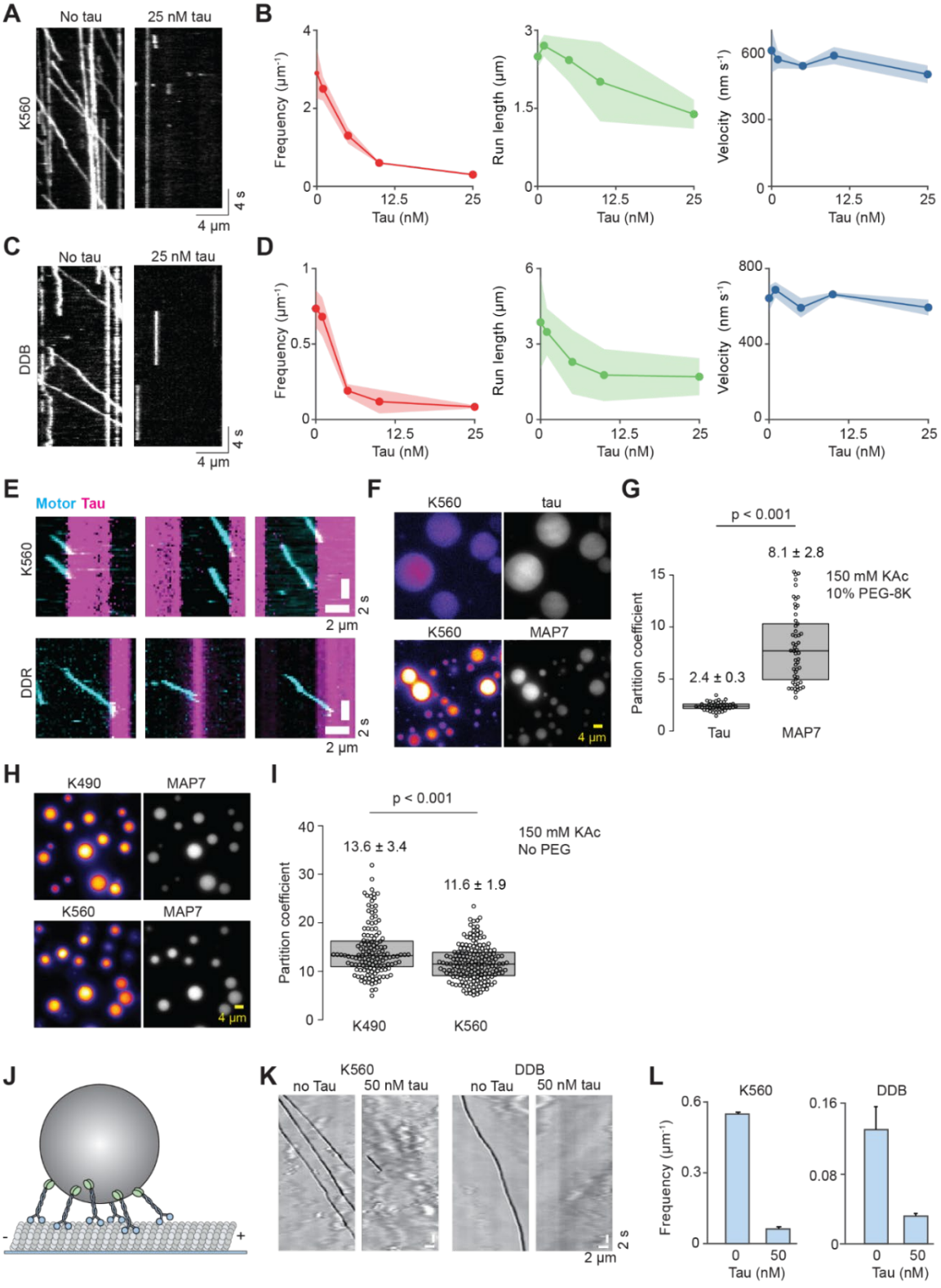
A
No tau
25 nM tau
K560
4 s
4 µm
B
Frequency (µm⁻¹)
Run length (µm)
Velocity (nm s⁻¹)
Tau (nM)
C
DDB
D
E
Motor Tau
K560
DDR
2 s
2 µm
F
K560
tau
MAP7
4 µm
G
p < 0.001
8.1 ± 2.8
150 mM KAc
10% PEG-8K
2.4 ± 0.3
Partition coefficient
Tau
MAP7
H
K490
I
13.6 ± 3.4
11.6 ± 1.9
No PEG
J
K
no Tau
50 nM tau
L

**Figure 22. Regulation of single and a team of kinesin and dynein motors by tau and MAP7; related to Figure 14. (A)** Kymographs of K560 motility with and without tau in the absence of added salt or methylcellulose. **(B)** The run frequency, run length, and velocity of K560 at different tau concentrations. N = 432, 270, 229, 193, 133 runs from left to right. **(C)** Kymographs of the dynein-dynactin-BicD2N (DDB) complex with and without tau in the absence of added salt or methylcellulose. **(D)** The run frequency, run length, and velocity of DDB at different tau concentrations. N = 210, 162, 89, 71, 50 runs from left to right. **(E)** Example kymographs show both K560 and DDR motility stops when the motors encounter a tau condensate on an MT in 150 mM KAc. **(F)** In the absence of MTs, K560-GFP partitions into tau and MAP7 droplets in solution. Droplets are formed in 150 mM KAc and 10% PEG-8000. **(G)** K560 partitions more strongly into MAP7 droplets than tau droplets. The center line and edges of the box represent mean and quartiles. Mean value plus standard deviation given above plot. p-value was calculated from two-tailed t-test. N = 44, 54 for tau and MAP7 droplets, respectively (mean ± s.d., three technical replicates). **(H)** K490 and K560 partition into MAP7 droplets. Droplets are formed in the presence of 150 mM KAc (no PEG). False colors in the kinesin channel represent the fluorescence signal to increase from blue to yellow. **(I)** Partition coefficients of K490 and K560 into MAP7 droplets. N = 138, 176 droplets for K490 and K560, respectively (mean ± s.d., three technical replicates). The center line and edges of the box represent mean and quartiles. p-value was derived from a two-tailed t-test. **(J)** Schematic shows a bead driven by multiple kinesin motors. **(K)** Kymographs of beads driven by multiple K560s or DDBs in the presence or absence of 50 nM tau in the absence of added salt or methylcellulose. **(L)** The run frequency for multi-motor driven beads decreases by tau. From left to right, N = 210, 41, 109, and 28 runs. All error bars represent s.d.

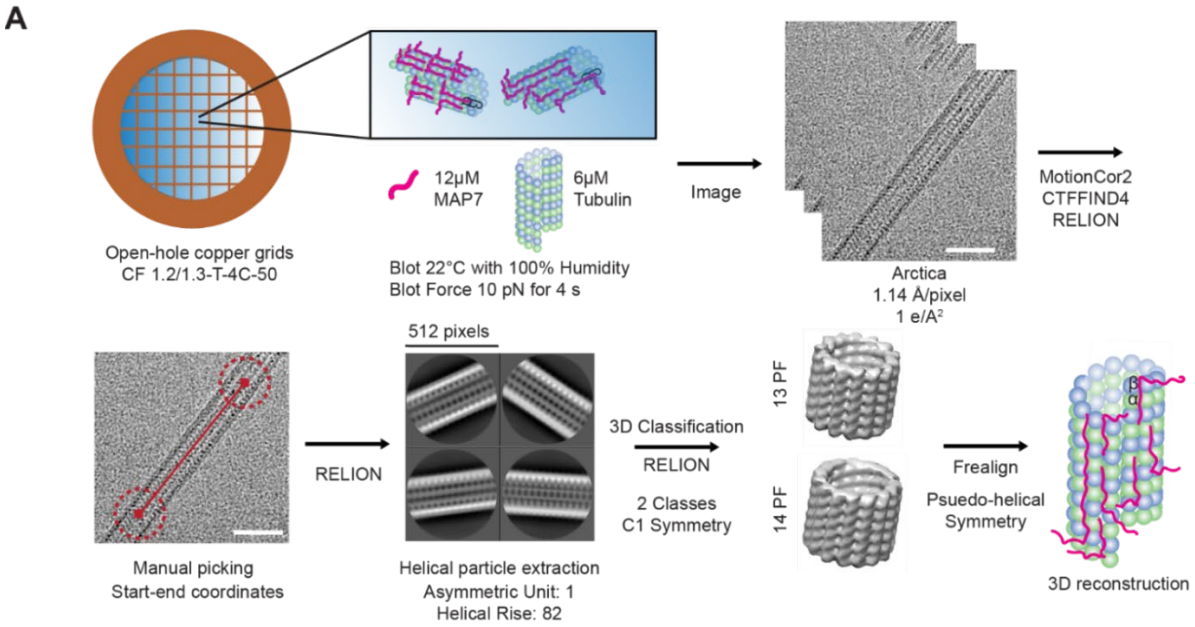
A
Open-hole copper grids
CF 1.2/1.3-T-4C-50
12μM
MAP7
6μM
Tubulin
Blot 22°C with 100% Humidity
Blot Force 10 pN for 4 s
Image
Arctica
1.14 Å/pixel
1 e/A²
MotionCor2
CTFFIND4
RELION
Manual picking
Start-end coordinates
RELION
512 pixels
Helical particle extraction
Asymmetric Unit: 1
Helical Rise: 82
3D Classification
RELION
2 Classes
C1 Symmetry
13 PF
14 PF
Frealign
Psuedo-helical
Symmetry
3D reconstruction

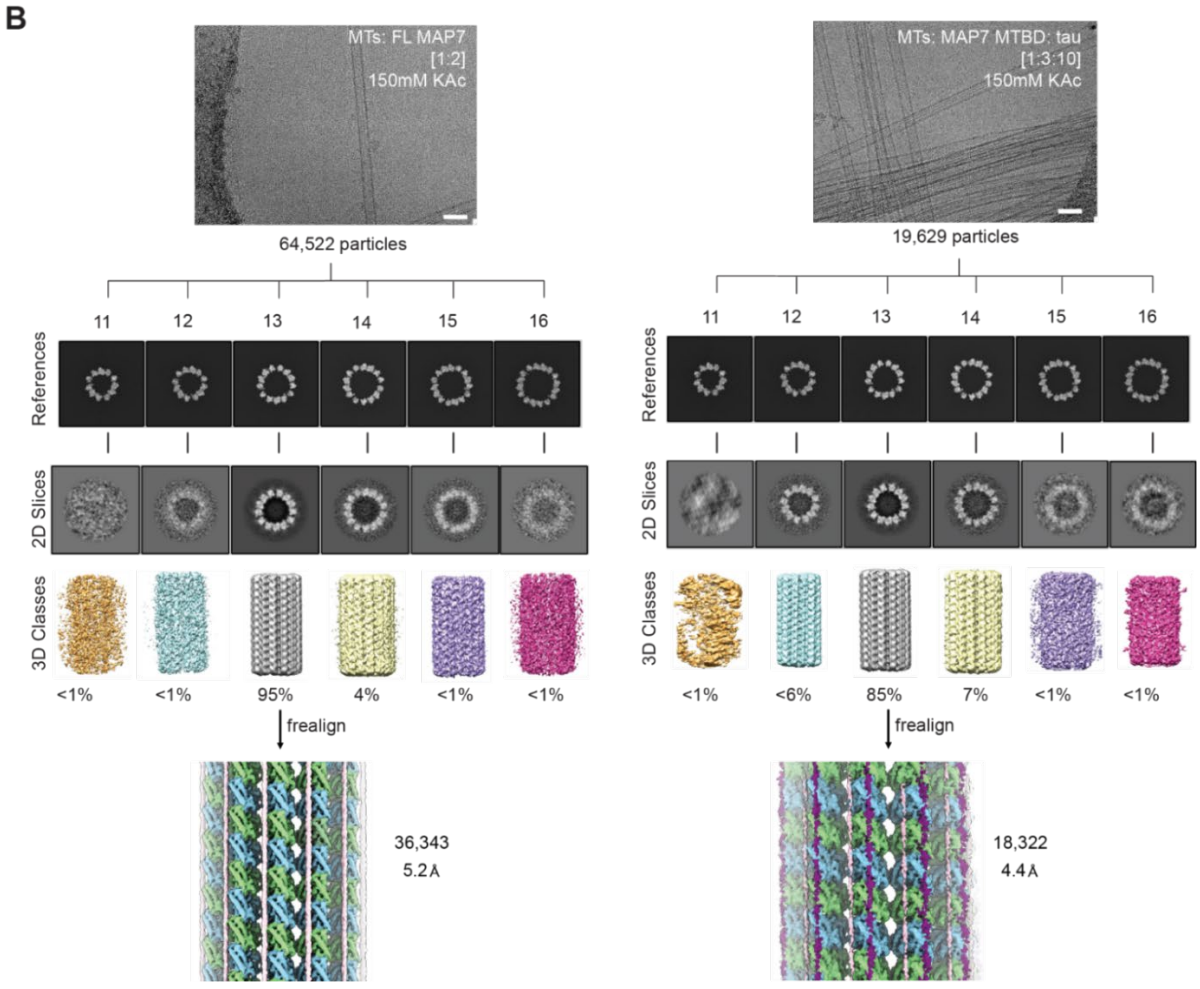
B
MTs: FL MAP7
[1:2]
150mM KAc
64,522 particles
MTs: MAP7 MTBD: tau
[1:3:10]
150mM KAc
19,629 particles
11
12
13
14
15
16
References
2D Slices
3D Classes
<1%
<1%
95%
4%
<1%
<1%
<1%
<6%
85%
7%
<1%
<1%
frealign
frealign
36,343
5.2Å
18,322
4.4Å

**Figure 23. Cryo-EM image processing pipeline; related to Figure 17. (A)** cryo-EM sample preparation and image processing pipeline. **(B)** Representative micrographs for MTs decorated with FL MAP7 (left) and with MAP7 MTBD and tau (right). For both constructs MTs have predominately 13 protofilaments.

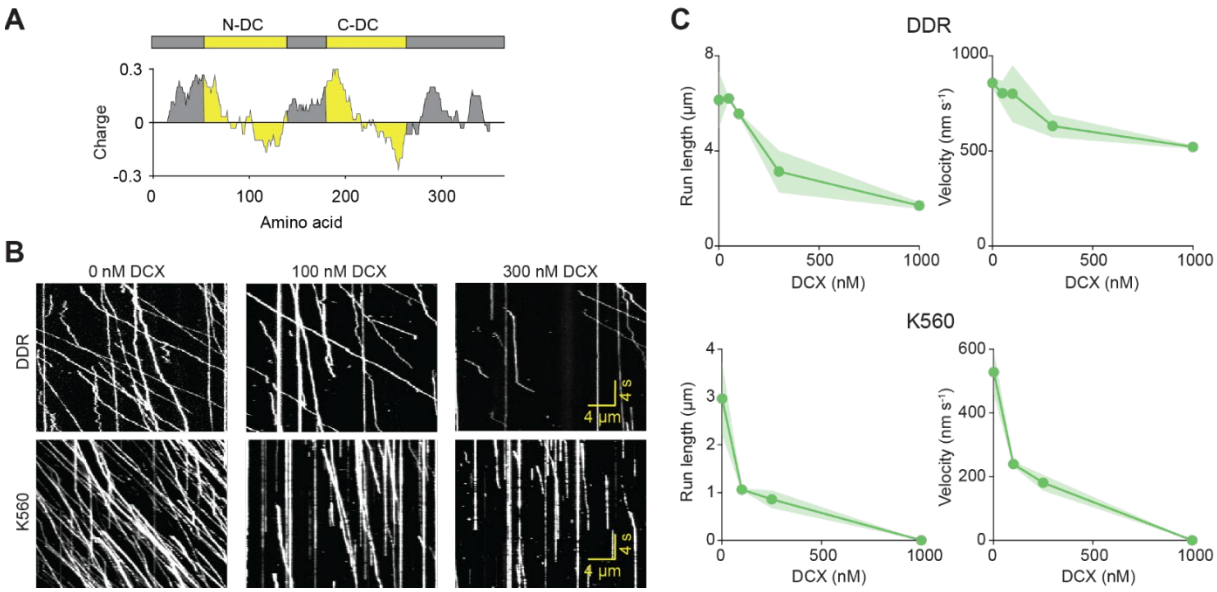


**Figure 24. Regulation of kinesin and dynein motility by DCX; related to Figure 17. (A)** Domain organization and charge distribution of DCX. DCX has an N-terminal and a C-terminal doublecortin domain (N-DC and C-DC, respectively) that bind to the MT. **(B)** Kymographs of DDR and K560 in the presence and absence of DCX. **(E)** The run frequency of DDR in different DCX concentrations. From left to right, N = 224, 237, 245, 104, 55 runs for DDR. **(F)** Kymographs of K560 with DCX. **(G)** The run frequency of K560 in different DCX concentrations. From left to right, N = 655, 187, 130, 0 runs for K560.

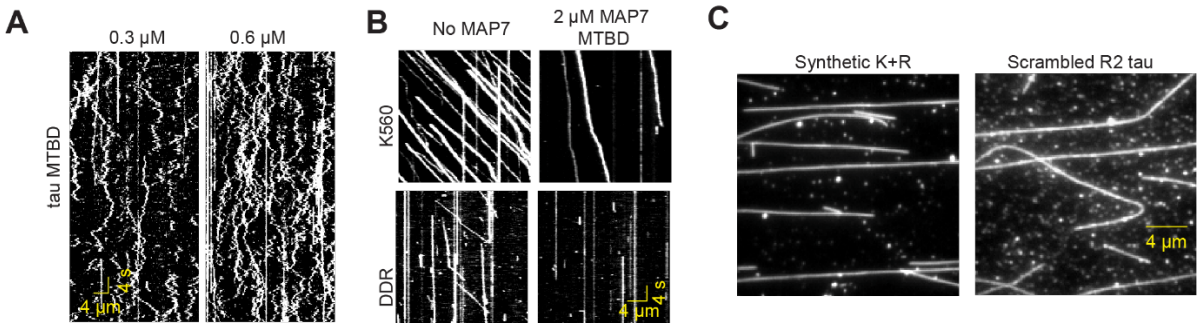


**Figure 25.** ***In vitro*** **characterization of truncated Map7 and tau constructs, and synthetic peptides; related to Figures 5 and 6. (A)** Kymographs show diffusion of tau MTBD on the MT in the absence of added salt. **(B)** Kymographs of K560 and DDR motility in the presence of MAP7 MTBD with 150 mM KAc and 0.1% methylcellulose. **(C)** Fluorescent images of synthetic peptides bound on the MT. "Synthetic K+R" is a scrambled sequence of 30 arginine (R), 30 lysine (K), 20 glycine (G), 20 serine (S) residues. "Scrambled R2 tau" is a scrambled sequence of the R2 repeat region in the MTBD of tau.

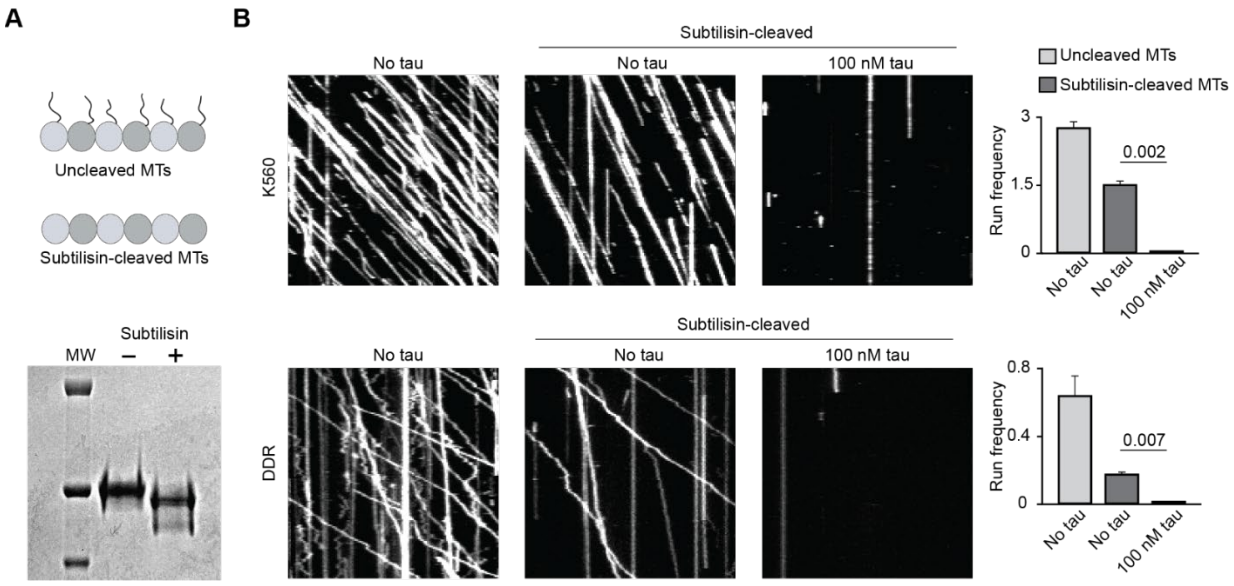


**Figure 26. Tau inhibits K560 and DDR motility even in the absence of E-hooks at the tubulin C-terminal tail; related to Figure 19. (A)** (Top) subtilisin treatment cleaves intrinsically-disordered tails of at the C-terminus of tubulin. (Bottom0 Denaturing gel shows reduce the reduction of the molecular weight (MW) of tubulin upon subtilisin treatment. **(B)** (Left) Kymographs of K560 and DDR motility on uncleaved and subtilisin-cleaved MTs in the presence and absence of 100 nM tau. The assay was performed without additive salt. (Right) The run frequency (mean ± s.e.m.) of K560 and DDR motility on uncleaved and subtilisin-cleaved MTs in the presence and absence of 100 nM tau. p-values are calculated from a two-tailed t-test.

## Methods

### Protein purification

Human MAP7 (UniProtKB Q14244-1), tau (UniProtKB P10636-8), and kinesin-1 (UniProtKB P33176-1) constructs have an N-terminal ZZ affinity tag, followed by a TEV protease cleavage sequence. MAP7 and tau constructs have an N-terminal ybbR sequence (DSLEFIASKLA)[105]. Kinesin constructs have a C-terminal GFP and a SNAP-tag connected by a 1x GS linker sequence. The mouse BicDR1 (UniProtKB A0JNT9-1) construct has a C-terminal SNAP-tag. The BicDR1:Nanobody construct has a C-terminal GFP nanobody followed by the SNAP-tag.

Protein purification was performed as previously described [27,96]. For MAP7 and tau constructs, a 500 mL cell pellet of Sf9 cells was thawed in 50 mL lysis buffer (25 mM HEPES pH 7.4, 1 M KCl, 10% glycerol, Roche protease inhibitor, 1 mM PMSF, 1 mM DTT, 1 mM ATP). The lysis was performed using a Wheaton glass dounce homogenizer. The lysate was spun for 45 min at 360,000 g in a Ti70 rotor. The supernatant was incubated with 1 mL IgG sepharose beads for 1 h. Beads were then washed in 50 mL lysis buffer and 50 mL storage buffer (25 mM HEPES pH 7.4, 300 mM KCl, 1 mM EGTA, 10 mM $MgCl_2$, 10% glycerol, 1 mM DTT, 1 mM ATP). Beads were resuspended with 1 mL storage buffer and transferred to a 2 mL Eppendorf tube. For SNAP-tag labeling, the bead-bound protein was incubated with 10 nmol SNAP-ligand conjugated dye for 1 h on ice. For ybbR-tag labeling, the bead-bound protein was incubated with coenzyme-A conjugated dye and 1 μM SFP enzyme for 1 h. After labeling, beads were washed with 50 mL storage buffer. Beads were resuspended with 2 mL storage buffer and mixed with 30 μL of 2 mg/mL TEV protease for 1 h for elution. For dynein and BicDR, the same procedure was used using different lysis (50 mM HEPES pH 7.4, 100 mM NaCl, 10% glycerol, 1 mM DTT, 1 mM ATP, 2 mM PMSF, 1 Roche tablet per 50 mL) and storage (50 mM Tris pH 7.4, 150 mM KAc, 2 mM $MgAc_2$, 1 mM EGTA, 10% glycerol, 1 mM ATP, 1 mM DTT) buffers.

$K350^{E236A}$ and DCX expression plasmids were transformed into Rosetta2 (DE3) pLysS cells. Bacteria were grown in YT media until the culture reached an $OD_{600}$ of 0.7. Cells were induced overnight at 20 °C with 0.2 M IPTG, spun down at 4,785 g for 15 min in a JLA 8.1 rotor, and combined with 50 mL lysis buffer (50 mM $NaH_2PO_4$, 250 mM NaCl, 2 mM $MgCl_2$, 30 mM imidazole, 10% glycerol, 1 mM DTT, 1 mM PMSF, pH 8.0). Cells were lysed with a sonicator and spun at 117,734 g in a Ti70 rotor. The supernatant was incubated with 1 mL of Ni-NTA beads for 1 h. Beads were washed with 50 mL wash buffer A (lysis buffer without PMSF), 50 mL wash buffer B (wash buffer A plus 750 mM additional NaCl) and exchanged back into wash buffer A. Protein was eluted with elution buffer (50 mM $NaH_2PO_4$ pH 7.2, 250 mM NaCl, 1 mM $MgCl_2$, 500 mM imidazole, 10% glycerol). For SFP, the same procedure was used with different lysis (20 mM Tris, 0.5 M NaCl, 5 mM imidazole, pH 8) and elution (20 mM Tris, 0.5 M NaCl, 500 mM imidazole, pH 8) buffers. Protein concentrations were determined with either Bradford

assay or absorbance at 280 nm on a Nanodrop spectrophotometer. Protein preps were run on an SDS-PAGE gel to check for purity and snap-frozen in liquid nitrogen for storage.

**Microscopy**

Fluorescence microscopy was performed using a Ti-E Eclipse inverted microscope body equipped with a 100x 1.49 NA Apo TIRF objective (Nikon). 488, 532 and 633 nm laser beams (Coherent) were fiber-coupled using laser-to-fiber couplers and a wave dimension multiplexer (OZ Optics). TIRF illumination was controlled using a TI-TIRF Motorized Illuminator unit (Nikon). The emission signal was filtered using 512/25, 580/40 697/75 nm bandpass filters (Chroma) mounted in a Lambda 10-B optical filter changer (Sutter). Images were collected with an electron-multiplied CCD camera (Andor, Ixon$^{+}$). The microscope was controlled using Micromanager. The effective pixel size after magnification was 160 nm.

**Motility assays**

Tubulin was purified from pig brain and labeled with biotin or fluorophores as described [71,88]. The final percentage of labeled tubulin in the MTs was less than 5%. Coverslips coated with PEG/PEG-Biotin (Microsurfaces) were assembled into flow chambers with laser-cut Parafilm. All solutions for motility assays were in MB buffer (30 mM HEPES, 5 mM $MgSO_4$, 1 mM EGTA, pH 7.0). 1 mg/mL streptavidin was added to the chamber and incubated for 2 min. Following three washes with 40 µL wash buffer (MB buffer supplemented with 0.5% Pluronic F-127, 1 mg/mL casein, 1 mM TCEP, 10 µM taxol), MTs were added to the chamber and allowed to attach for 2 min. Unattached MTs were removed by an extensive wash of the flow chamber and the chamber was exchanged into imaging buffer (wash buffer supplemented with 150 mM KAc, 0.1% methylcellulose, 1 mM ATP, glucose oxidase, catalase, 0.4% glucose, motors, and MAPs). The sample was sealed and imaged immediately. Reported MAP concentrations represent the concentration of MAP added to the imaging buffer.

All fitting was performed in OriginPro 9 or MATLAB 2016a. Binding curves of MAP7 and tau to MTs were fit to a Hill equation, $I = \frac{I_{max}[MAP]}{k_{sat}+[MAP]}$, and $k_{sat}$ was reported as half-maximal saturation, where "I" is fluorescence intensity on the MT. Motor inhibition by MAPs was fit to a single exponential decay function, where $IC_{50}$ is the decay rate by MAP concentration. For phase separation experiments, saturation concentration (*cSat*) was calculated from a sigmoidal logistic function, $A = A_{max}\left(1 + e^{-k([MAP]-cSat)}\right)^{-1}$, where $A$ surface area of liquid condensates, $A_{max}$ is the surface area of condensates at saturation, and $k$ is the logistic growth rate. The run frequency ($f$) of K560 was fitted to a two-component Hill equation $f = \frac{f_{max}}{\left(1+\left(\frac{K_a}{[MAP7]}\right)^{H_a}\right)\left(1+\left(\frac{[MAP7]}{K_i}\right)^{H_i}\right)}$, where $f_{max}$ is the maximum run frequency, $K_a$ is the half-maximum activating MAP7 concentration, $H_a$ is the Hill coefficient of activation, $K_i$ is the half-maximal inhibiting MAP7 concentration, and $H_i$ is the Hill coefficient of inhibition.

Partition coefficients were determined from the ratios of the fluorescence signal inside to outside the droplet. 10-pixel square box was drawn either inside or outside the droplet. For MT binding affinity measurements, a circle was drawn to a size slightly larger than the diameter of the MT. The signal inside the box or the circle was measured with the "Measure" function in ImageJ.

**KD assemblies**

The dynein complex (0.6 μM) was labeled with SNAP-LD655 on an N-terminal SNAP-tag on the dynein heavy chain and mixed with unlabeled dynactin (1 μM), and the BicDR1 construct (1 μM), which contains a C-terminal GFP-nanobody. After incubating the mixture on ice for 15 min, FL kinesin-1-GFP-SNAP labeled with LD555 (0.5 μM) was added and the mixture was incubated on ice for another 10 min. Biotinylated-MTs were attached to PEG-Biotin coverslips. Wash buffer included Pluronic and casein. The kinesin-dynein complex was diluted 500-fold in imaging buffer (wash buffer supplemented with 1 mM ATP, glucose oxidase, catalase, 0.4% glucose, and MAPs).

Movies were acquired using time-sharing between 532 and 633 nM laser exposures (200 ms each). Files were analyzed using Bio-Formats (ImageJ). In the "no MAP7" condition, immotile or diffusive spots in the dynein channel motors were attributed to dynein only motors. Stationary molecules were filtered from the kymograph in the Fourier space using a fast Fourier transform (FFT) mask in ImageJ. Two fluorescent channels were registered to identify trajectories that contain both fluorescent dyes. Velocities of these trajectories were measured by determining the distance between binding and dissociation and the time over which the motors stepped, including pauses and backtracking events.

**Sample Preparation for Cryo-EM**

Tubulin (Cytoskeleton) aliquots at 10 mg/ml tubulin in EM Buffer [80mM PIPES pH 6.9, 1mM EGTA, 1mM $MgCl_2$, and 1 mM GTP] were polymerized for 20 min at 37° C. MTs were then centrifuged at 17,000 g for 20 min. Each MT pellet was resuspended in 20 μL EM buffer supplemented with 1 mM DTT and 266 μM peloruside (an MT-stabilizing drug). Samples were incubated at a stoichiometry of 1:2 for MTs:MAP7-FL and 1:3:10 for MTs:MTBD-MAP7:Tau (Figure 23B) for 5 min in MB buffer supplemented with 10% NP-40 and 266 μM peloruside. MT concentration was set to 6 μM. 150 mM KAc was added to the MT solution before adding FL-MAP7. The MAP/MT mixtures were added to glow-discharged C-flat holey carbon grids (CF-1.2/1.3–4C, 400 mesh, copper; Protochips) inside a Vitrobot (FEI) set at 22 °C and 100% humidity before plunge-freezing in ethane slush and then transferred to liquid nitrogen, as previously described [49,109,120]( Figure 23A).

Because MTBD MAP7 binds the MT less strongly than FL MAP7, MAP7 MTBD and FL tau were incubated with MTs in the absence of added salt.

**Cryo-EM**

Micrographs were collected using an Arctica microscope (ThermoFisher) operated at an accelerating voltage of 200 kV. All cryo-EM images were recorded on a K2 Summit direct electron detector (Gatan), at a nominal magnification of 36,000×, corresponding to a calibrated pixel size of 1.14 Å. The camera was operated in superresolution mode, with a dose rate of ~1 e− per pixel $s^{-1}$ on the detector. We used an exposure time of 4 s, corresponding to a total dose of 45 electrons/ $Å^2$ on the specimen. The data were collected semiautomatically using the SerialEM software suite [121].

**Image Processing**

Stacks of dose-fractionated image frames were aligned using the UCSF MotionCor2 software. Images were corrected for drift and MT segments were manually selected from 2,000 and 800 images for MAP7-FL, and MAP7-MTBD and tau datasets, respectively, using the Helical Manual Picker in RELION. We estimated the Contrast Transfer Function (CTF) using CTFFIND4 and converted the segments to 90% overlapping boxes (512 × 512 pixels) for particle extraction using the helical picking feature in RELION. The remaining non-overlapping region is set to 82 Å and corresponds to the tubulin dimer repeat (asymmetric unit). Extracted particles were classified by PF number using the 3D classification feature in RELION. Finally, 13-PF MT particles (MAP7-FL dataset, 64,522 particles; MAP7-MTBD and tau co-dataset, 19,629 particles) were refined in FREALIGN, version 9.11 [122], using pseudo-helical symmetry. A schematic of the MT pipeline is outlined in Figure 23A.

**Co-sedimentation Assay**

Peloruside-stabilized MTs were incubated with combinations of MAP7 and kinesin at 25 °C for 10 min in MB buffer supplemented with 150 mM KAc, 1 mM DTT, and 2 mM peloruside. The final concentrations of MTs, kinesin, and MAP7 were 8, 16, and 24 μM, respectively. 100 μM AMP-PNP was added for stably tethering kinesin to MTs. After incubation, 20 μL reaction mixtures were centrifuged at 90,000 g for 15 min at 25 °C atop 20 μL of 50% glycerol cushion. The supernatant (20 μL) and the pellet (20 μL) were added to 5X SDS sample buffer, heated at 95 °C for 10 min, and loaded on denaturing 4-12% Bis-Tris gels (Invitrogen). The gels were stained with Coomassie blue and imaged using the Bio-Rad Gel Imager. Band intensities were determined using ImageJ and normalized to the MT pellet for each experiment.

**Reagents**

| REAGENT or RESOURCE | SOURCE | IDENTIFIER |
|---|---|---|
| Bacterial and Virus Strains | | |
| Competent cells | QB3 MacroLab | XL1-Blues |
| Competent cells | QB3 MacroLab | Rosetta2 (DE3) pLysS |
| Competent cells | QB3 MacroLab | DH10Bac |
| Insect cells | Berkeley Cell Culture Facility | Sf9 |
| | | |
| Chemicals, Peptides, and Recombinant Proteins | | |
| Glucose oxidase | Sigma | G2133 |
| Catalase | Sigma | C40 |
| Taxol | Sigma | T7191 |
| CoA Cy3 | Lumidyne | Custom synthesis |
| CoA Cy5 | Lumidyne | Custom synthesis |
| ATP | Sigma | A3377 |
| Pluronic F-127 | ThermoFisher | P6866 |
| Streptavidin | ThermoFischer | S888 |
| Methylcellulose | Sigma | M0512 |
| Casein | Sigma | C5890 |
| Taxol | Sigma | T7191 |
| TCEP | Sigma | C4706 |
| Human KIF5B (1-490 aa)::GFP:: SNAP | This study | N/A |
| Human KIF5B (1-560 aa) ::GFP:: SNAP | This study | N/A |
| Human KIF5B (1-963 aa) ::GFP:: SNAP | This study | N/A |
| Human KIF5B (1-350 aa, E236A) | | N/A |
| Human MAP7 (1-749 aa) | This study | N/A |
| Human ybbR::MAP7 (1-749 aa) | This study | N/A |
| Human ybbR::MAP7 (1-316 aa) | This study | N/A |
| Human ybbR::MAP7 (60-170 aa) | This study | N/A |
| Human ybbR::MAP7 (307-749 aa) | This study | N/A |
| Human ybbR::Tau (1-441 aa) | This study | N/A |
| Human ybbR::Tau (242-367 aa) | This study | N/A |
| Human DCX | | N/A |
| Porcine dynactin complex | | N/A |
| Human dynein complex | | N/A |
| Mouse BicDR1 (1-577 aa)::SNAP | This study | N/A |
| Mouse BicDR1 (1-577 aa)::SNAP::GFP nanobody | This study | N/A |

| | | |
|---|---|---|
| Tubulin | | N/A |
| SFP | | N/A |
| TEV protease | | N/A |
| | | |
| Critical Commercial Assays | | |
| BCA assay kit | ThermoScientific | 23250 |
| | | |
| Deposited Data | | |
| | | |
| | | |
| | | |
| | | |
| Recombinant DNA | | |
| Human DCX | Addgene | 83928 |
| Human KIF5B (1-490 aa)::GFP:: SNAP | This study | N/A |
| Human KIF5B (1-560 aa) ::GFP:: SNAP | This study | N/A |
| Human KIF5B (1-963 aa) ::GFP:: SNAP | This study | N/A |
| Human KIF5B (1-350 aa, E236A) | | N/A |
| Human MAP7 (1-749 aa) | This study | N/A |
| Human ybbR::MAP7 (1-749 aa) | This study | N/A |
| Human ybbR::MAP7 (1-316 aa) | This study | N/A |
| Human ybbR::MAP7 (60-170 aa) | This study | N/A |
| Human ybbR::MAP7 (307-749 aa) | This study | N/A |
| Human ybbR::Tau (1-441 aa) | This study | N/A |
| Human ybbR::Tau (242-367 aa) | This study | N/A |
| Human dynein complex | | N/A |
| Mouse BicDR1 (1-577 aa)::SNAP | This study | N/A |
| Mouse BicDR1 (1-577 aa)::SNAP::GFP nanobody | This study | N/A |
| | | |
| Software and Algorithms | | |
| ImageJ | ImageJ | https://imagej.nih.gov/ij/ |
| Matlab | MathWorks | https://www.mathworks.com/ |
| Origin | OriginLab | https://www.originlab.com/ |
| BoxPlotR | BoxPlotR | http://shiny.chemgrid.org/boxplotr/ |
| Protein disorder prediction | IUPred2A | https://iupred2a.elte.hu/ |

| | | |
|---|---|---|
| Protein charge distribution | EMBOSS | http://www.bioinformatics.nl/cgi-bin/emboss/charge |
| Amino acid sequence shuffle | SMS | https://www.bioinformatics.org/sms2/shuffle_protein.html |
| | | |
| Other | | |
| Biotin PEG coverslips | Microsurfaces | Bio-02 |
| Ni-NTA beads | Thermo Scientific | 88221 |
| IgG sepharose beads | GE Healthcare | 17096902 |
| Glass dounce | Wheaton | 357544 |
| cOmplete, Mini, EDTA-free Protease Inhibitor Cocktail | Sigma | 11836170001 |

## Chapter IV: Concluding remarks

### Are MAPs inhibitory to motors *in vivo*?

In neurons, a motor carrying its cargo from one side of the cell to another would encounter many different MAPs on MTs. For example, kinesin would interact with MAP7, MAP1, MAP9, tau, DCX, DCLK1 and many others as it travels though the axon [39]. Our model predicts that MAPs are inhibitory to motors, in general, either through steric clash or the positive charges on the MTBD. A motor can overcome this inhibition by forming favorable interactions with a specific MAP. Kinesin has a build-in interaction domain with MAP7 and this allows it to overcome the negative interactions due to MAP7's MT-binding domain. Yet, it remains unclear how kinesin walks in the presence of the other MAPs that inhibit kinesin motility *in vitro.*

Built-in interactions between a motor with its favorable MAP might be sufficient to overcome the negative interactions with other MAPs, but this view has not been supported by *in vitro* studies. For example, the inhibition of kinesin-1 by DCX on the MT is not rescued by adding MAP7 to the MT [39]. As an alternative possibility, tubulin PTMs may play a major role in regulating MAP-motor interactions. A live cell imaging study showed that tubulin PTMs are not uniformly distributed on adjacent MTs in neurons, and a subset of these MTs are coated with a singular or a group of modifications [123]. It is possible that PTMs also tightly regulate the recruitment of specific MAPs to MTs, and these serve as tracks for motors that interact with those MAPs to transport cargo.

Besides motors, other components of the MT transport machinery can form favorable interactions with a MAP, which would allow the cargos to be transported along those MTs. For example, there may be a single or a class of cargo adaptors that can bind to both motors and MAPs. JIP1 is such cargo adaptor that binds to both kinesin-1 and dynein [124]. Interestingly, JIP-1 contains an SH3 domain which is known to interact with proline-rich regions of proteins. Tau, MAP7, DCX and other MAPs have proline-rich regions removed from the MT-binding domain. This give rise to the possibility that a kinesin motor with JIP1 bound would be able to walk though diverse MAP-coated MTs because the JIP1 is able to interact with a large number of MAP types. Other proteins have also been proposed to regulate the interactions between MAPs and motors. Mapmodulin has a disordered C-terminal domain that mimics the C-terminal tail of tubulin [101,125]. As a trimer, it is possible that mapmodulin could use its C-terminal sequence to bridge an interaction between motors and MAPs and enable motors to enter into MAP condensates. Future studies could look for other possible "global MAP-motor adaptors" by mass spectrometry studies of proteins that pull down with MAP-coated MTs.

## Implications for disease

Tau aggregates are a hallmark of multiple neurodegenerative diseases [104]. However, the mechanism that underlies tau's pathological effect remains to be studied. Aggregation could potentially lead to MT instability and subsequent breakdown of the MTs in the axon [30]. However, other MAPs also stabilize MTs and tau -/- mice are still viable [126]. Tau is abnormally post-translationally modified in Alzheimer's disease. Residues in the proline-rich domain become highly phosphorylated in disease. Phosphorylation is known to reduce the affinity of SH3 binding partners. If JIP1 is indeed required for motors to walk on tau bound MTs, it is possible that tau phosphorylation would interfere with this process. Lysine resides in the MT-binding domain of tau are acetylated, converting them from positively charged to polar [55]. We predict that lysine acetylation would substantially affect the ability of tau to inhibit motors, because its MT-binding domain would be less positively charged. This may lead to a misregulation of cargo transport in the axon. Further work could investigate how kinesin and dynein are affected by PTMs on tau.

## References


1 Verhey, K. J., Kaul, N. & Soppina, V. Kinesin assembly and movement in cells. *Annual review of biophysics* 40, 267-288, doi:10.1146/annurev-biophys-042910-155310 (2011).

2 Reck-Peterson, S. L., Redwine, W. B., Vale, R. D. & Carter, A. P. The cytoplasmic dynein transport machinery and its many cargoes. *Nature reviews. Molecular cell biology* 19, 382-398, doi:10.1038/s41580-018-0004-3 (2018).

3 Schliwa, M. Myosin steps backwards. *Nature* 401, 431-432, doi:10.1038/46692 (1999).

4 Roberts, A. J. *et al.* AAA+ Ring and linker swing mechanism in the dynein motor. *Cell* 136, 485-495, doi:10.1016/j.cell.2008.11.049 (2009).

5 Schmidt, H., Gleave, E. S. & Carter, A. P. Insights into dynein motor domain function from a 3.3-A crystal structure. *Nature structural & molecular biology* 19, 492-497, S491, doi:10.1038/nsmb.2272 (2012).

6 Kon, T. *et al.* The 2.8 A crystal structure of the dynein motor domain. *Nature* 484, 345-350, doi:10.1038/nature10955 (2012).

7 Can, S., Lacey, S., Gur, M., Carter, A. P. & Yildiz, A. Directionality of dynein is controlled by the angle and length of its stalk. *Nature* 566, 407-410, doi:10.1038/s41586-019-0914-z (2019).

8 Busson, S., Dujardin, D., Moreau, A., Dompierre, J. & De Mey, J. R. Dynein and dynactin are localized to astral microtubules and at cortical sites in mitotic epithelial cells. *Current biology : CB* 8, 541-544 (1998).

9 Sharp, D. J., Rogers, G. C. & Scholey, J. M. Microtubule motors in mitosis. *Nature* 407, 41-47 (2000).

10 Nogales, E. Structural insights into microtubule function. *Annu Rev Biochem* 69, 277-302, doi:10.1146/annurev.biochem.69.1.277 (2000).
11 Ramkumar, A., Jong, B. Y. & Ori-McKenney, K. M. ReMAPping the microtubule landscape: How phosphorylation dictates the activities of microtubule-associated proteins. *Dev Dyn* 247, 138-155, doi:10.1002/dvdy.24599 (2018).
12 Li, L., Alper, J. & Alexov, E. Cytoplasmic dynein binding, run length, and velocity are guided by long-range electrostatic interactions. *Sci Rep* 6, 31523, doi:10.1038/srep31523 (2016).
13 Bodakuntla, S., Jijumon, A. S., Villablanca, C., Gonzalez-Billault, C. & Janke, C. Microtubule-Associated Proteins: Structuring the Cytoskeleton. *Trends in cell biology* 29, 804-819, doi:10.1016/j.tcb.2019.07.004 (2019).
14 Vale, R. D., Reese, T. S. & Sheetz, M. P. Identification of a novel force-generating protein, kinesin, involved in microtubule-based motility. *Cell* 42, 39-50 (1985).
15 Brady, S. T. A novel brain ATPase with properties expected for the fast axonal transport motor. *Nature* 317, 73-75 (1985).
16 Hirokawa, N., Noda, Y., Tanaka, Y. & Niwa, S. Kinesin superfamily motor proteins and intracellular transport. *Nature reviews. Molecular cell biology* 10, 682-696, doi:10.1038/nrm2774 (2009).
17 Paschal, B. M. *et al.* Isolated flagellar outer arm dynein translocates brain microtubules in vitro. *Nature* 330, 672-674, doi:10.1038/330672a0 (1987).
18 Roberts, A. J., Kon, T., Knight, P. J., Sutoh, K. & Burgess, S. A. Functions and mechanics of dynein motor proteins. *Nature reviews. Molecular cell biology* 14, 713-726, doi:10.1038/nrm3667 (2013).
19 Perrone, C. A. *et al.* A novel dynein light intermediate chain colocalizes with the retrograde motor for intraflagellar transport at sites of axoneme assembly in chlamydomonas and Mammalian cells. *Molecular biology of the cell* 14, 2041-2056, doi:10.1091/mbc.E02-10-0682 (2003).
20 McKenney, R. J., Huynh, W., Tanenbaum, M. E., Bhabha, G. & Vale, R. D. Activation of cytoplasmic dynein motility by dynactin-cargo adapter complexes. *Science* 345, 337-341, doi:10.1126/science.1254198 (2014).
21 Urnavicius, L. *et al.* Cryo-EM shows how dynactin recruits two dyneins for faster movement. *Nature* 554, 202-206, doi:doi:10.1038/nature25462 (2018).
22 Grotjahn, D. A. *et al.* Cryo-electron tomography reveals that dynactin recruits a team of dyneins for processive motility. *Nature Structural & Molecular Biology* 25, 203-207, doi:doi:10.1038/s41594-018-0027-7 (2018).
23 Yildiz, A., Tomishige, M., Vale, R. D. & Selvin, P. R. Kinesin walks hand-over-hand. *Science* 303, 676-678, doi:10.1126/science.1093753 (2004).
24 Asbury, C. L., Fehr, A. N. & Block, S. M. Kinesin moves by an asymmetric hand-over-hand mechanism. *Science* 302, 2130-2134 (2003).

25 DeWitt, M. A., Chang, A. Y., Combs, P. A. & Yildiz, A. Cytoplasmic dynein moves through uncoordinated stepping of the AAA+ ring domains. *Science* 335, 221-225, doi:10.1126/science.1215804 (2012).
26 Qiu, W. *et al.* Dynein achieves processive motion using both stochastic and coordinated stepping. *Nature structural & molecular biology* 19, 193-200, doi:10.1038/nsmb.2205 (2012).
27 Zhang, K. *et al.* Cryo-EM Reveals How Human Cytoplasmic Dynein Is Auto-inhibited and Activated. *Cell* 169, 1303-1314 e1318, doi:10.1016/j.cell.2017.05.025 (2017).
28 Friedman, D. S. & Vale, R. D. Single-molecule analysis of kinesin motility reveals regulation by the cargo-binding tail domain. *Nature cell biology* 1, 293-297, doi:10.1038/13008 (1999).
29 Kelliher, M. T. *et al.* Autoinhibition of kinesin-1 is essential to the dendrite-specific localization of Golgi outposts. *J Cell Biol* 217, 2531-2547, doi:10.1083/jcb.201708096 (2018).
30 Vossel, K. A. *et al.* Tau reduction prevents Aβ-induced axonal transport deficits by blocking activation of GSK3β. *J Cell Biol* 209, 419-433, doi:10.1083/jcb.201407065 (2015).
31 Hancock, W. O. Bidirectional cargo transport: moving beyond tug of war. *Nature reviews. Molecular cell biology* 15, 615-628, doi:10.1038/nrm3853 (2014).
32 Encalada, S. E., Szpankowski, L., Xia, C. H. & Goldstein, L. S. Stable kinesin and dynein assemblies drive the axonal transport of mammalian prion protein vesicles. *Cell* 144, 551-565, doi:10.1016/j.cell.2011.01.021 (2011).
33 Kaplan, L., Ierokomos, A., Chowdary, P., Bryant, Z. & Cui, B. Rotation of endosomes demonstrates coordination of molecular motors during axonal transport. *Sci Adv* 4, e1602170, doi:10.1126/sciadv.1602170 (2018).
34 Chowdary, P., Che, D., Zhang, K. & Cui, B. in *Biophys J* Vol. 108 2691-2703 (2015).
35 Derr, N. D. *et al.* Tug-of-war in motor protein ensembles revealed with a programmable DNA origami scaffold. *Science* 338, 662-665, doi:10.1126/science.1226734 (2012).
36 Elshenawy, M. M. *et al.* Cargo adaptors regulate stepping and force generation of mammalian dynein-dynactin. *Nat Chem Biol* 15, 1093-1101, doi:10.1038/s41589-019-0352-0 (2019).
37 Che, D. L., Chowdary, P. D. & Cui, B. A close look at axonal transport: Cargos slow down when crossing stationary organelles. *Neurosci Lett* 610, 110-116, doi:10.1016/j.neulet.2015.10.066 (2016).
38 Rai, A. *et al.* Dynein Clusters into Lipid Microdomains on Phagosomes to Drive Rapid Transport toward Lysosomes. *Cell* 164, 722-734, doi:10.1016/j.cell.2015.12.054 (2016).
39 Monroy, B. Y. *et al.* A Combinatorial MAP Code Dictates Polarized Microtubule Transport. *Dev Cell*, doi:10.1016/j.devcel.2020.01.029 (2020).
40 Liang, W. H. *et al.* Microtubule Defects Influence Kinesin-Based Transport In Vitro. *Biophysical journal* 110, 2229-2240, doi:10.1016/j.bpj.2016.04.029 (2016).

41 Schneider, R., Korten, T., Walter, W. J. & Diez, S. Kinesin-1 motors can circumvent permanent roadblocks by side-shifting to neighboring protofilaments. *Biophysical journal* 108, 2249-2257, doi:10.1016/j.bpj.2015.03.048 (2015).

42 Dixit, R., Ross, J. L., Goldman, Y. E. & Holzbaur, E. L. Differential Regulation of Dynein and Kinesin Motor Proteins by Tau. *Science*, doi:1152993 [pii] 10.1126/science.1152993 (2008).

43 Telley, I. A., Bieling, P. & Surrey, T. Obstacles on the microtubule reduce the processivity of Kinesin-1 in a minimal in vitro system and in cell extract. *Biophysical journal* 96, 3341-3353, doi:10.1016/j.bpj.2009.01.015 (2009).

44 Leduc, C. *et al.* Molecular crowding creates traffic jams of kinesin motors on microtubules. *Proceedings of the National Academy of Sciences of the United States of America* 109, 6100-6105, doi:10.1073/pnas.1107281109 (2012).

45 Hoeprich, G. J., Thompson, A. R., McVicker, D. P., Hancock, W. O. & Berger, C. L. Kinesin's neck-linker determines its ability to navigate obstacles on the microtubule surface. *Biophysical journal* 106, 1691-1700, doi:10.1016/j.bpj.2014.02.034 (2014).

46 Ruensern Tan, A. J. L., Tracy Tan, Jisoo Han, Dan W. Nowakowski, Michael Vershinin, Sergi Simo, Kassandra M. Ori-McKenney, Richard J. McKenney. Microtubules Gate Tau Condensation to Spatially Regulate Microtubule Functions. *biorXiv*, doi:https://doi.org/10.1101/423376 (2019).

47 Tymanskyj, S. R., Yang, B. H., Verhey, K. J. & Ma, L. MAP7 regulates axon morphogenesis by recruiting kinesin-1 to microtubules and modulating organelle transport. *eLife* 7, doi:10.7554/eLife.36374 (2018).

48 Barlan, K., Lu, W. & Gelfand, V. I. The microtubule-binding protein ensconsin is an essential cofactor of kinesin-1. *Curr Biol* 23, 317-322, doi:10.1016/j.cub.2013.01.008 (2013).

49 Kellogg, E. H. *et al.* Near-atomic model of microtubule-tau interactions. *Science* 360, 1242-1246, doi:10.1126/science.aat1780 (2018).

50 Manka, S. W. & Moores, C. A. Pseudo-repeats in doublecortin make distinct mechanistic contributions to microtubule regulation. *bioRxiv*, 808899, doi:10.1101/808899 (2019).

51 Luo, Y. *et al.* Direct observation of dynamic protein interactions involving human microtubules using solid-state NMR spectroscopy. *Nature Communications* 11, 1-10, doi:doi:10.1038/s41467-019-13876-x (2020).

52 Semenova, I. *et al.* Regulation of microtubule-based transport by MAP4. *Mol Biol Cell* 25, 3119-3132, doi:10.1091/mbc.E14-01-0022 (2014).

53 Hooikaas, P. J. *et al.* MAP7 family proteins regulate kinesin-1 recruitment and activation. *J Cell Biol* 218, 1298-1318, doi:10.1083/jcb.201808065 (2019).

54 Liu, J. S. *et al.* Molecular basis for specific regulation of neuronal kinesin-3 motors by doublecortin family proteins. *Mol Cell* 47, 707-721, doi:10.1016/j.molcel.2012.06.025 (2012).

55 Arakhamia, T. *et al.* Posttranslational Modifications Mediate the Structural Diversity of Tauopathy Strains. *Cell* 180, 633-644.e612, doi:10.1016/j.cell.2020.01.027 (2020).
56 Ebneth, A. *et al.* Overexpression of tau protein inhibits kinesin-dependent trafficking of vesicles, mitochondria, and endoplasmic reticulum: implications for Alzheimer's disease. *J Cell Biol* 143, 777-794, doi:10.1083/jcb.143.3.777 (1998).
57 Sang, T. K. & Jackson, G. R. Drosophila models of neurodegenerative disease. *NeuroRx* 2, 438-446, doi:10.1602/neurorx.2.3.438 (2005).
58 Monroy, B. Y. *et al.* Competition between microtubule-associated proteins directs motor transport. *Nature communications* 9, 1487, doi:10.1038/s41467-018-03909-2 (2018).
59 Tan, R. *et al.* Microtubules gate tau condensation to spatially regulate microtubule functions. *Nature cell biology* 21, 1078-1085, doi:10.1038/s41556-019-0375-5 (2019).
60 Banani, S. F., Lee, H. O., Hyman, A. A. & Rosen, M. K. Biomolecular condensates: organizers of cellular biochemistry. *Nat Rev Mol Cell Biol* 18, 285-298, doi:10.1038/nrm.2017.7 (2017).
61 Hyman, A. A., Weber, C. A. & Julicher, F. Liquid-liquid phase separation in biology. *Annual review of cell and developmental biology* 30, 39-58, doi:10.1146/annurev-cellbio-100913-013325 (2014).
62 Jain, A. & Vale, R. D. RNA phase transitions in repeat expansion disorders. *Nature* 546, 243-247, doi:10.1038/nature22386 (2017).
63 DW, S. *et al.* Competing Protein-RNA Interaction Networks Control Multiphase Intracellular Organization. *Cell* 181, doi:10.1016/j.cell.2020.03.050 (2020).
64 Riback, J. A. *et al.* Composition dependent phase separation underlies directional flux through the nucleolus. doi:10.1101/809210 (2019).
65 Bechstedt, S. & Brouhard, G. J. Doublecortin recognizes the 13-protofilament microtubule cooperatively and tracks microtubule ends. *Dev Cell* 23, 181-192, doi:10.1016/j.devcel.2012.05.006 (2012).
66 Siahaan, V. *et al.* Kinetically distinct phases of tau on microtubules regulate kinesin motors and severing enzymes. *Nature cell biology* 21, 1086-1092, doi:10.1038/s41556-019-0374-6 (2019).
67 King, M. R. & Petry, S. Phase separation of TPX2 enhances and spatially coordinates microtubule nucleation. *Nat Commun* 11, 270, doi:10.1038/s41467-019-14087-0 (2020).
68 Hernandez-Vega, A. *et al.* Local Nucleation of Microtubule Bundles through Tubulin Concentration into a Condensed Tau Phase. *Cell Rep* 20, 2304-2312, doi:10.1016/j.celrep.2017.08.042 (2017).
69 Altman, R. B. *et al.* Cyanine fluorophore derivatives with enhanced photostability. *Nature methods* 9, 68-71, doi:10.1038/nmeth.1774 (2011).
70 Fish, K. N. Total internal reflection fluorescence (TIRF) microscopy. *Curr Protoc Cytom* Chapter 12, Unit12.18, doi:10.1002/0471142956.cy1218s50 (2009).

71 Castoldi, M. & Popov, A. V. Purification of brain tubulin through two cycles of polymerization-depolymerization in a high-molarity buffer. *Protein Expr Purif* 32, 83-88, doi:10.1016/s1046-5928(03)00218-3 (2003).
72 Reck-Peterson, S. L., Redwine, W. B., Vale, R. D. & Carter, A. P. The cytoplasmic dynein transport machinery and its many cargoes. *Nature reviews. Molecular cell biology*, doi:10.1038/s41580-018-0004-3 (2018).
73 Ray, S., Meyhofer, E., Milligan, R. A. & Howard, J. Kinesin follows the microtubule's protofilament axis. *J Cell Biol* 121, 1083-1093 (1993).
74 Can, S., Dewitt, M. A. & Yildiz, A. Bidirectional helical motility of cytoplasmic dynein around microtubules. *eLife* 3, e03205, doi:10.7554/eLife.03205 (2014).
75 Feng, Q., Mickolajczyk, K. J., Chen, G. Y. & Hancock, W. O. Motor Reattachment Kinetics Play a Dominant Role in Multimotor-Driven Cargo Transport. *Biophys J* 114, 400-409, doi:10.1016/j.bpj.2017.11.016 (2018).
76 Soundararajan, H. C. & Bullock, S. L. The influence of dynein processivity control, MAPs, and microtubule ends on directional movement of a localising mRNA. *eLife* 3, e01596, doi:10.7554/eLife.01596 (2014).
77 Schlager, M. A., Hoang, H. T., Urnavicius, L., Bullock, S. L. & Carter, A. P. In vitro reconstitution of a highly processive recombinant human dynein complex. *The EMBO journal* 33, 1855-1868, doi:10.15252/embj.201488792 (2014).
78 Trokter, M., Mücke, N. & Surrey, T. Reconstitution of the human cytoplasmic dynein complex. doi:10.1073/pnas.1210573110 (2012).
79 Singleton, M. R., Dillingham, M. S. & Wigley, D. B. Structure and mechanism of helicases and nucleic acid translocases. *Annu Rev Biochem* 76, 23-50, doi:10.1146/annurev.biochem.76.052305.115300 (2007).
80 Levi, V., Serpinskaya, A. S., Gratton, E. & Gelfand, V. Organelle transport along microtubules in Xenopus melanophores: evidence for cooperation between multiple motors. *Biophys J* 90, 318-327, doi:10.1529/biophysj.105.067843 (2006).
81 Blehm, B. H., Schroer, T. A., Trybus, K. M., Chemla, Y. R. & Selvin, P. R. In vivo optical trapping indicates kinesin's stall force is reduced by dynein during intracellular transport. *Proceedings of the National Academy of Sciences of the United States of America* 110, 3381-3386, doi:10.1073/pnas.1219961110 (2013).
82 Belyy, V. *et al.* The mammalian dynein-dynactin complex is a strong opponent to kinesin in a tug-of-war competition. *Nature cell biology* 18, 1018-1024, doi:10.1038/ncb3393 (2016).
83 Reck-Peterson, S. L. *et al.* Single-molecule analysis of dynein processivity and stepping behavior. *Cell* 126, 335-348, doi:10.1016/j.cell.2006.05.046 (2006).
84 Nelson, S. R., Trybus, K. M. & Warshaw, D. M. Motor coupling through lipid membranes enhances transport velocities for ensembles of myosin Va. *Proc Natl Acad Sci U S A* 111, E3986-3995, doi:10.1073/pnas.1406535111 (2014).

85 Verdeny-Vilanova, I. *et al.* 3D motion of vesicles along microtubules helps them to circumvent obstacles in cells. *Journal of cell science* 130, 1904-1916, doi:10.1242/jcs.201178 (2017).
86 Nitzsche, B., Ruhnow, F. & Diez, S. in *Nat Nanotechnol* Vol. 3 552-556 (2008).
87 Tjioe, M. *et al.* Asymmetric Tug-of-War leads to Cooperative Transport of a Cargo by Multiple Kinesins. *biorxiv*, doi:10.1101/544080 (2019).
88 Nicholas, M. P., Rao, L. & Gennerich, A. Covalent immobilization of microtubules on glass surfaces for molecular motor force measurements and other single-molecule assays. *Methods Mol Biol* 1136, 137-169, doi:10.1007/978-1-4939-0329-0_9 (2014).
89 Jaqaman, K. *et al.* Robust single-particle tracking in live-cell time-lapse sequences. *Nat Methods* 5, 695-702, doi:10.1038/nmeth.1237 (2008).
90 DeWitt, M. A., Cypranowska, C. A., Cleary, F. B., Belyy, V. & Yildiz, A. The AAA3 domain of cytoplasmic dynein acts as a switch to facilitate microtubule release. *Nature structural & molecular biology* 22, 73-80, doi:10.1038/nsmb.2930 (2015).
91 Qin, D., Xia, Y. & Whitesides, G. M. Soft lithography for micro- and nanoscale patterning. *Nat Protoc* 5, 491-502, doi:10.1038/nprot.2009.234 (2010).
92 Thery, M. & Piel, M. Adhesive micropatterns for cells: a microcontact printing protocol. *Cold Spring Harb Protoc* 2009, pdb.prot5255, doi:10.1101/pdb.prot5255 (2009).
93 Eddington, D., Puccinelli, J. & J. Beebe, D. *Thermal Aging and Reduced Hydrophobic Recovery of Polydimethylsiloxane*. Vol. 114 (2006).
94 Lee, J. N., Park, C. & Whitesides, G. M. Solvent compatibility of poly(dimethylsiloxane)-based microfluidic devices. *Anal Chem* 75, 6544-6554, doi:10.1021/ac0346712 (2003).
95 McKenney, R. J., Huynh, W., Vale, R. D. & Sirajuddin, M. Tyrosination of α-tubulin controls the initiation of processive dynein-dynactin motility. *Embo j* 35, 1175-1185, doi:10.15252/embj.201593071 (2016).
96 Ferro, L. S., Can, S., Turner, M. A., ElShenawy, M. M. & Yildiz, A. Kinesin and dynein use distinct mechanisms to bypass obstacles. *eLife* 8, doi:10.7554/eLife.48629 (2019).
97 Tjioe, M. *et al.* Multiple kinesins induce tension for smooth cargo transport. *Elife* 8, doi:10.7554/eLife.50974 (2019).
98 Shigematsu, H. *et al.* Structural insight into microtubule stabilization and kinesin inhibition by Tau family MAPs. *J Cell Biol* 217, 4155-4163, doi:10.1083/jcb.201711182 (2018).
99 Voter, W. A. & Erickson, H. P. Electron microscopy of MAP 2 (microtubule-associated protein 2). *J Ultrastruct Res* 80, 374-382, doi:10.1016/s0022-5320(82)80051-8 (1982).
100 Chen, J., Kanai, Y., Cowan, N. J. & Hirokawa, N. Projection domains of MAP2 and tau determine spacings between microtubules in dendrites and axons. *Nature* 360, 674-677, doi:doi:10.1038/360674a0 (2020).

101 Ulitzur, N., Humbert, M. & Pfeffer, S. R. Mapmodulin: a possible modulator of the interaction of microtubule-associated proteins with microtubules. *Proc Natl Acad Sci U S A* 94, 5084-5089, doi:10.1073/pnas.94.10.5084 (1997).
102 Paschal, B. M., Obar, R. A. & Vallee, R. B. Interaction of brain cytoplasmic dynein and MAP2 with a common sequence at the C terminus of tubulin. *Nature* 342, 569-572, doi:10.1038/342569a0 (1989).
103 Dixit, R., Ross, J. L., Goldman, Y. E. & Holzbaur, E. L. Differential regulation of dynein and kinesin motor proteins by tau. *Science* 319, 1086-1089, doi:10.1126/science.1152993 (2008).
104 Wegmann, S. *et al.* Tau protein liquid-liquid phase separation can initiate tau aggregation. *Embo j* 37, doi:10.15252/embj.201798049 (2018).
105 Yin, J. *et al.* Genetically encoded short peptide tag for versatile protein labeling by Sfp phosphopantetheinyl transferase. *Proc Natl Acad Sci U S A* 102, 15815-15820, doi:10.1073/pnas.0507705102 (2005).
106 Vershinin, M., Carter, B. C., Razafsky, D. S., King, S. J. & Gross, S. P. Multiple-motor based transport and its regulation by Tau. *Proceedings of the National Academy of Sciences of the United States of America* 104, 87-92, doi:10.1073/pnas.0607919104 (2007).
107 Valenstein, M. L. & Roll-Mecak, A. Graded Control of Microtubule Severing by Tubulin Glutamylation. *Cell* 164, 911-921, doi:10.1016/j.cell.2016.01.019 (2016).
108 Chaudhary, A. R. *et al.* MAP7 regulates organelle transport by recruiting kinesin-1 to microtubules. *J Biol Chem* 294, 10160-10171, doi:10.1074/jbc.RA119.008052 (2019).
109 Eshun-Wilson, L. *et al.* Effects of α-tubulin acetylation on microtubule structure and stability. doi:10.1073/pnas.1900441116 (2019).
110 Sui, H. & Downing, K. H. Structural basis of interprotofilament interaction and lateral deformation of microtubules. *Structure* 18, 1022-1031, doi:10.1016/j.str.2010.05.010 (2010).
111 Shang, Z. *et al.* High-resolution structures of kinesin on microtubules provide a basis for nucleotide-gated force-generation. *eLife* 3, e04686, doi:10.7554/eLife.04686 (2014).
112 Redwine, W. B. *et al.* Structural basis for microtubule binding and release by dynein. *Science* 337, 1532-1536, doi:10.1126/science.1224151 (2012).
113 Wang, Z. & Sheetz, M. P. The C-terminus of tubulin increases cytoplasmic dynein and kinesin processivity. *Biophys J* 78, 1955-1964, doi:10.1016/s0006-3495(00)76743-9 (2000).
114 Lacey, S. E., He, S., Scheres, S. H. & Carter, A. P. Cryo-EM of dynein microtubule-binding domains shows how an axonemal dynein distorts the microtubule. *eLife* 8, doi:10.7554/eLife.47145 (2019).
115 Drechsler, H., Xu, Y., Geyer, V. F., Zhang, Y. & Diez, S. in *Mol Biol Cell* Vol. 30 2953-2968 (2019).

116 Fumagalli, L. *et al.* C9orf72-derived arginine-containing dipeptide repeats associate with axonal transport machinery and impede microtubule-based motility. *bioRxiv*, 835082, doi:10.1101/835082 (2019).
117 Kaul, N., Soppina, V. & Verhey, K. J. Effects of α-tubulin K40 acetylation and detyrosination on kinesin-1 motility in a purified system. *Biophys J* 106, 2636-2643, doi:10.1016/j.bpj.2014.05.008 (2014).
118 Li, P. *et al.* Phase transitions in the assembly of multivalent signalling proteins. *Nature* 483, 336-340, doi:10.1038/nature10879 (2012).
119 Goode, B. L. *et al.* Functional interactions between the proline-rich and repeat regions of tau enhance microtubule binding and assembly. *Mol Biol Cell* 8, 353-365, doi:10.1091/mbc.8.2.353 (1997).
120 Zhang, R., Alushin, G. M., Brown, A. & Nogales, E. Mechanistic Origin of Microtubule Dynamic Instability and Its Modulation by EB Proteins. *Cell* 162, 849-859, doi:10.1016/j.cell.2015.07.012 (2015).
121 Mastronarde, D. N. Automated electron microscope tomography using robust prediction of specimen movements. *J Struct Biol* 152, 36-51, doi:10.1016/j.jsb.2005.07.007 (2005).
122 Grigorieff, N. Frealign: An Exploratory Tool for Single-Particle Cryo-EM. *Methods Enzymol* 579, 191-226, doi:10.1016/bs.mie.2016.04.013 (2016).
123 Tas, R. P. *et al.* Differentiation between Oppositely Oriented Microtubules Controls Polarized Neuronal Transport. *Neuron* 96, 1264-1271.e1265, doi:10.1016/j.neuron.2017.11.018 (2017).
124 Fu, M. M. & Holzbaur, E. L. JIP1 regulates the directionality of APP axonal transport by coordinating kinesin and dynein motors. *J Cell Biol* 202, 495-508, doi:10.1083/jcb.201302078 (2013).
125 Itin, C., Ulitzur, N., Mühlbauer, B. & Pfeffer, S. R. Mapmodulin, cytoplasmic dynein, and microtubules enhance the transport of mannose 6-phosphate receptors from endosomes to the trans-golgi network. *Mol Biol Cell* 10, 2191-2197, doi:10.1091/mbc.10.7.2191 (1999).
126 Lei, P. *et al.* Motor and cognitive deficits in aged tau knockout mice in two background strains. *Mol Neurodegener* 9, 29, doi:10.1186/1750-1326-9-29 (2014).